The Dissertation Committee for Andrew Thomas Jamieson Certifies that this is the approved version of the following dissertation:

Top Surface Imaging for Sub-100nm Lithography

Committee:

C. Grant Willson, Supervisor

Roger T. Bonnecaze

Benny D. Freeman

Gyeong S. Hwang

Scott A. MacDonald

Top Surface Imaging for Sub-100nm Lithography

by

Andrew Thomas Jamieson, B.S. Ch.E, B.S. Ch., M.S.E.

Dissertation

Presented to the Faculty of the Graduate School of
The University of Texas at Austin
in Partial Fulfillment
of the Requirements
for the Degree of

Doctor of Philosophy

The University of Texas at Austin
May, 2004

Acknowledgements

I would like to thank my friends, family, coworkers and financial supporters for their help. Without them, I would not be where I am today. The amount of assistance that I received throughout this doctoral program (and life in general) was enormous, and I will be forever grateful.

Specifically, I'd like to thank the Semiconductor Research Corporation for its generous funding in the form of a graduate research fellowship. I would also like to thank the UT College of Engineering for its Thrust fellowship.

Numerous individuals in industry were instrumental in my research. Foremost among them was Scott MacDonald from IBM (now Hitachi). He was a pleasure to work with during his sabbatical at UT. Jeff Byers from KLA-Tencor is a great person and teacher- he taught me an enormous amount about lithography. Adam Pawloski from AMD was great to work with on the base quencher project. I would also like to thank Chris Mack and Roger Bonnecaze for their insightful discussions. Mike Sheehan from DuPont Electronic Materials was generous to allow us to have samples of semiconductor grade polymers. Ralph Dammel of AZ Clariant was helpful in theoretical discussions and in material donations. The collaboration with ETEC was great, and I enjoyed working with the people there.

I was fortunate to have the opportunity to run many experiments at International SEMATECH. In the course of these experiments, I received help from countless people. Danny Miller in particular was a pleasure to work with-

he is a great combination of hard work, good ethics and a great personality. Will Conley provided great assistance and guidance. The crew of Vicky Graffenburg, Georgia Rich, Mike Rodriguez, and Shashi Patel are helpful, hard working people that were a great to spend hours gowned up with. David Stark, Paul Zimmerman, Stefan Hein, and Jeff Muete taught us a lot. In the ATDF, Larry Looger and Jordan Owens were generous for allowing to us to use their steppers and tracks. Chari, Dennis Hanslik, and Arnie Ford were very helpful in all they did.

The Willson research group was a tremendous place to work for four and a half years; Dr. Willson has created an amazing research group. I am indebted to him for his guidance, friendship, and everything he has made possible. Kathleen Sparks is a great person, both professionally and personally. There have been so many graduate students I've had the pleasure to work with that it will be hard to not leave anyone out. Without the help of Mark Somervell, my graduate program would've been longer and more frustrating. His teaching and guidance were excellent. I was fortunate to collaborate with Matt Pinnow. He is a first-rate scientist and person. Without his assistance, this dissertation would be a fraction of what it is. There are a number of other chemists that I worked with closely, including: Charles Chambers, Brian Osborn, Shintaro Yamada, Takashi Chiba, Raymond Hung, Les Carpenter, and HV Tran; a heartfelt thank you to them all. In chemical engineering, I had the pleasure of working with a number of great people. Pavlos was about the best lab-mate a person could have. He is a great person to talk to at any time. Tim Michaelson was an excellent collaborator on many projects, and he played a significant role in much of the work presented here. Steve Johnson, Matt Schmid, Matt Colburn, Sean Burns, Jason Meiring, EK Kim, Mike Dickey, Michael Stewart, Heather Johnoson, and everyone else in engineering were a pleasure to work side by side for my time there.

I was fortunate enough to work with a number of excellent undergraduate students. Zach Hogan played a huge role in my research. He is a top-notch person, both personally and intellectually. Terry Farmer was great to work with. Never before has such a wealth of chemical engineering knowledge, and UT football obsession been combined in one mind. I was also lucky enough to work for shorter times with Ryan Deschner, Rashid Hameed and Cyrus Tabery. I have no doubt that they will all succeed in anything they put their minds to.

Finally, and most importantly, I'd like to thank my family and close friends. Without their amazing support, I would not be where I am today. I cannot express how grateful I am to my parents for all that they have done for me. Peter, Emily and Mike: thank you for always being there. Thank you Monika for your encouragement, patience and caring.

Thank you all again,

-ATJ

Top Surface Imaging for Sub-100nm Lithography

Publication No._____________

Andrew Thomas Jamieson, Ph.D.
The University of Texas at Austin, 2004

Supervisor: C. Grant Willson

Advances in semiconductor microlithography have resulted in reduced transistor dimensions and consequent improvements in chip performance and cost. In the microlithographic process a photoactive material called a photoresist is uniformly spun cast on a substrate and selectively exposed to radiation, causing a chemical change in the exposed areas. The polymer is subsequently removed in either the exposed or unexposed regions, typically using an aqueous base developer.

An alternative to the traditional lithographic method is a process called Top Surface Imaging (TSI). TSI has a number of advantages over traditional base-development techniques but is highly susceptible to line edge deformities commonly referred to as line edge roughness (LER). In TSI, the top surface of the photoresist is exposed to radiation, resulting in the generation of reactive sites. A gas phase, silicon-containing compound called a silylation agent reacts with these sites, causing selective incorporation of silicon. The silicon then acts as an etch mask in an anisotropic oxygen etch process. As the industry continues to improve resolution by shifting to shorter wavelengths, TSI's lax transparency requirements provide it with a distinct advantage over traditional lithographic techniques.

In this work, TSI was evaluated for use with three industrially relevant radiation sources, including 157nm light, low-voltage electron beams, and extreme ultraviolet light. An investigation into the origins of low frequency LER in TSI systems showed it to be the result of surface tension induced capillary instabilities (also known as a Rayleigh instability). The polymer contribution to LER was investigated by the synthesis of numerous high-Tg TSI polymers. Although many of these polymers are capable of producing high-resolution features, they all suffer from significant levels of LER. The kinetics of the gas phase reaction of the TSI polymer poly(hydroxystyrene) and the silylation agent dimethylaminodimethylsilane was investigated using variable angle spectroscopic ellipsometry, and was found to be front propagated and reaction limited. It was found that the addition of base quenchers to chemically amplified photoresists greatly minimizes LER, and a theoretical approach to understand this effect is presented. Overall, TSI performs well, but the nature of LER in TSI systems is still not fully understood.

Table of Contents

List of Tables

List of Figures

Chapter 1. Introduction to Microlithography and Thin layer Imaging

BACKGROUND

Device scaling and economics

Semiconductor manufacturing is a highly competitive industry in which device cost and speed are the major economic driving forces. The competitiveness of the industry was described by Gordon Moore from Intel, when he predicted that the number of transistors per chip would double approximately every year and half [1]. This relation has become known as “Moore’s law”. Any company that cannot keep pace will fall behind and not be competitive. Moore’s law has held true for nearly 40 years, and shows no signs of ending in the near future. The average cost per chip has remained nearly constant over that time period, so the cost per transistor has plummeted. This amazing accomplishment is based on several factors. First, the size of the silicon wafers, which chips are made from has gradually increased from 1” to 12”, while the cost per wafer for most processing steps hasn’t changed dramatically. Second, the size of the average chip has increased, increasing the area on which transistors can be placed (although this has stabilized in recent times). Finally, and most importantly, the size of transistors has shrunk dramatically. Printing smaller features on a wafer (and thus smaller transistors) has enabled more transistors to be placed on a given wafer area, and thus more transistors are produced per processing step. Smaller transistors are faster and cheaper to make. Chips with small transistors are both faster and have more transistors. Intel’s current Pentium 4 chip has features that are 130nm, possess 42 million transistors per chip and operates at speeds of over 2 gigahertz. This amazing miniaturization has been the result of the patterning process called microlithography.

Microlithographic Process

Microlithography is a process that selectively places patterns of material (polymer) on a surface. The polymer acts as mask for subsequent semiconductor processing steps, protecting the underlying region. For instance, during ion implantation, the polymer shields the underlying silicon from dopants that are accelerated at the wafer surface, resulting in selective doping of certain regions of the silicon. The microlithographic process is illustrated schematically in figure 1.1. First, a solution of a polymer is evenly spin coated onto a wafer surface. The solution is typically made up of a polymer, a moderately volatile solvent, a photo active compound and other additives. After coating, the wafer is baked (called a post-apply bake, or PAB), causing the solvent to evaporate, and resulting in a uniform, thin film of polymer on the wafer. The wafer is then selectively exposed to radiation. The radiation interacts with the photo-sensitive coating, resulting in a chemical change within the exposed region. The film is then baked again (called the post-exposure bake, or PEB), resulting in limited diffusion of the exposed photoactive compound (this is necessary to help remove undesired optical effects called standing waves, and in the case of some resists, to allow a catalytic reaction to occur within the exposed region). The chemical change within the exposed areas allows the material to be selectively removed (usually by dissolution into an aqueous base solution). This occurs by either removing the exposed areas (called positive tone) or by removing the un-exposed areas (called negative tone).

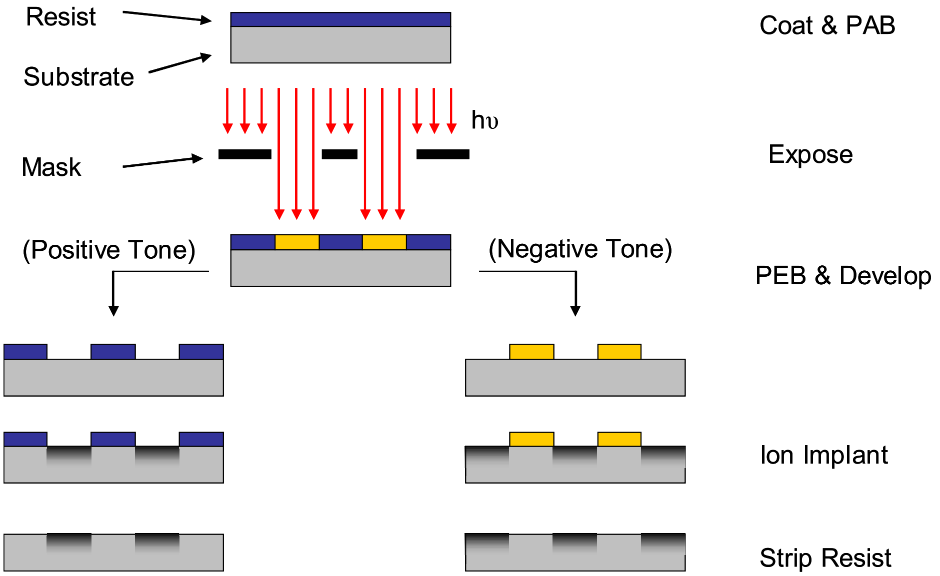

Figure 1.1: The microlithographic process (ion implantation is just an example of many possible processing steps that could occur using the resist as a mask).

The ultimate goal of microlithography is to produce features as small as possible. In optical exposure, the feature size is limited by Rayleigh's equation:

$$\text{Minimum feature size} = \frac{k_1 \lambda}{NA} \tag{1.1}$$

where k_1 is a proportionality constant, λ is wavelength of light, and NA is the numerical aperture of the lens. This equation holds true for a pattern of lines and spaces of equal width. The semiconductor industry has decreased this minimum feature size aggressively by changing all three parameters. k_1 has been decreased by improved resist performance, and moving to alternate exposure techniques (such as off-axis illumination and phase-shifting), but it is quickly reaching the theoretical limit of 0.5 for partially coherent light. The numerical aperture of lenses has been increasing, with current state-of-the-art tools having an NA of 0.8. This too is approaching the theoretical maximum of 1 for tools ($NA = n \sin \theta$, where n is the index of the medium, 1 in this case for air, and θ is the diverging angle from the normal of the sample to the edge of the lens, with 90^o being the maximum). The exposure wavelength has been continuously decreased from the Hg arc lamp bands of 436nm and 365nm, down to excimer laser wavelengths of 248nm, 193nm and 157nm. Current state-of-the-art production tools are just now beginning to use 193nm light, and research is underway to develop either a viable 157nm process or a 193nm process with water in between the photoresist and the bottom lense element (increases NA by increasing the index of refraction).

Photoresist Chemistry

Typically, the subsequent processing steps require the polymer to have certain material properties. The process with the most stringent requirements is plasma etching. In order for a polymer to adequately act as an etch mask, it must have a relatively low etch rate in plasma environments, which is accomplished by using polymers that contain cyclic structures and often have relatively high degrees of unsaturation. In addition, the resist coating must be of sufficient thickness that it will not be entirely consumed during the etch processes.

In traditional resist processes, the light renders the exposed resist either soluble or insoluble in aqueous base developer. The photoresist must be relatively transparent at the exposure wavelength in order to have the solubility switch occur throughout the thickness of the film. This requirement has grown progressively more challenging as imaging wavelengths have decreased. In fact, most polymeric materials are extremely absorbing in the UV, and significant research has been performed to create materials that will function at 248nm, 193nm and 157nm. One can avoid this problem by going to thinner and thinner films; however, the plasma etch process requirements typically place a minimum value upon thickness.

Microlithography with wavelengths of 365nm or longer was performed using diazonapthoquinone (DNQ)/ novolac based resists. Novolac is a polymer that is inherently soluble in aqueous base developer. DNQ is a photoactive compound that when unexposed, inhibits the dissolution of novolac. Upon exposure, the DNQ undergoes a chemical reaction to form a compound that enhances the solubility of the novolac. Thus, the resist system is positive tone. It takes at least one photon to chemically alter one DNQ molecule. The reader is referred to Ralph Dammel's book[2] for a thorough discussion of DNQ / Novolac resists. Unfortunately, novolac is not sufficiently transparent for use at 248nm, so the industry was forced to change to a new polymer resin. Additionally, for various reasons (including throughput), it was decided that the new photoresist should be more sensitive to light than the DNQ / Novolac system.

It was quickly found out that poly(hydroxystyrene) (PHS) was transparent at 248nm, and soluble in base developer. Unfortunately, DNQ does not inhibit the dissolution of PHS, and no other dissolution inhibitor could be found. Instead, Ito and Willson proposed a different mechanism for introducing a solubility switch to this system[3]. Called "chemical amplification", the process consisted of placing an acid labile protecting group on the acidic hydroxyl group, and incorporating a photoacid generator into the resin solution. Upon exposure, acid is generated in the film, and during the post-exposure bake the acid catalytically removes the protection group. Thus, within the exposed areas, soluble PHS is generated. Reaction A illustrated this scheme using t-butoxycarbonyl (t-BOC) on PHS. Chemically amplified resists are predominant in the semiconductor industry for imaging at wavelengths of 248nm and shorter.

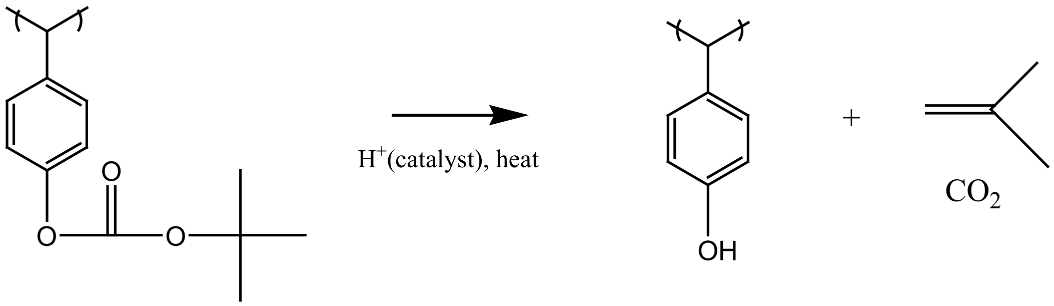

Reaction A

Thin Layer Imaging

Thin layer imaging (TLI) techniques are alternatives to traditional single layer processes and have long been considered for industrial implementation[4]. Fundamentally, a TLI technique is one in which the imaging is performed in a very thin section at the top of the resist, and then the image is transferred anisotropically down through the resist, usually utilizing reactive ion etch processes. Schematically, the process is shown in figure 1.2.

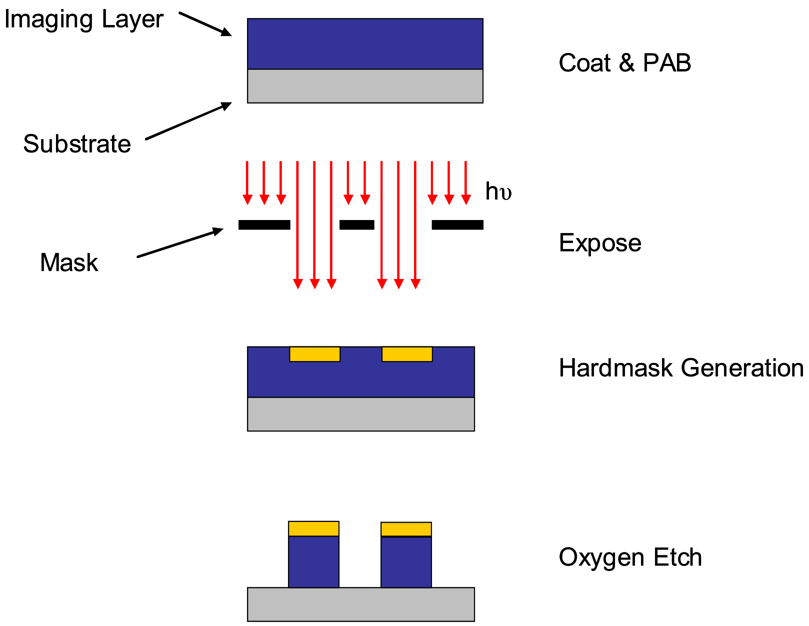

Figure 1.2: Schematic of thin layer imaging technique.

There are many advantages to thin layer imaging processes. First, the transparency requirements are dramatically lower. One only needs to have good energy deposition profiles in the top ~150nm of the resist in order to generate tall features. The height of the final profile is dictated by the transfer layer (the layer which is etched through), rather than the imaging depth. Second, thin layer imaging techniques do not suffer from feature collapse due to capillary forces, as occur in traditional wet-developed resist systems. In single layer systems, during the drying step after development, water between lines can pull features down if the pitch (distance between the centers of sequential lines) is too close. Finally, since imaging must be performed in a thinner film, these systems should perform with better depth-of-focus (errors in focus of the stepper, or topography can cause features to print poorly; a better depth-of-focus allows for better process control).

Unfortunately, these thin film imaging techniques also suffer from added complexity. At the bare minimum, they require a plasma etch step, and often include additional coating steps, or gas phase reaction steps. As such, they have been slow to be accepted into practice. However, as lithography processes grow more and more challenging, people have grown more accepting of these techniques as alternatives, especially if no single layer process exists that will work for a given application. Two thin film imaging techniques are used in industry today: bilayer processes and the CARL process.

A bilayer technique is shown schematically in figure 1.3. It involves the coating of two layers. The bottom layer is typically a non-functional polymer (often novolac) that contains only carbon, hydrogen and oxygen. The layer is usually baked at a high temperature after coating, resulting in cross-linking. The top layer is a thin (~150nm), functional resist that typically contains at least 12% silicon in addition to carbon, hydrogen and oxygen. The stack is exposed, and the top layer undergoes a solubility switch. The material is developed in aqueous base, resulting in silicon containing features atop a uniform transfer layer. The stack is then etched in a reactive ion etcher containing an environment of mainly oxygen gas. The silicon containing resist quickly oxidizes to silicon dioxide, which is inert to oxygen plasma, while the regions that do not possess the top resist are quickly etched away, forming water and carbon dioxide. One can tune the etch process to perform the etch anisotropically, resulting in vertical features. This technique is shown schematically in figure 1.3.

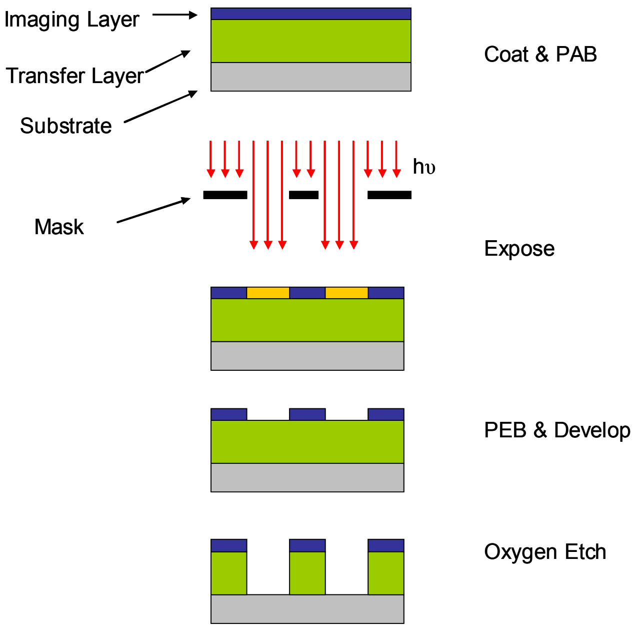

Figure 1.3: Schematic of a positive tone bilayer imaging process.

Bilayer processes have all the aforementioned advantages of thin layer imaging techniques. Typically, they are used in industrial processes which require exceptionally high aspect ratio features patterned over topography. The major drawbacks to the techniques are the addition of an extra coating step, and a plasma etch step, both of which are not required with traditional resists (although most resists require both the spin-casting of an anti-reflection coating and a "trim etch" step after development, so bilayer resists don't add too much complexity). A further drawback is the added potential for contamination of the bottom lens element of an exposure system with silicon. During exposure, small amounts of resist can degrade and outgas into the volume above the resist. These materials can contaminate the lens, degrading optical performance, which necessitates cleaning of the lens. Unfortunately, contamination by silicon onto the fused silica lens element is nearly impossible to clean. This results in costly replacement of the bottom lens element. As such, bilayer processes are considered moderately controversial in many circles.

The second thin layer imaging process that is practiced in industry is called Chemical Amplification of Resist Lines (or CARL). Originally developed by Infineon, this process is similar to the bilayer process, except for the fact that the silicon is incorporated into the top resist in a liquid silylation step after base development. The process is shown schematically in figure 1.4.

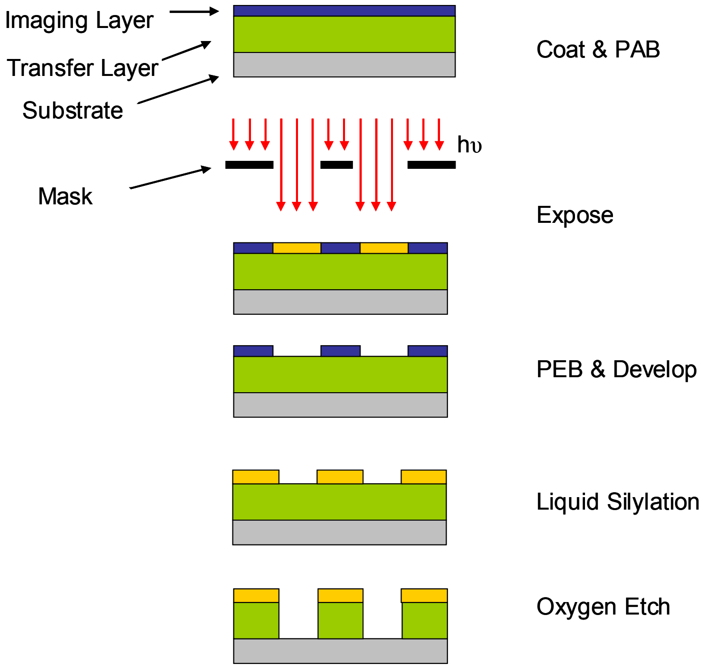

Figure 1.4: Schmatic of Infineon's CARL Process.

Clearly, CARL has significantly more process complexity than a traditional resist. It incorporates one extra coating step, one extra etch step, and a liquid silylation step. It possesses all the benefits of the bilayer process, with two additional advantages. First, the top layer doesn't contain nearly as much silicon as is present in bilayer, thereby decreasing the chances of uncorrectable lens contamination. Second, and more important, is a result of the liquid silylation step. During the silylation step, the resist swells in size, both vertically and horizontally. This allows lithographers to print a space at the Rayleigh limit, and then shrink the space further. So, they are able to print so-called "trenches" beyond the Rayleigh limit of their tool. Alternatively, they can over-expose the resist, making the pre-silylated images smaller than they desire, and then swell the images up to the size they want. The advantage of this over-exposure is that typically the so-called the “iso-focal dose”- the dose at which focus errors minimally affect feature size - occurs at an over-exposed dose. Therefore, they are able to gain significant process latitude by using this thin layer imaging process.

2. TOP SURFACE IMAGING BY VAPOR-PHASE SILYLATION

Introduction to Top Surface Imaging

Top surface imaging (TSI) is a thin film imaging technique with a fairly simple process flow. As opposed to the bilayer and CARL processes discussed earlier, TSI only employs a coating step, an exposure step, a gas phase reaction step and an oxygen etch step. The fundamental idea behind TSI is that a single resist film is coated on a substrate and exposed to light or electrons in such a way that only the top of the resist is chemically altered (either by working at a wavelength at which the resist absorbs, or at an electron energy where the penetration depth is shallow). The resist is then put in the presence of a silylation agent, which causes silicon to be incorporated into either the exposed or unexposed region. The film is then etched in an oxygen plasma, where the incorporated silicon acts as a hard mask, protecting that region.

In the TSI system studied here, silylation contrast is created by a photo-induced switch in the chemical reactivity of the polymer. A polymer that is unreactive to vapor phase silylation is rendered reactive through a chemically amplified mechanism. Fig. 1.5 shows how this process works using poly(4-*t*-butoxycarbonyloxystyrene), also referred to as t-BOC styrene[5]. In this system the polymer has two states, reactive and unreactive. Since the polymer is always in one of these two states, the silylation is digital. The other feature is subtle but important. Exposure and heat causes deprotection (which changes the polymer's reactivity to silylation) with concurrent loss of volatile products. As a result of this volatilization, the polymer film shrinks in the regions of exposure. The silylation reaction, however, changes the mass and volume of the polymer substantially and causes it to swell. The net change in thickness is small in the case where dimethylaminodimethylsilane, a silylation agent, is used, which results in very little image deformation throughout the process.

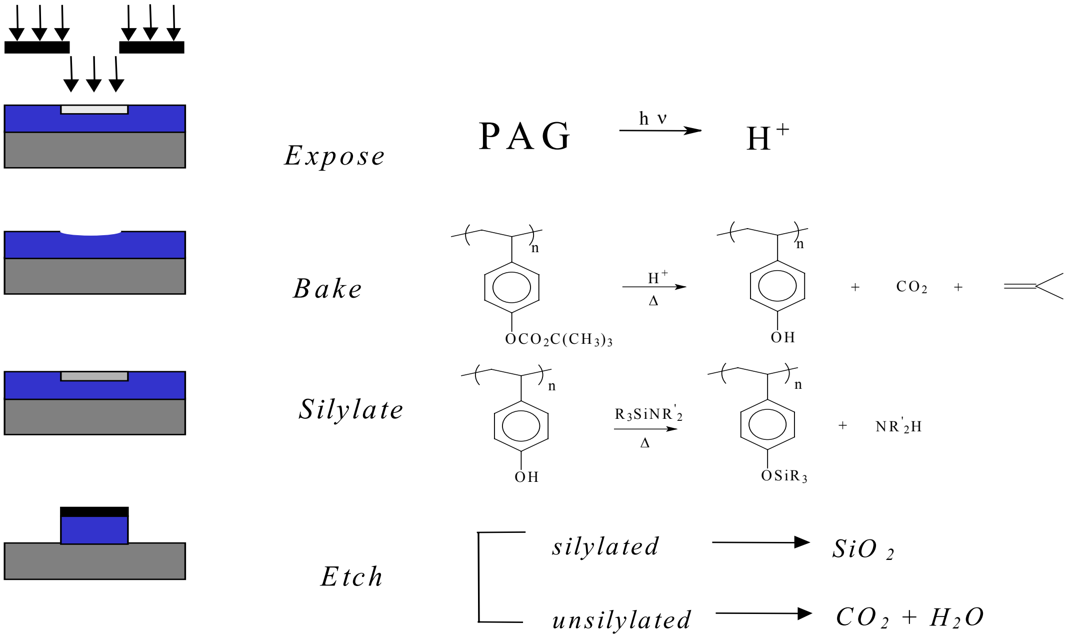

Figure 1.5: Process Schematic for Negative Tone TSI System

Top surface imaging using t-BOC styrene has produced high resolution, high aspect ratio images when exposed with 248nm and 193nm light[6]. Figure 1.6 shows images patterned at 193nm. As can be seen, the images have vertical sidewalls, and are patterned near the resolution limit of the exposure tool. Unfortunately, upon closer inspection, the images suffer from significant levels of line edge roughness (LER), as is shown in top-down scanning electron micrograph in figure 1.7.

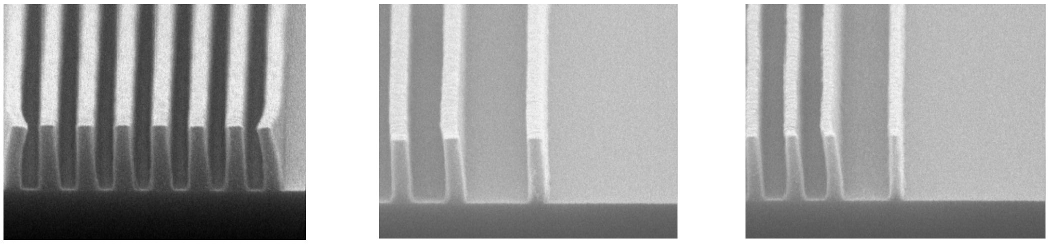

0.15 μm
3.8 mJ/cm^2

0.11 μm
6.2 mJ/cm^2

90 nm
6.2 mJ/cm^2

Figure 1.6: High resolution, high aspect ratio features printed with a TSI scheme employing t-BOC styrene with binary illumination at 193nm.

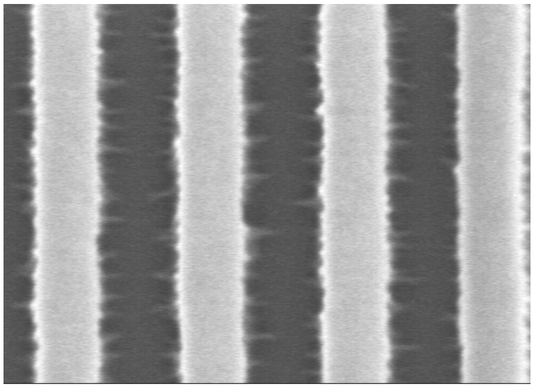

Figure 1.7: Top-down scanning electron micrographs of line-edge roughness in t-BOC stryene, a) low levels of LER (but still unacceptable), largely at footing of lines.

The fundamental nature of line edge roughness in TSI systems is still poorly understood, and is subject of paramount interest. Fortunately, a TSI system has been developed which possesses nearly no LER[6]. Originally discovered by Mark Somervell, the system employs a co-polymer of *tert*-butyloxycarbonyl protected 3-bicyclo[2.2.1]hept-5-ene-2-yl)-1,1,1-trifluoro-2-(trifluoromethyl)propan-2-ol (tBOC-NBHFA) and sulfur dioxide. The polymer is shown in figure 1.8 and is henceforward referred to as PFAS. The norbornene ring is employed for etch resistance in post-lithography processing. The hexafluoroalcohol unit was used due its pKa of 12, which behaves similarly to poly(hydroxystyrene) in reactions with silylation agents. The sulfone linkage was incorporated largely out of necessity in the polymerization process, as techniques had not been developed to homopolymerize NBHFA (this has subsequently changed, and will be discussed later). Due to the increased mass of the repeat unit as compared to poly(hydroxystyrene), a new silylation agent was necessary in order to increase the silicon content of the fully silyated polymer above 12% (wt) (the threshold level of silicon above which the features will not etch in an oxygen plasma environment). David Wheeler of Sandia National Laboratories generated a synthetic route to create dimethylaminodimethyldisilane (DMADMDS), also shown in figure 1.8. This polymer system is capable of printing with very smooth images, as is shown in figure 1.9.

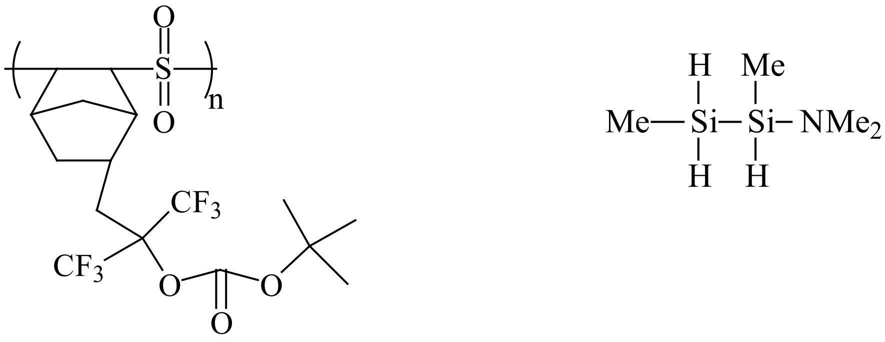

Figure 1.8: PFAS and DMADMDS.

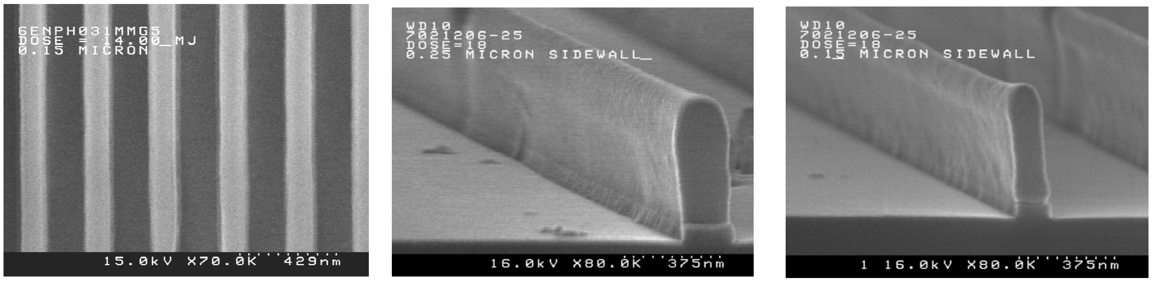

Figure 1.9: Smooth Imaging performed with PFAS.

The fundamental material property differences between these two polymers are many. However, if one could determine the critical parameters that enable the second system to print as cleanly as it does, one might be able to apply these lessons to the design of future TSI systems. PFAS suffers from additional problems which would make it difficult to use in industry, such as cleavage of the backbone which releases sulfur-dioxide. Additionally, the challenging synthetic route to DMADMDS greatly limits its availability, and thus the potential for process optimization. As such, generation of new polymer systems would be extremely beneficial.

It was believed that two material properties were largely responsible for the smooth imaging behavior of PFAS. The first property is the high glass transition temperature of the polymer, especially in its silylated state. The Tg of silylated PFAS is around 120^{o}C (the Tg of silylated poly(hydroxystyrene) is ~70^{o}C). This Tg is substantially higher than the silylation process temperature of 90^{o}C. The structures that are created in lithographic processes are thermodynamically unstable, and processing above the Tg allows material flow, usually with poor results. The fundamental mechanisms of this material flow are not well understood in relation to these systems. The second material property that is dramatically different in these two systems is the opacity of the polymers. PHS is extremely absorbing at 193nm, and as such, the feature edge is poorly defined. The random nature of the deprotection reaction and the etch process could stochastically degrade this poor feature edge, resulting in roughness. PFAS on the other hand is fairly transparent, and the resulting feature edge is more clearly defined. Figure 1.10 shows energy deposition profiles in the two resists at 193nm.

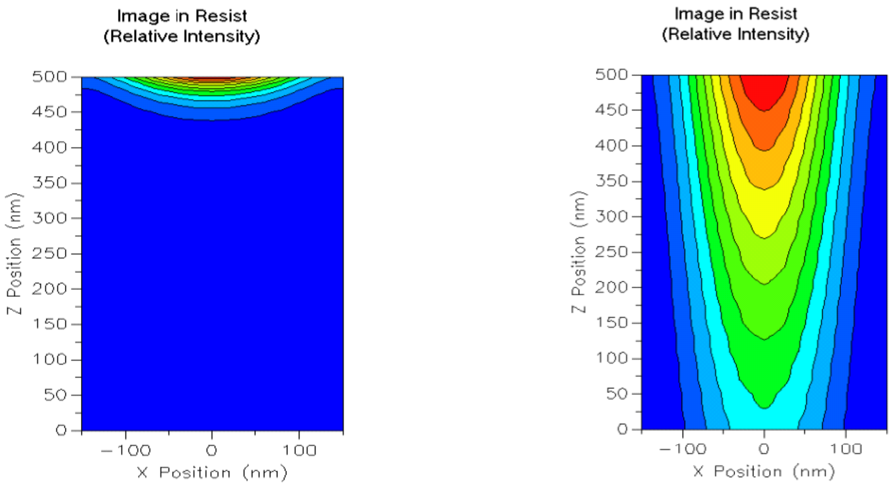

Image in Resist
(Relative Intensity)

Image in Resist
(Relative Intensity)

A

B

Figure 1.10: *Energy deposition profiles in a) PHS and b) PFAS (red corresponds to high relative intensity, while blue represents low relative intensity). Note the clear edge definition in the more transparent polymer on the right.*

3. RESEARCH OBJECTIVES & ACCOMPLISHMENTS:

The goals of this dissertation were originally stated in my preliminary document. They were broken into four distinct area of research, including:

1. Application of TSI to new exposure sources.
2. Investigation of mechanisms of line edge roughness in TSI.
3. Development of new TSI polymer systems.
4. Fundamental investigations of silylation reaction.

All of these areas were studied thoroughly, and a brief synopsis of the goals and accomplishments of each area are shown below.

1. Application of TSI to New Exposure Sources.

Goals / Motivation:

Resists and microlithography processes at current commercial exposure wavelengths are well developed and optimized. Resist processes for future exposure sources are largely undetermined. Ideally, industry would prefer to work with a traditional single layer process, but that is often very difficult. Thus, it is extremely important to study alternate techniques for use in these next generation lithography (NGL) systems. From a researcher's perspective, these NGL exposure sources are capable of printing much higher resolution features than are currently available at today's wavelengths of 248nm and 193nm. Working with higher resolution features and different energy deposition profiles in general allows investigation of fundamental mechanisms of resist behavior that cannot be seen when working with larger features.

Therefore, the first area of research that I planned to investigate was the application of TSI to alternate exposure sources. There are many exposure sources that have been proposed for future industrial use. Three exposure sources that are particularly interesting to investigate are 157nm light, low-voltage electron beams (1-3kV) and extreme ultra violet (EUV, or 10-14nm). 157nm light is slotted to be the next major wavelength that will be used in industry, and is currently slated to go into production at the 70nm feature node, which will occur sometime around 2006. International SEMATECH in Austin has a 157nm stepper that we have access to, and TSI applications can be investigated thoroughly with this exposure source. Low voltage electrons have been suggested for use in mask making applications due to their amenability for use in micro-column arrays (multiple exposure sources simultaneously exposing a single sample). A major challenge associated with application of this technique lays in finding a suitable resist system. Low voltage electrons have very shallow penetration depths (~25nm for 1kV electrons), and as such, a thin film imaging technique is absolutely necessary to produce adequate etch resistance for later processing. Top surface imaging is particularly well suited for this application, as even bilayer applications may not work here since spin coating films of less than 70nm is difficult due to thin film instabilities. Additionally, electron beam exposure often has very high resolution, so probing fundamental mechanisms of TSI is particularly possible. EUV is currently slated for introduction to industrial practice after 157nm lithography, and as such, is a wavelength whose resist processes haven't been well investigated.

Accomplishments:

In the course of this research, TSI was applied to nearly every next generation lithography (NGL) exposure source that is presently being considered by industry. These include 157nm light, 13nm light (aka Extreme Ultraviolet (EUV) and low voltage electron beam exposures. TSI performed fairly well in all of these studies, but in the end still suffered from LER (although much headway was made in the understanding of this area). The work at 157nm is presented in chapter 2. Chapter 3 is a summary of work performed in collaboration with ETEC systems in Hayward, CA on the application of TSI to low-voltage electron beam exposure sources. Along with TSI, studies based on another promising thin-film imaging technique, HSQ bilayer, are presented. Preliminary studies on the utility of TSI for use as a EUV resist were performed, but is not presented here since it did not provide much new knowledge. Overall, TSI performed adequately in these new applications, but suffered from a somewhat larger magnitude of LER than is desired. The main benefit of these experiments was the increased knowledge and data that resulted. Although it is often tempting to do so, creating theories on limited amounts of data is a risky proposition. These imaging experiments not only examined the application of the TSI process to new conditions, but created a large body of data from which to work.

2. Investigation of Mechanisms of Line Edge Roughness Formation in TSI

Goals / Motivation:

Line edge roughness is the largest problem in TSI, and the origins of the phenomenon are not fully understood. This problem caused Intel, Texas Instruments, Bell Labs, and other companies to halt research into TSI. Until the paper of Somervell, et al[6] it was thought that TSI and line edge roughness were not separable. The beginning of my thesis was a unique time in research of this area since examples of materials that print roughly and materials that print smoothly were available. The critical material properties related to line edge roughness proposed in the previous section seem reasonable, but a detailed analysis of the effects of aerial image, and low glass transition temperature had not been performed when those theories were made. In fact, when this work began, there were many questions that remained about the nature of line edge roughness that the previous theories did not entirely encompass. For instance, although silylation of PFAS above its Tg at 130^{o}C does produce rough images, silylation of PHS below its Tg of 70^{o}C (say at 50^{o}C) does not produce smooth images. It has been postulated that this results from silylation agent sorption, and hence plasticization, of the resist, but this had not been carefully studied. It was my aim to investigate line edge roughness in TSI systems from a mechanistic standpoint. The goal was to acquire an understanding that could aid in the design of polymers for TSI.

Accomplishments:

LER in chemically amplified systems in general is an extremely complicated topic that is still poorly understood in the lithography community today. In the author's opinion, LER may become the major obstacle to continuation of Moore's law sometime in the not too distant future, barring a revolution in photoresist design. Since LER in chemically amplified systems in general isn't understood fully, a complete understanding of LER in chemically amplified TSI systems is still limited. Previous work by Somervell indicated that alteration of the polymer structure was capable of fixing LER in TSI in and of itself. Although true for that particular case, duplication of that performance in other polymer systems was elusive. Nearly 20 new TSI polymers were synthesized and none performed nearly as well as PFAS. This work is documented in chapter 5. The hypothesis that the use of high Tg polymers could fix LER was tested and proven incorrect. High Tg does however have the benefit of kinetically quenching phenomena associated with polymer mobility. Chapter 4 shows how mobility can result in alteration of structures by using a Rayleigh Instability analysis. In essence, this chapter shows theoretically that some of the structures that are creacted lithographically are thermodynamically unstable, and need to be kinetically quenched.

Finally, the low-kV TSI experiments revealed the amazing effects that base quenchers have on line edge roughness in TSI systems. In fact, base quenchers have dramatic, but poorly understood effects on all chemically amplified systems, base-developed included. Certain aspects of their performance-improving behavior are studied in chapter 7. The work was performed on a base-developed system due to its larger relevance, but applies equally to TSI systems as well.

3. Development of New TSI Polymer Systems.

Goals / Motivation:

In the end, a working polymer system that uses readily available materials to produce high quality images is the goal of any research program in top surface imaging. As is often the case, sometimes the best approach to solve a problem is to simply go out and experiment. The fundamental understanding that we had at the beginning of our experiments (aim for high Tg materials that are moderately transparent) we hoped would meet the requirements adequately to make a workable TSI process. A major portion of the Willson research group was devoted to the development of single layer resists for application at 157nm. Close collaboration with the skilled chemists working on that project had a good chance of bearing fruit in this area. As such, it was my plan to synthesize, characterize and test new polymers for TSI applications. At the very least, having more data points when it comes to systems that work, and systems that don't, would increase our understanding of the fundamental processes that contribute to line edge roughness.

Accomplishments:

Numerous novel TSI imaging systems were developed and evaluated, and none of them matched the Line edge roughness present in previous work with PFAS. Chapter 5 summarizes all the polymers that were developed in the course of this dissertation. Overall, it appears as though alteration of polymer structure in nearly all cases doesn't dramatically improve imaging performance.

4. Fundamental Investigations of the Silylation Process

Goals / Motivation:

A chemically amplified top surface imaging (TSI) scheme consists of three main processing steps. First, one coats a resist, bakes it, exposes it to radiation and then bakes it again, resulting in a film patterned with a latent image of reactive sites. Second, one exposes the resist to a gaseous silylation agent, which incorporates silicon into the reactive sites through covalent bond formation. Finally, one performs an oxygen reactive ion etch on the resist, anisotropically removing resist from the regions that lack silicon. Most TSI systems suffer far greater levels of line edge roughness than wet-developed processes. In order to understand the cause of this problem, one must investigate the process of which we have the least understanding. The first processing step has been studied in great depth by countless researchers around the world. There are still many fundamental questions associated with that step, but overall it has been well investigated. Numerous people studied the third step as well, and although it is not completely understood, the process space in this area has been explored thoroughly. It is likely that these two steps are not the cause of the dramatic line edge roughness found in TSI. The second step however, has not been fully probed, and many fundamental questions remain.

The standard techniques that have been used to investigate thin film processes in resists, such as infrared spectroscopy, interferometry, and quartz crystal microbalance are a challenge to apply to in-situ studies of the silylation reaction. In order to get infrared spectroscopy to probe the reaction, one must create a cell with a very limited pathlength in order to bring the film signal out from the background of the gas phase. Interferometry lacks the ability to compensate for changes of index within a film which would likely occur during reaction and swelling. Finally, a quartz crystal microbalance lacks the ability to distinguish between changes in mass and changes in modulus when dealing with sorption in polymer films, and thus lacks the ability to generate quantitative data with any accuracy. Therefore, it was proposed that a technique to investigate the fundamental mechanisms associated with the silylation reaction be developed. The construction of a silylation cell that will work in a real-time Woolham ellipsometer was the planned research route.

Accomplishments:

A silylation chamber that allows for *in-situ* ellipsometric monitoring was constructed and automated. The silylation kinetics of poly(hydroxystyrene) were investigated thoroughly and are presented in chapter 6. The reaction was found to proceed by a front-propagated, reaction-limited mechanism. The silylation agent is very soluble in the reacted film, and nearly insoluble in the unreacted film. The solubility was measured by monitoring the unidirectional expansion and contraction of a thin film upon exposure to the silylation agent.

References:

(1) Moore, G. E. *Electronics* **1965**, *36*.

(2) Dammel, R. R. *Spie Press* **1993**, *TT 11*.

(3) Ito, H.; Willson, C. G. *Polymers in Electronics* **1984**, *ACS Symposium Series 242*, 11-23.

(4) Thompson, L. F., Willson, C. Grant, Bowden, M. J. *Introduction to Microlithography*; ACS, 1983.

(5) Ito, H.; MacDonald, S. A.; Miller, D. A.; Willson, C. G. *US Patent* **1985**, *4,552,83*.

(6) Somervell, M. H.; Byers, J.; Willson, C. G. *Abstracts of Papers of the American Chemical Society* **1999**, *218*, 29-PMSE.

Chapter 2: Top Surface Imaging at 157 nm

ABSTRACT:

Top surface imaging (TSI) has had an interesting history. This process showed great promise in the late 1980's and several attempts were made to introduce it to full-scale manufacturing. Unfortunately, defect density problems limited the process and it fell from favor. TSI emerged again as an important part of the EUV and 193 nm strategies in the early stages of those programs because it offered a solution to the high opacity of common resist materials at both wavelengths. A flurry of research in both areas identified new, transparent polymers for single-layer resists, and the seemingly insurmountable problem of line edge roughness in TSI resists, which caused the process to be dropped from both programs. Recent developments in TSI have demonstrated the ability to print high-resolution, high-aspect ratio images at 193 nm with less line edge roughness than typical single layer resist systems. This has largely been due to the development of a polymer specifically tailored for that end use. The 157 nm program has much in common with the early stages of the 193 nm program. The optical density of even 193 nm resist materials at 157 nm is far too high to allow their use in single layer applications. The less stringent optical density requirements of TSI make it a potentially viable imaging scheme for use at 157 nm. Various TSI materials, including the traditional *t*-BOC styrene, as well as novel aliphatic cyclic polymers bearing bis-trifluoromethylcarbinol substituents,

have been investigated for use at 157 nm, and smooth high-resolution images have been generated.

INTRODUCTION:

The semiconductor industry continues to drive toward production of devices with smaller and smaller critical dimensions. This quest has generated many difficult challenges. When the industry moved to 248 nm exposure light, the challenge was to find a material that was appropriately transparent and functioned with low energy doses. Chemical amplification with poly(hydroxystyrene) based systems overcame these obstacles. At 193 nm, the primary challenge lay in optical transparency, since phenolic materials absorbed strongly. Fortunately, it was found that alicyclic materials such as norbornene and adamantane provided both transparency and adequate etch resistance.

At the exposure wavelength of 157 nm, the industry faces the same optical density challenge, but with a much more limited set of transparent functional groups from which to work. At 157 nm, nearly everything absorbs light, including polyethylene, which is made up of only C-C and C-H bonds. Preliminary work by Kunz[1] and others[2] indicates that polymer systems based on siloxanes and fluoro-carbons are the most transparent platforms for resist design, and functional, etch resistant photoresists have now been formulated with absorbances of around 1 μm^{-1} [3]. However, even with polymer systems that are this transparent, in order to achieve appropriate sidewall angles, resist coatings will have to be fairly thin, usually less than 200 nm. This thickness is not adequate for many subsequent etch processes, so in case polymers with lower absorbance are not found for single layer systems, many people are looking into alternative imaging schemes including inorganic BARC "hardmasks"[4,5], bi-layer processes[6] and top surface imaging[7]. Further motivating the push towards alternative imaging schemes is the problem of feature collapse in base-developed systems. Studies by researchers at University of Wisconsin and International SEMATECH show that the critical aspect ratio of collapse scales roughly linearly with pitch, and as such, 70 nm nested lines will likely be limited to aspect ratios of less than 2 in wet developed systems[8].

This chapter focuses on the application of top surface imaging to 157 nm lithography. The TSI systems in this paper have silylation contrast created by a photo-induced switch in the chemical reactivity of the polymer. A polymer that is unreactive to vapor phase silylation is rendered reactive through a chemically amplified mechanism. Fig. 2.1 shows how this process can be implemented in tBOC styrene.[9,10] This example serves to display some important features of the process design. In this system the polymer has two states, reactive and unreactive. Since the polymer is always in one of these two states, the silylation is digital. The other feature is subtle but important. Exposure and heat causes deprotection (which changes the polymer's reactivity to silylation) with concurrent loss of volatile products. As a result of this volatilization, the polymer film shrinks in the regions of exposure. The silylation reaction, however, changes the mass and volume of the polymer substantially and causes it to swell. Silylation of poly(hydroxystyrene) with dimethylaminodimethyldisilane (DMADMDS) is shown in Reaction Scheme A. The mass loss due to deprotection and the mass gain due to silylation are balanced to make the net change in the resist film thickness zero.[11] This effect is desirable because thickness changes in the film can lead to unwanted image distortion that drastically diminishes the quality of imaging. This system may therefore be described as a "digital, zero-volume change, TSI process."

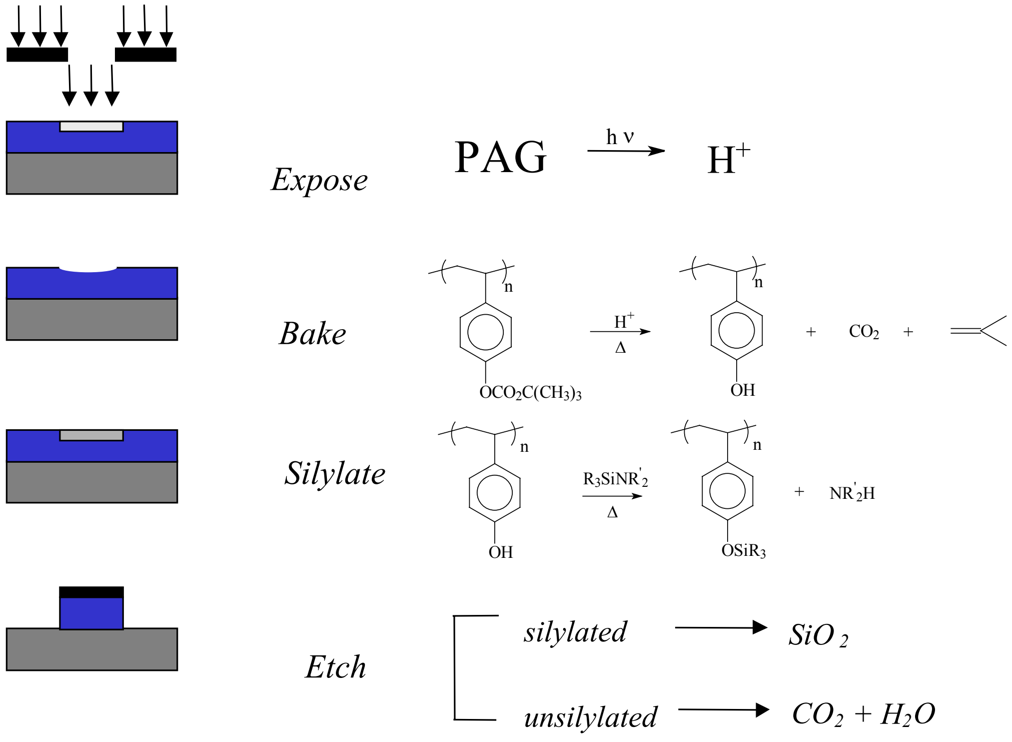

Figure 2.1: Process Schematic for Negative Tone TSI System

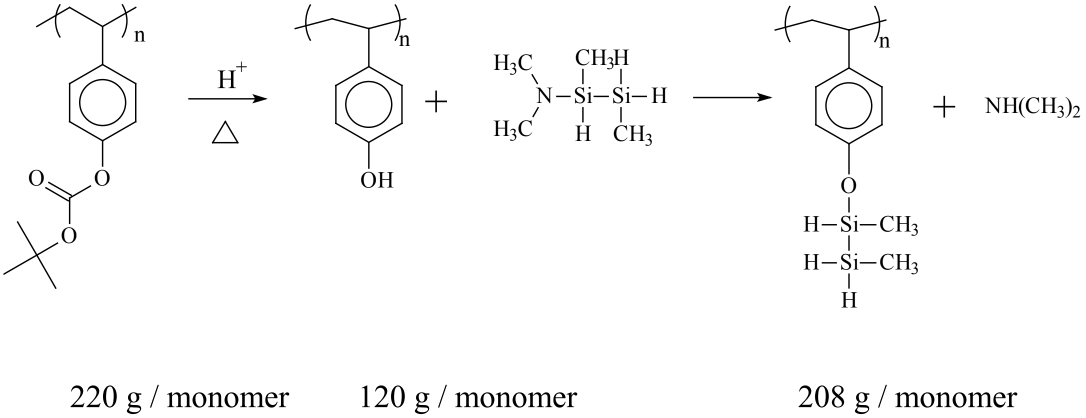

Scheme A

EXPERIMENTAL AND MATERIALS

Materials

*t*BOC-Styrene was prepared by polymerization of 4-*t*-butyloxycarbonyloxystyrene monomer donated by Triquest chemical company. A typical polymerization procedure is given below. *t*-BOC-styrene monomer, (20g, 0.091 mol), was dissolved in dry THF (40mL) in a round bottom flask. The solution was heated to 60°C and then 0.2g of AIBN (0.2g) was added. The resulting solution was stirred overnight, cooled to room temperature, and diluted with an additional 20ml of THF. The THF solution was added to 1L of rapidly stirred methanol whereupon a white precipitate formed. The polymer was isolated by filtration, dried *in vacuo* at room temperature for 24 hours, redissolved in THF, and then reprecipitated. The resulting white polymer powder was obtained in 85% yield after the two precipitations and typically had a number averaged molecular weight of 25,000 with a Mw / Mn of 1.8.

PFAS was prepared by the free radical polymerization of SO_2 with *t*BOC-NBHFA. A typical polymerization procedure is given below. Sulfur dioxide (25mL) was condensed in a round bottom flask at -41^{o}C (dry ice / acetonitrile). A solution of *t*BOC-NBHFA (5g, 13.3 mmol) in 22.5 ml dry THF was added. A solution of *t*-butylhydroperoxide (23μl, 0.31 mmol) was added in 2 ml dry THF, and the reaction vessel was stirred for 4 hours. In order to quench the reaction, hydroquinone (70mg, 0.64 mmol) was added, and the flask was allowed to warm to room temperature after the polymerization, evolving SO_2 gas. The polymer solution was mixed with 75ml of ethyl acetate and washed with 5% $NaHCO_3$ in water until neutral. The organic phase was then washed with water (3x) and with brine (2x), and dried with $MgSO_4$. The ethyl acetate was removed by roto-evaporation, and the polymer was redissolved into a minimum volume of THF. The polymer was precipitated into hexane, filtered, and dried *in vacuo* at room temperature overnight (3.0g, 51%).

Poly (*t*-BOC-NBHFA) was synthesized by *t*-BOC protection of poly-(NBHFA) with di-*tert*-butyl dicarbonate. Poly-(NBHFA) was prepared by the Pd^{2+} catalyzed addition polymerization in dichloromethane at room temperature, as described in Hung *et al* [4]. Poly-(NBHFA) (3.13 g, 11.4 mmol) and di-*tert*-butyl dicarbonate (5.4 g, 22.8 mmol) were dissolved in 40 ml THF. The solution was stirred at room temperature for 5 minutes. 4-dimethylaminopydridine (0.21 g, 1.14 mmol) was added to the solution. The resulting mixture was stirred overnight at room temperature. The resulting polymer was precipitated into methanol (500 ml), filtered, and dried *in vacuo* at 50°C to give a white powder (3.2 g).

Dimethylaminodimethylsilane (DMADMS) was purchased from Silar Laboratories, and 1,2-dimethylaminodimethyldisilane (DMADMDS) was donated to us by Dr. David Wheeler from Sandia National Laboratories. DMADMDS was used in imaging and contrast curve experiments, while DMADMS was used in the FTIR experiments with poly (NBHFA) for proof of silylation

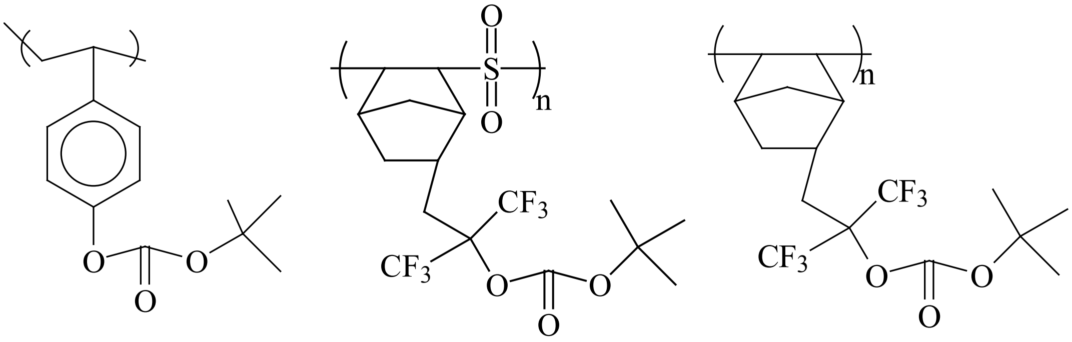

.

t-BOC Styrene PFAS poly (NBHFA)

Figure 2.2: The three polymer systems used in this study.

Experimental Apparatus

Wafers were coated and baked using an FSI Polaris 2000 track. All 157 nm exposures were done using an Exitech micro-stepper at International

SEMATECH (NA = 0.6). For binary mask exposures, $\sigma = 0.7$, for alternating aperture phase-shifted exposures, $\sigma = 0.3$. Silylation was performed using a Genesis 200C at 90°C with DMADMDS for varying times and pressures that are described for each polymer system. Etching was performed on a LAM 9400 SE with the following settings: top power = 260 watts, bottom power 75 watts, pressure = ~3.2 mTorr O_2, flowrate 60sccm O_2, and bottom chuck T = -25°C. Endpoint detection for imaging was done using Endpoint Plus with 30% over-etch. Thickness was measured using a Prometrix interferometer using cauchy coefficients obtained for each polymer system using a Woolham variable angle spectroscoptic ellipsometer. SEM work was done using a Joel tilt SEM and a Hitachi 4500. Absorbance data was taken with a Woolham VUV VASE ellipsometer. IR spectra were taken on-wafer using a Nicolet Magna FTIR 550. For the contrast curve experiments, pad exposures were performed at 248 nm using an Ultratech XLS stepper.

RESULTS AND DISCUSSION

Imaging Experiments

Top Surface Imaging of **t***BOC Styrene*

Previous work[7] with *t*BOC Styrene at 193 nm led to the proposal that line edge roughness was largely due to two factors. The first factor is the high opacity of *t*BOC Styrene at 193 nm. The high opacity results in poor feature edge definition, and a stochastic etch mask degradation process along the edge of the feature during the etch step. The second factor is the low Tg of the silylated form of the polymer of 70^{o}C. The silylation reaction is run at a temperature of 90^{o}C, and as such, during the silylation step, the polymer is mobile, and the image can blur as a result of flow, phase separation or some other mechanism. For this work at 157 nm, the transparency of the resist is significantly better than at 193 nm (as can be seen in Fig. 2.3, although it is still relatively high at ~6 um^{-1}), which is expected to improve imaging performance. This is a necessary, but not sufficient characteristic. Based on this theory, the low Tg of the silylated polymer should still result in roughness.

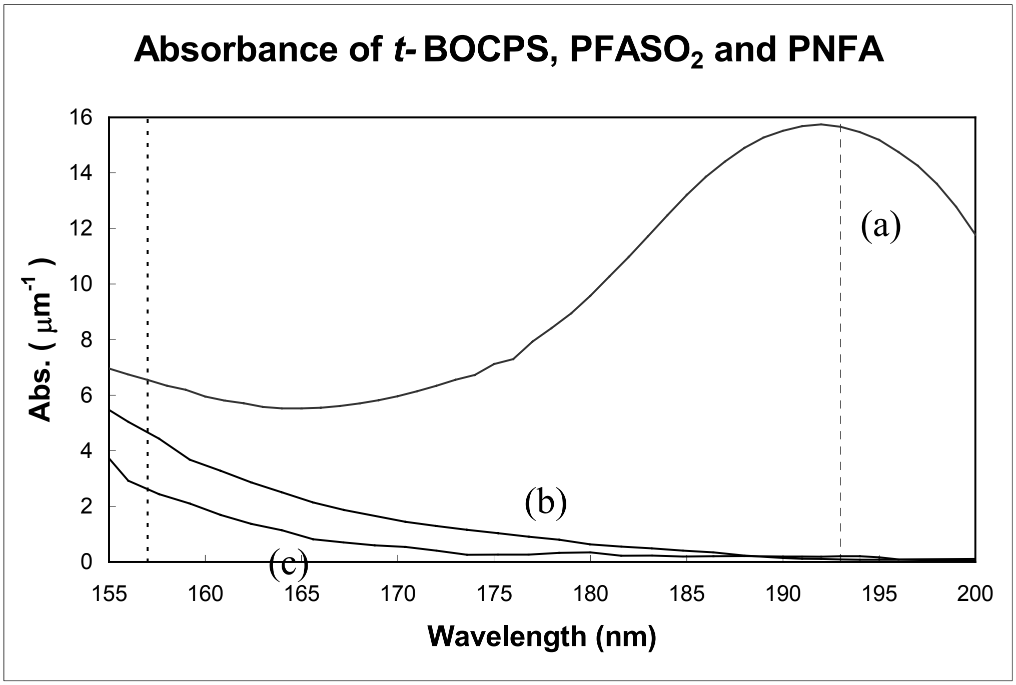

Figure 2.3: Absorbance (a) *t*-BOC styrene, (b) PFAS, and (c) poly(NBHFA as a function of wavelength

*t*BOC Styrene was formulated with 4% DPI-Nf (wt PAG / wt Poly) and 5% trioctylamine (moles base / moles PAG) in PGMEA. PAB was 100^{o}C for 60s, PEB 100^{o} for 60s. The resist was silylated at 90^{o}C for 60s at 30 torr DMADMDS. The resist was imaged at 157 nm using a binary mask and the resulting images are shown in Fig. 2.4.

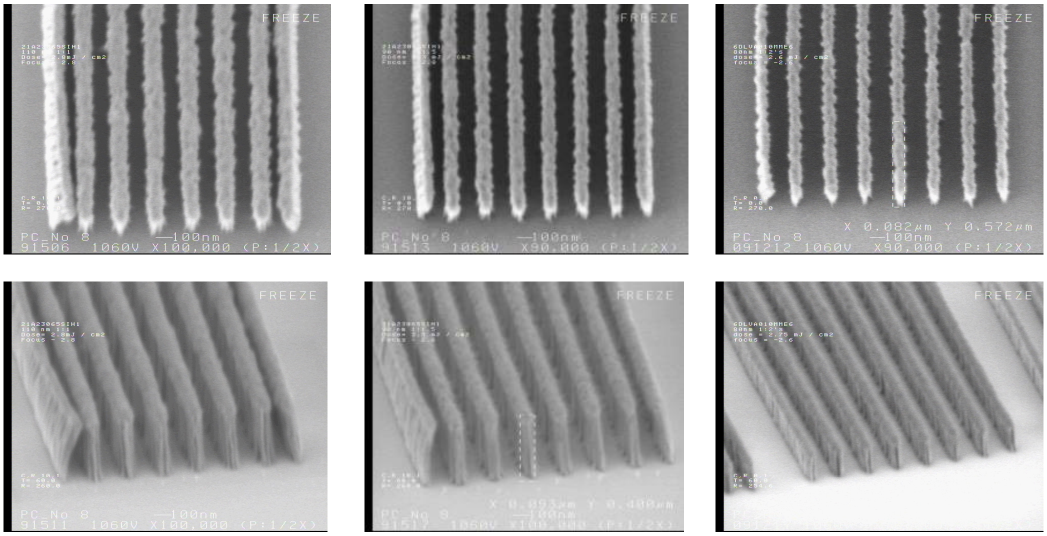

120 nm 1:1's, 400 nm tall 90 nm 1:1.5's, 400 nm tall 80 nm 1:2's, 300 nm tall

2.7 mJ / cm^2 3.3 mJ / cm^2 3.3 mJ / cm^2

Figure. 2.4: Top down and Tilted SEM of *t*BOC Styrene imaged with a binary mask at 157 nm.

This resist prints with rough sidewalls, but the aspect ratio is extremely high, and the resolution is near the limit of the tool with a binary mask.

Top Surface Imaging of PFAS

Previous work[7] with PFAS at 193 nm showed the ability to print high-resolution, high-aspect ratio images with extremely low Line Edge Roughness (LER). The extremely low LER of this system was attributed to two advantageous material properties: low opacity and a high Tg of the silylated polymer (~105°C). At 157 nm the opacity of the resist is higher, as can be seen in Fig. 2.3, and as such, the effects of the wavelength change are unclear. Fortunately though, the glass transition temperature is above the temperature of the silylation step.

PFAS was formulated with 4% TPS-Nf (wt PAG / wt Poly) and 10% trioctylamine (moles base / moles PAG). PAB and PEB were both run at 90°C for 60s. The resist was silylated at 90°C for 300s at 40 torr DMADMDS. The resist was imaged at 157 nm using a binary mask and the resulting images are shown in Fig. 2.5.

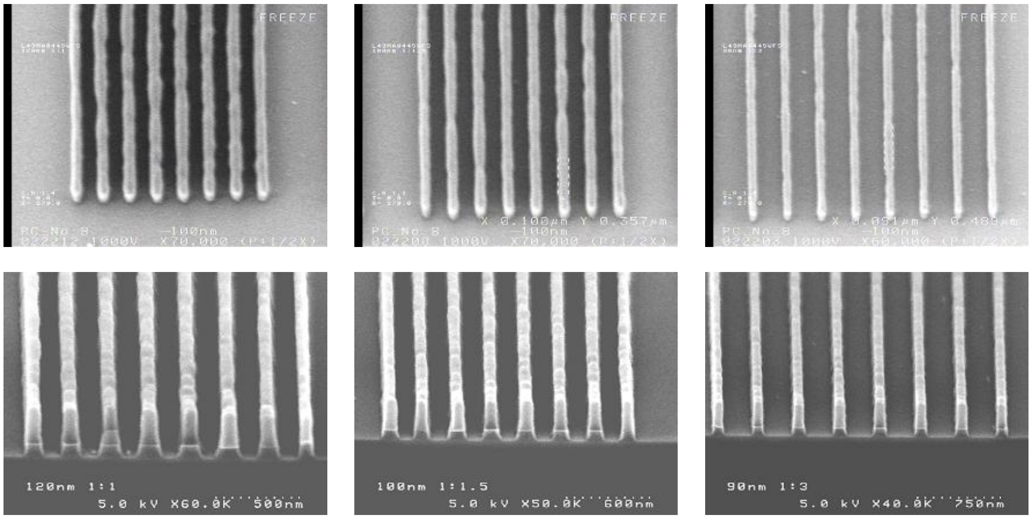

120 nm 1:1's 100 nm 1:2's 90 nm 1:3's

Figure 2.5: Top down and Tilted SEMs of PFAS imaged at 157 nm with a binary mask. All features are 270 nm tall

The imaging quality is excellent and the edges are relatively smooth. The images show some low-frequency LER, but the high-frequency roughness that is characteristic of most TSI systems is not present. The dose required to print these images is between 80- 110 mJ / cm^2. The process hasn't been optimized, (in fact these images were taken from the second wafer we processed at high doses), and it is likely that with optimization of the bake temperatures and etch conditions, the low-frequency roughness can be overcome. Overall, these images show that printing smooth lines with TSI at 157 nm is possible.

Top Surface Imaging of Poly(NBHFA)

Poly (NBHFA) is a material that was generated as a byproduct of our 157 nm single-layer resist program. It has promising material properties in that it has high silicon content after silylation (15.5% wt), is more transparent than PFAS, (see Fig. 2.3), and has a high Tg in its silylated state (nearly all homopolymers of norbornenes have high Tgs).

In order to insure that poly (NBHFA) deprotected and silylated properly, we first studied the silylation of the material with IR. Poly (NBHFA) was formulated with 6% TPS-Nf (wt PAG / wt Poly) and 10% trioctylamine (moles base / moles PAG). The resist was coated, baked, flood exposed at 248 nm, and silylated. PAB and PEB were both run for 60s at 130^{o}C. Silylation was at 90^{o}C for 120s with 40torr DMADMS. The infrared spectrum of poly (NBHFA) was collected after the PAB, after the PEB, and after silylation. The resulting spectra are shown in Fig. 2.6. The complete disappearance of the carbonyl peak at ~1770 cm^{-1} coupled with the appearance of the OH peak at ~3500 cm^{-1} after exposure indicates complete deprotection, and the appearance of the Si-H peak at ~2100 cm^{-1} in the silylated spectra accompanied by the complete disappearance of the OH peak at ~3500 cm^{-1} indicates complete silylation. Analogous spectra of *t*BOC Styrene and PFAS have been published previously[7,12]).

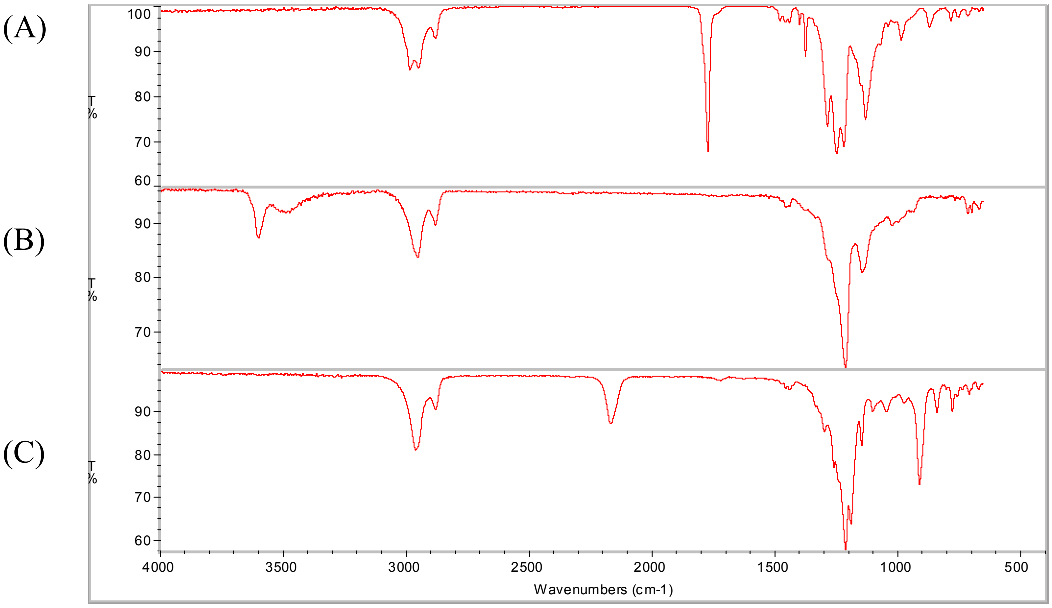

Figure 2.6: Infrared Spectra of poly (NBHFA) (a) after coating, (b) after exposure and PEB and (c) after silylation with DMADMS.

The resist was imaged at 157 nm using an alternating aperture phase-shifted mask and the resulting images are shown in Fig. 2.7. Process conditions were the same as described for the IR experiment, the only exception being the use of DMADMDS instead of DMADMS. Unfortunately, the images printed with rough sidewalls. Imaging the resist at 193 nm, where the polymer is essentially completely transparent did not help. These results indicate that a high Tg, and transparency may be necessary, but not sufficient, material properties for smooth imaging. This material has some, but not all of the attributes required for 157 nm TSI applications. This issue will be discussed in the ensuing chapters of the dissertation.

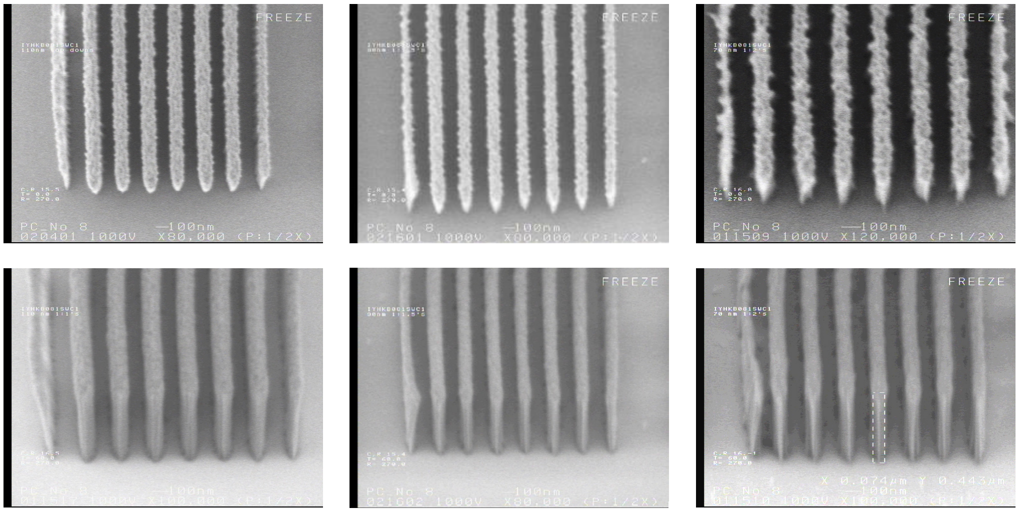

110 nm 1:1's 90 nm 1:1.5's 70 nm 1:2's

Figure 2.7: Top down and Tilted SEMs of poly (NBHFA) imaged at 157 nm with a phase-shifted mask. All features 450 nm tall.

Contrast Curves

Generation of contrast curves

In order to gain a better understanding of the fundamental behavior of these TSI systems, contrast curves were generated through each step of the process by recording film thickness as a function of dose. It was verified that thickness changes correlate nearly exactly with changes in the chemical composition of the film by IR, by either monitoring the growth of the Si-H peak (at ~2100 cm^{-1})or by monitoring the loss of the carbonyl peak, (the thickness changes were not the result of density changes). Thickness was measured with an interferometer in each field of a 10 x 10 array after each of the following steps: PAB, PEB, silylation, 10s etch, 50s etch, and 110s etch. Flood exposures were performed at 248 nm where all three polymer systems are transparent. These curves are presented as Figs. 2.8, 2.9 and 2.10. Using an ellipsometer, it was found that the Cauchy coefficients varied little through deprotection and silylation, and as such, Cauchy coefficients for the protected compounds were used. All process conditions (formulation, PAB, PEB, silylation, etc) were the same as those used for imaging, with the exception of the *t*BOC Styrene, where 2% TPS-Nf was used for contrast curves instead of 4% DPI-Nf.

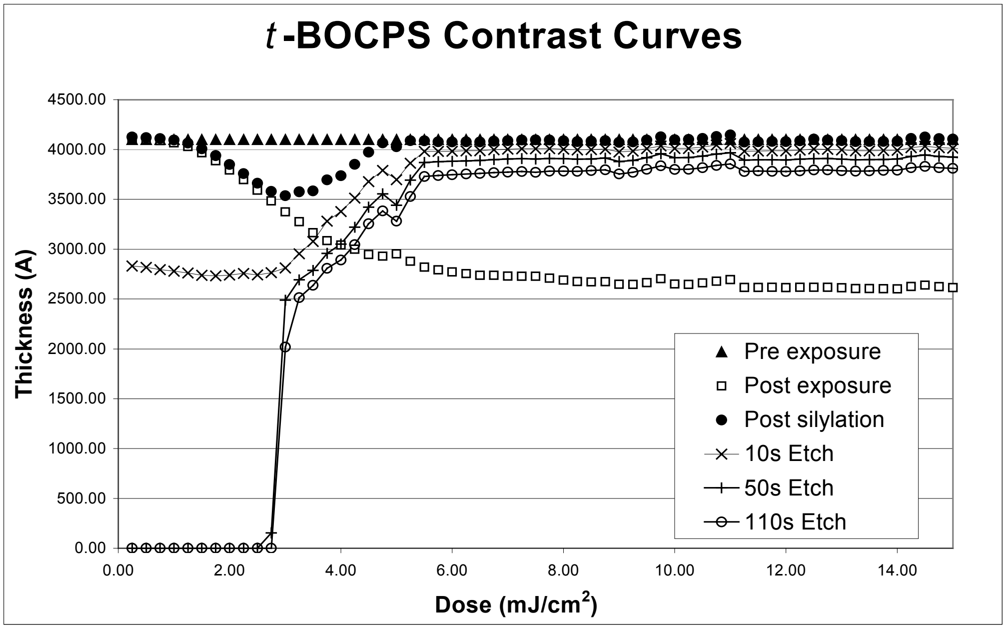

Figure 2.8: Contrast curves for *t*BOC Styrene

Discussion of **t***BOC Styrene contrast curve*

These curves show a number of interesting aspects of this system. The chemical amplification step of this resist generates excellent contrast, as can be seen by the sharp thickness loss after exposure greater than ~1 mJ / cm^2. The silylation of this resist also enhances the contrast of the system. Until the resist is ~50% deprotected, the silylation agent does not permeate into the film (as can be seen by the lack of thickness increase upon silylation at doses of less than ~3 mJ / cm^2). However, above 50% deprotection, the silylation agent readily permeates and reacts with the film. This is the only system that we have seen that exhibits this “silylation contrast” behavior. As is usually the case, *t*BOC Styrene shows great contrast in its final etch step. The overall contrast in this system is excellent.

The very high silicon content of the PHOST silylated with DMDSDMA (27 wt %) results in an extremely low etch rate of the silylated resist. The blanket etch rate of the silylated resist after the silicon dioxide etch mask has been formed is ~ 0.2 nm / s. The blanket etch rate of the protected polymer is ~13 nm / s. This excellent etch contrast enables the TSI system to function at wavelengths where the resist is nearly opaque since the light (and hence deprotection and silicon incorporation) does not need to go very deep into the film for an adequate etch barrier to be formed.

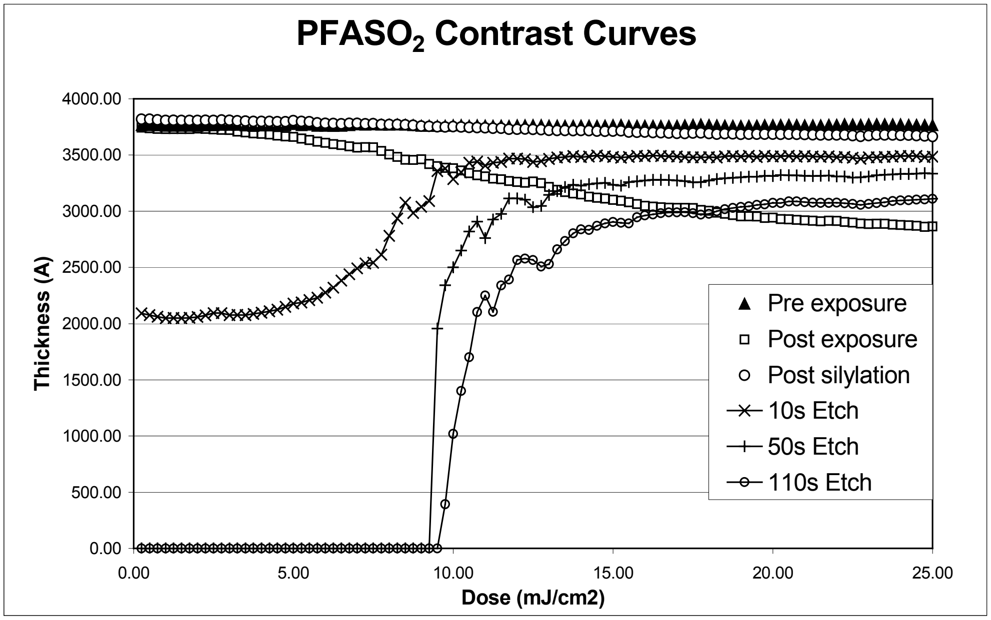

Figure 2.9: Contrast curves for PFAS

Discussion of contrast curves for PFAS

The contrast curves of the PFAS system reveal a number of interesting aspects. First, the thickness curve after exposure and PEB shows that the deprotection step of this polymer is extremely slow. Typically, one would expect to see a much sharper transition, and this result is very puzzling. This curve was replicated by looking at the carbonyl peak in the IR across all the fields and by synthesizing a second batch of polymer that was more rigorously neutralized after polymerization than that described by Ito *et al*[13]. This poor deprotection contrast might be related to the relatively low PEB temperature of 90°C, but since the polymer begins to decompose at higher temperatures, it is not appropriate to run it at higher temperatures.

The post-silylation curve of this polymer indicates that no “silylation contrast” is present in the film, since the film fills back up to the initial thickness. Fortunately, the high etch contrast of system results in acceptable overall contrast in the system. The blanket etch rate of the silylated resist after the silicon dioxide etch mask has been formed of 0.4 nm/s is slightly higher in this system than in *t*BOC Styrene. The blanket etch rate of the protected resist is 17 nm / s.

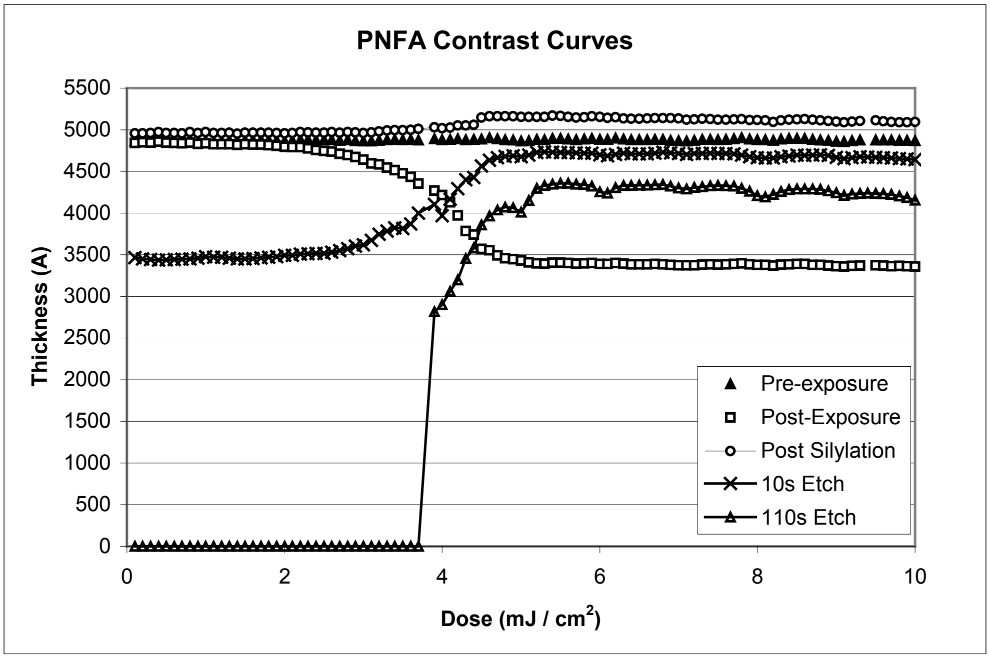

Figure 2.10: Contrast curves for PFNA

Discussion of contrast curves for poly (NBHFA)

The deprotection step in poly (NBHFA) generates sharp etch contrast at around 4 mJ / cm^2. The silylation step fills the image in to its original thickness, not enhancing overall system contrast. Finally the etch step enhances contrast, resulting in a sharp overall contrast at around 4 mJ / cm^2. The slow deprotection step that we saw in the PFAS has vanished by removing the SO_2 from the polymer backbone, and by raising the PEB temperature. The etch rate of this silylated polymer is still relatively high compared to *t*BOC Styrene, but the increased transparency and better contrast of the resist drops the imaging dose at 157 nm to a more reasonable level of ~15mJ / cm^2 for a binary mask.

CONCLUSIONS

TSI is a process that has the potential to overcome many of the challenges facing the lithographic community at 157 nm. It is capable of printing smooth, high aspect ratio, high resolution images that do not suffer feature collapse problems, while using polymers that are substantially more absorbing than those used in single layer applications. Until recently, TSI has had significant line edge roughness problems, but this might be overcome if the correct material properties are present in the polymeric resin (although these material properties are not yet fully understood). This paper demonstrates that TSI is capable of printing smooth images at 157 nm, and with proper development, could be a viable imaging alternative to single layer resists.

6. REFERENCES

---

(1) R. R. Kunz, T. M. Bloomstein, D. E. Hardy, R. B. Goodman, D. K. Downs, J.E. Curin, *Proc. SPIE* **3678**, 13 (1999)

(2) C. Brodsky, *et al*, *J. Vac. Sci. Technol.* B, **18 (6),** 3396-3401 Nov/Dec (2000)

(3) R. J. Hung, *et al*, *Proc. SPIE* **4345** (2001)

(4) A. P. Mahorowala, *et al. SPIE* **4343** (2001)

(5) J. Cobb, W. Conley, F. Huang, T. Lii, S. Usmani, S. Hector, W. Wu, *Proc. SPIE* **4345**, (2001).

(6) R. Sooriyakumanaran, D. Fenzel-Alexander, N. Fender, G.M. Wallraff, R.D. Allen, *Proc. SPIE* **4345**, (2001).

(7) M. H. Somervell, D. S. Fryer, B. Osborn, K. Patterson, C. G. Willson*, J. Vac. Sci. Technol.* B **18(5)**, 2551-2559 Sep/Oct (2000)

(8) W. D. Domke, V. L. Graffenberg, S. Patel, G. K. Rich, H. B. Cao, P. F. Nealey, *Proc. SPIE* **3999**, 313 (2000)

(9) S. A. MacDonald, H. Schlosser, N. J. Clecak, C. G. Willson, J. M. J. Fréchet, *Chem. Mater.* **4**, 1364 (1992).

(10) H. Ito, S. A. MacDonald, R.D. Miller, C. G. Willson, *U.S. Patent 4,552,83*, (1985).

(11) S. V. Postnikov, M. H. Somervell, C. L. Henderson, C. G. Willson, S. Katz, J. Byers, A. Qin, Q. Lin, *Proc. SPIE* **3333**, 997 (1998).

(12) S. A. MacDonald, H. Schlosser, H. Ito, N. J. Clecak, C. G. Willson, *Chem. Mater.* **3**, 435-442 (1991)

(13) H. Ito, N. Seehof, R. Sato, T. Nakayama, M.Ueda, *Micro- and Nanopatterning Polymers*, ACS Symposium Series **706**, 210-212

Chapter 3: Low-voltage Electron Beam Lithography Resist Processes: Top Surface Imaging and Hydrogen Silsesquioxane Bilayer.

ABSTRACT:

A Hydrogen Silsesquioxane (HSQ) bilayer process and a Top Surface Imaging (TSI) process have been investigated for application as low-voltage electron beam resist systems. Namatsu, van Delft, and others have reported printing exceptionally small features using high voltage electron beam exposure of HSQ at high exposure doses (~2000μC/cm^2 at 100kV). The shallow penetration depth of low voltage electrons results in greatly reduced dose requirements, and smooth, high resolution images were generated at 1kV with an exposure dose of less than 60 μC/cm^2. HSQ's high silicon content enabled it to be used in a bilayer form utilizing reactive ion etching with an oxygen plasma, thus generating high aspect ratio images. TSI has been studied in the past by numerous researchers at low-voltages using various TSI schemes. Here we investigate the use of a chemically amplified TSI resist process based on t-BOC Styrene. The effect of base quencher loading in the resist formulation on line edge roughness and resolution was investigated, and found to have dramatic influence. High resolution (40nm), high aspect ratio images were printed that exhibited only moderate levels of line edge roughness. Further, proximity effects and exposure latitude at 1, 2 and 3 kV were examined and compared to simulation.

INTRODUCTION:

a. Motivation for low-kV electron beam exposure tools

As feature sizes shrink, the demands on mask writing become increasingly difficult to meet. In particular, the popularity of optical proximity correction (OPC) has put tremendous pressure on the mask industry to accelerate their plan for shrinking of minimum feature sizes. Prior to OPC, the resolution of mask features was dictated by the reduction ratio of the lens systems, so the minimum mask feature size was approximately four times that of the chip generation. However, the writing of OPC features demands far higher resolution. Optical mask making tools are reaching their optical resolution limits, and electron beam systems are quickly becoming the tools of choice for the most demanding masks.

Traditionally, the resolution of electron beam systems has been improved by increasing the accelerating voltage. Higher energy electron beams have better resolution due to enhanced beam stiffness and the improved energy deposition profile within the resist. There are two aspects of electron behavior in a resist that dictate the energy deposition profile. The first, known as forward scattering, occurs when the electrons are scattered as they travel through the resist. The second, backscattering, is the result of electrons that scatter off the substrate and expose the resist as they exit the material. Increasing the exposure energy reduces the range of forward scattering but also increases the range of the backscattered electrons. Fortunately, a process of dose modulation called proximity correction can largely compensate for the backscattered component, but it is a computationally intensive and time-consuming process. A way of circumventing this process would be very valuable. In addition, the capture cross-section of materials is inversely proportional to the accelerating potential, which results in much lower sensitivity of resists.

One way to solve the problems of low resist sensitivity, and proximity correction in electron beam systems is to lower the accelerating voltage dramatically (to 1-3keV) to the point where the forward scattering and backscattering ranges are smaller than the feature size [1-5]. The low penetration depth of electrons within a solid at these voltages makes proximity corrections unnecessary, [6, 7] and results in very high sensitivity. In addition, the low voltages within the column make it particularly amenable for use in micro-column form, allowing the design of multiple beam writing systems[8-10]. Charge induced pattern distortion is a potential issue associated with low-voltage electron beam lithography[11-13] , although many ways exist to circumvent this issue by imaging near the cross-over energy, or by altering the cross-over energy of a resist film through the use of additives.

A major difficulty associated with low voltage imaging is the development of a suitable resist process. The low penetration depth of the electrons necessitates the use of a thin film imaging technique to generate features with sufficient etch resistance for subsequent etch transfer steps. In addition, the resist must have sufficiently high resolution to meet the demands of future imaging processes, while maintaining extremely low levels of line edge roughness. Many researchers have investigated this topic[14-19]. Top Surface Imaging and a bi-layer resist scheme employing a thin, (~20nm thick) hydrogen silsesquioxane imaging layer atop a novolac transfer layer are promising candidates for this application.

b. Hydrogen Silsesquioxane

Hydrogen Silsesquioxane (HSQ) is a material that is typically used for spin-on-glass applications. It has been commercialized by Dow-Corning under the trade name FOx (standing for Flowable Oxide). FOx solutions are available with varying concentrations of HSQ dissolved in methylisobutylketone (MIBK). The chemical structure of HSQ shown in figure 3.1. As can be seen, it is basically a cross-linked silicon dioxide cage structure, with reactive Si-H bonds on the corners. The material cures at high temperature, releasing H_2, and forming a film of porous silicon dioxide[20, 21]. The Si-H bonds are very reactive, and as such, the resist is sensitive to contamination. The material should not be stored in glass- it should only be stored in poly-ethylene or fluorocarbon bottles at low temperatures.

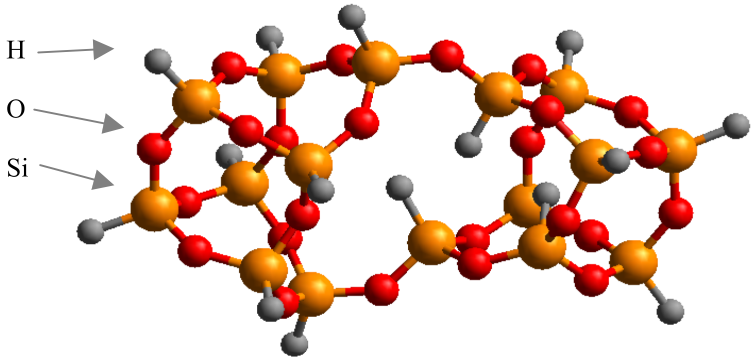

Figure 3.1: Chemical structure of HSQ.

The substantial chemical structure change that occurs during curing of HSQ led researchers to investigate its utility as a resist. Its very high silicon content made it even more appealing because of its potential as a top layer in a bilayer process. In 1998, Namatsu published the surprising result[22] that the unexposed resist dissolves in traditional base developer, and demonstrated the functionality of HSQ as a resist. Namatsu, Maile, van Delft, and others have printed very high-resolution features in HSQ with high-voltage e-beam exposure (50-100kV)[23-25]. Unfortunately, the resist requires unusually high dose in order to function at these voltages (up to >1000μC/ cm^2 at 50 kV[25]). This is likely due to the large number of cross-linking events required to render the resist insoluble coupled with the lack of chemical amplification. The dose can be decreased through the use of a photo-base generator, as was demonstrated by Harkness et al[26], although this study used organic developers, such as MIBK, n-octane or toluene.

c. Top Surface Imaging

Top surface imaging (TSI) is a promising technique for use as a low kV resist process. The fundamental idea behind TSI is that a single resist film is coated on a substrate, and exposed to light or electrons in such a way that only the top of the resist is chemically altered (either by working at a wavelength at which the resist absorbs, or at an electron energy where the penetration depth is shallow). The resist is then put in the presence of a silylation agent, which causes silicon to be incorporated into either the exposed or unexposed region. The film is then etched in an oxygen plasma, where the incorporated silicon acts as a hard mask, protecting that region.

The traditional problem associated with TSI is line edge roughness (LER). LER in TSI systems is quite a complicated and involved subject. Recent research has shown that LER in TSI systems can be overcome [27]. These experiments strive to determine if TSI has the appropriate resolution capabilities for electron beam applications, and to investigate the factors that influence that resolution. As such, we focus on a traditional TSI system that is easier to work with than those that have minimal LER for the sake or efficiency. Thus, the LER of these images isn't indicative of the absolute limits of TSI. Numerous researchers have investigated the application of TSI to low-voltage electron beam lithography [14, 17, 19].

EXPERIMENTAL AND MATERIALS:

a. Exposure Conditions and Metrology

Imaging was performed on a Raith 150 electron beam exposure tool, which is capable of high resolution at voltages between 500 V and 30kV. The imaging was performed in a vector mode (the beam is electronically positioned at each location and then un-blanked for a single exposure for a designated duration and current). Typical imaging conditions were a step-size of 5 or 10 nm, and a current of 7-10pA. During exposure the aperture was 7.5 um and minimum blanker time was 100ns. Beam focus, aperture alignment and astigmatism were performed on 40nm and 100nm gold nanoparticles that were placed on the wafer. Beam spot sizes at 1, 2 and 3kV were measured to be below 10nm. 248 nm imaging was performed at International SEMATECH on a SVGL Micrascan III using a binary mask (NA = 0.6, $\sigma = 0.6$). Top-down metrology was performed on the Raith 150, or on a Joel Tilt SEM. Critical dimensions were measured using a signal-averaged linescan coupled with a threshold protocol (typically, 8 lines were scanned and averaged for each data point). Cross-section SEMs were made using a Hitachi 4500 and a Hitachi S-4700.

b. Processing Conditions and Materials

A solution of FOx-14 was purchased from Dow-Corning, and diluted with semiconductor grade MIBK in order to facilitate spin coating at a thickness on the order of 20- 30nm (~13 wt.% FOx-14). The thickness was measured with a Tencor Alpha-step profilometer that was calibrated at the beginning of the study. The diluted FOx was contained in fluoro-polymer or poly-ethylene bottles to avoid degradation, or else diluted in glass immediately prior to coating. The post apply bake was 5 min. at 120°C. Development was performed in two steps: 1min. in Shipley LDD-26W, and 10sec. in 1:9 LDD-26W:H20, followed by rinse and dry as described by Van Delft in Ref. [25]. The bottom layer used in bilayer imaging was the bottom resist used for Infineon's 248nm CARL process. It was coated at varying thicknesses (between 400 and 100nm), and baked for 1min at 140°C, followed by 5min at 250°C.

t-BOC styrene was synthesized as described in chapter 2. The post apply bake was 1 min. at 100°C. The post exposure bake was 1min. at 90°C. Silylation was performed on Genesis Microstar 250 using 30 torr of Dimethylaminodimethylsilane (purchased from Silar Laboratories) at 90°C for 1 min.

The etch process was performed on a PlasmaTherm 760, with a chuck temperature of -40°C, operated at a top and bottom power of 100W and 800W, respectively. The pressure was 5 mTorr, with a flowrate of 40/10 sccm O_2/He respectively. The etch duration was calculated based on measured etch rates plus 30% over etch. Etch work for the optical exposures was performed at International SEMATECH using a Lam 9400 SE operated with a top and bottom power of 260W and 75W respectively. The pressure was 2.5mTorr with an oxygen flowrate of 60sccm and a chuck temperature of -25°C.

RESULTS AND DISCUSSION:

a. HSQ Single Layer Imaging

Initially, the HSQ resist was imaged as a single layer in order to determine imaging performance without the added complication of the etch transfer step. The resist was coated at a thickness of 33nm, and exposed between 40 and 90 μC / cm^2 at 1kV. The imaging results are shown in figure 3.2a. The resist suffered from significant levels of adhesion failure and delamination. This is in accordance with the simulated penetration depth of the electrons within the resist. The electrons do not penetrate the full thickness of the film. They only insolubilize the top of the resist, and the developer is able to dissolve out the underlying underexposed resist. The resist was then coated at a thickness of 24nm, and exposed at 1kV. A resulting image is shown in figure 3.2b. The resist performed well, with very low line edge roughness, and fairly high resolution, down to 30nm for nested features. (The low contrast of the SEM results from the fact that it is of ~20nm features of basically SiO2 on a wafer surface of native oxide, and therefore we have very little topographical or elemental contrast.)

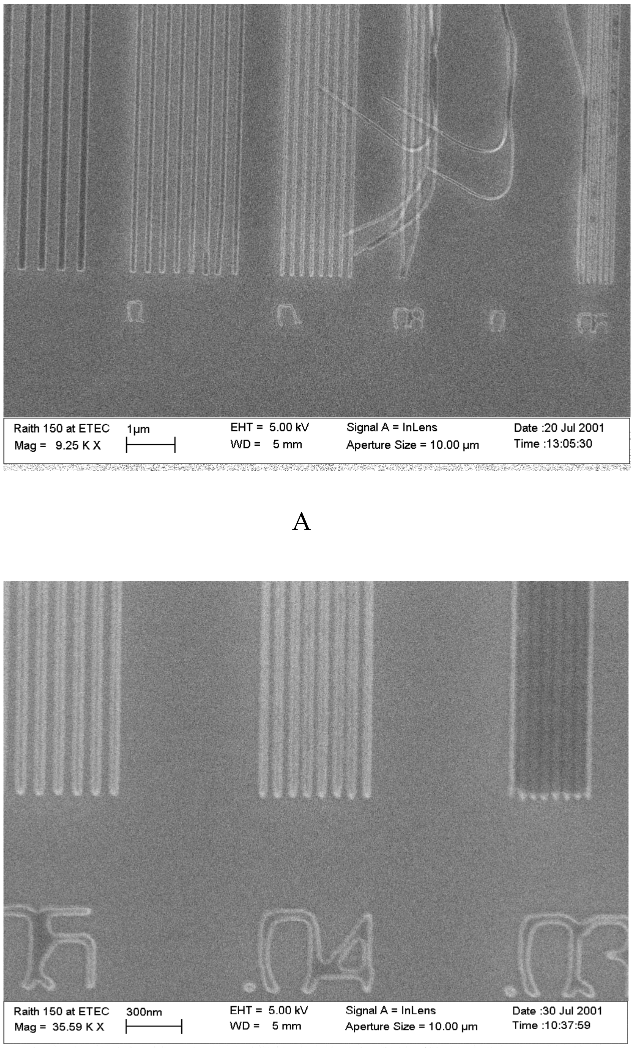

A

B

Figure 3.2: HSQ images generated at 1kV. a) 33nm thick resist exposed at 44µC / cm^2; note the inadequate penetration of the 1kV electrons into the resist, resulting in delamination. b) 24nm thick resist exposed at 40µC / cm^2. Image shows 50, 40 and 30nm lines on a 1:1 line:space pitch.

b. HSQ Bilayer Imaging

Once a satisfactory process was developed for the HSQ in single layer experiments, the work on the bilayer stack was undertaken. The etch rates of the top and bottom layers were measured, and found to be <2Å/s and ~180Å/s, respectively. A layer of 20nm of HSQ was coated on 180nm of image transfer layer, and exposed at 1, 2, and 3kV. The stack was developed, and etched for 13s. The resulting images are shown in figure 3.3. The resist printed exceptionally smoothly, and produced very high aspect ratio features. Figure 3.3b shows feature collapse that occurs at this tight pitch and high aspect ratio. Resist feature collapse in wet-developed systems is attributed to capillary forces. In this case, since the high aspect ratio features dry-developed in an etcher, the cause isn't immediately obvious. It is likely the result of condensation on the wafer that was still cold when removed from the etcher, or possibly intermolecular forces. The undercutting is the result of an un-optimized etch process, which could be fixed.

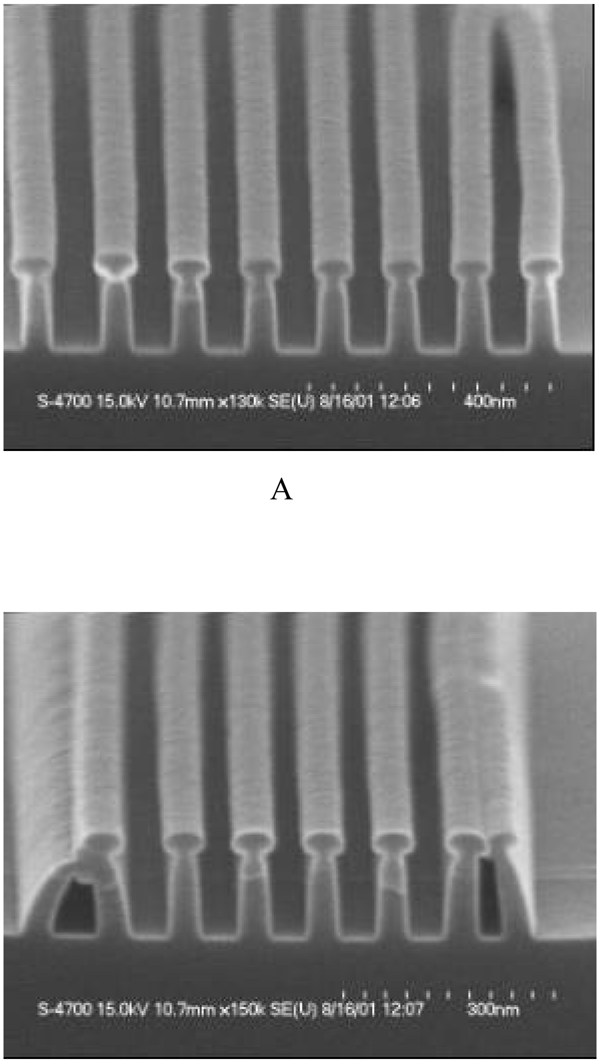

A

B

Figure 3.3: 60nm and 50nm nested features.

c. HSQ Proximity Effects

In order to investigate proximity effects in low-voltage electron beam systems, isolated and nested 70nm features were patterned under the same bilayer conditions that were described in Section 3b. The line-width was measured as a function of dose, and the results are presented in Fig. 3.4. Data were compared with simulated energy distribution profiles, which are shown in figures 3.5 a,b, and c. The thickness of the imaging layer is substantially thinner than the electron penetration depth at 2 and 3 kV. It is therefore likely that this condition results in a lower level of proximity effect, and a higher dose-to-size compared to a thicker film.

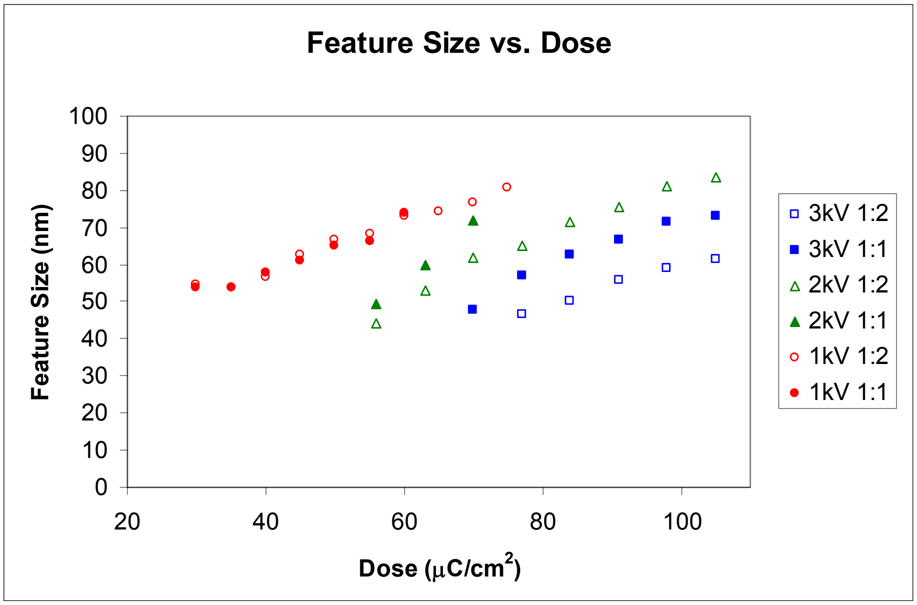

Figure 3.4: Line-width vs. Dose for nominal 70nm isolated and nested lines exposed at 1,2 and 3 kV.

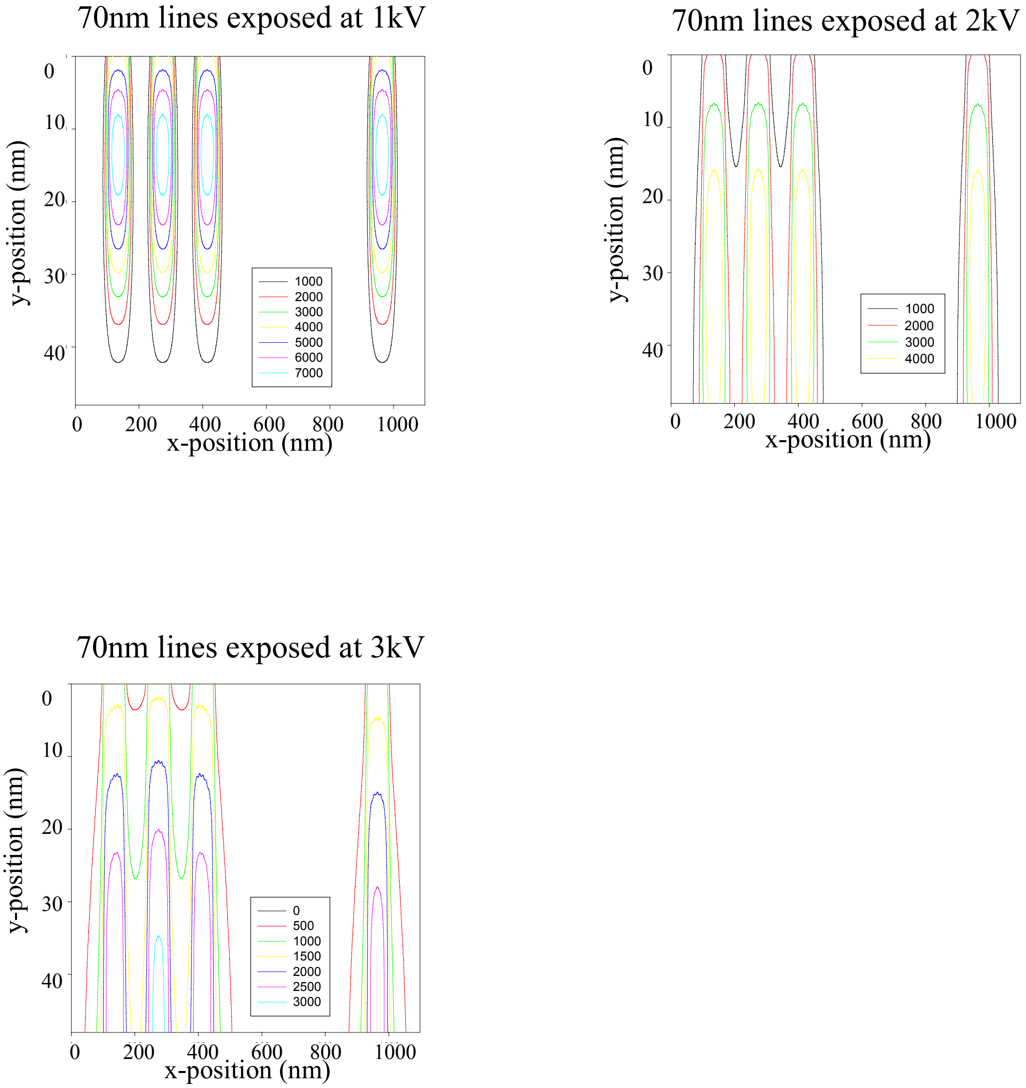

Figure 3.5: Energy deposition profiles of 1,2 and 3 kV electrons in HSQ. Nested lines are on the left; isolated are on the right (Units on energy contours are J / cm^3 for a dose of 30 μC / cm^2).

Resist exposure simulations were done using the Monte Carlo method of K. Kim[28] which has been shown to give results that agree with experiments at low electron energy, (<3keV). The method calculates the point spread function for the structure and materials used. Once the point-spread function has been calculated it is convolved with the spot shape to determine the instantaneous dose of the electron beam. Summing the spots that would be exposed then creates the pattern. In this case, a two-dimensional profile of lines and spaces was created. The input that produced figure 3.5 assumed the spot to have a Gaussian profile with a FWHM of 10nm and the spot was stepped with a 5 nm grid spacing to create the 70nm lines. Figure 3.5 shows the energy deposition contours for 70nm lines and spaces at 1, 2, 3 keV.

The low penetration depth and short scattering length of low voltage electrons has been shown to minimize proximity effects. The simulations in figure 3.5a, b, and c predict proximity effects to appear at 70nm feature width starting somewhere around 2kV, as evidenced the onset of wider energy deposition contours of the electrons within the nested features. If a simple threshold model for development is assumed (meaning that below a certain critical deposition energy, the resist will dissolve completely, and above that energy, the resist will not dissolve at all), it is possible to predict the iso-nested bias from the critical deposition energy at a given depth within the resist (preferably the widest point in the energy deposition profile). The predicted iso-nested bias is compared with the experimental data in Figure 3.3. Table 3.1 below shows these results.

Table 3.1: Proximity effect induced iso-nested bias: simulated vs. experimental.

	Predicted Iso-Nested Bias (threshold model) (nm)	Experimental Iso-Nested Bias (nm)
1kV	0	0
2kV	3	7
3kV	8	11

The model predicts the experimental trends, but underestimates the magnitude of the phenomenon. For 70nm features, proximity effects are not present at 1kV, begin to appear at 2kV and increase at 3kV. It is likely that the discrepancy in magnitude results from the threshold development rate assumption.

d. Exposure Latitude

A comparison can be made between predicted and experimental exposure latitude in many ways. At one end of the spectrum, a threshold model can be evoked, as was done in the previous section. At the opposite end of the spectrum is the complete model of the entire lithographic process. A rigorous model is not available, but by using the "log-slope method", one can compare theoretical and experimental exposure latitude, and gain some insight into resist performance. The log-slope method uses the normalized image-log-slope, or NLS (defined in Eq. 3.1 below) evaluated at the nominal feature edge as the metric for the imaging conditions.

$$NLS = w\frac{d\ln I}{dx} \tag{3.1}$$

In the equation above, *w* is the nominal line-width, *I* is the intensity, and *x* is the horizontal position. In general, the exposure latitude (EL) for a given imaging system can be related to the NLS by the relationship in Eqn. 3.2.

$$EL = \alpha(NLS - \beta) \tag{3.2}$$

In the above equation, α and β are adjustable parameters that vary from resist to resist and are process dependent. The parameter α is the minimum NLS for which a resist is able to resolve a pattern, and β is the percent change in exposure latitude per unit change in NLS. Typically, the EL is defined as the exposure latitude for which the developed line-width is within ±10% of the target line-width. For an ideal resist, α is 10, and $\beta=0$, and the performance of a resist can be measured by how close it is to these values. A typical resist has values of $\alpha = 8.1$, and $\beta=1.1$. The reader is referred to ref [29] for a thorough discussion of the image-log-slope method.

In optical systems, where this technique has been traditionally applied, the NLS is calculated from the aerial image at the point that is at the air-resist interface and nominal feature edge. At the air resist interface, the intensity of the aerial image is at its highest (optical absorption in the film has not occurred yet), and the NLS is at its highest. In order to apply the relationship to the low-voltage electron beam situation, the natural place to evaluate the NLS is still at the nominal feature edge, but at the depth where the energy deposition profile is at its widest. The imaging behavior of the system is dictated by what is occurring at this point, since the energy deposition is drastically higher than at the air-resist interface. The intensity at a fixed depth was extracted from the simulations, and the NLS was calculated. For 1kV, the depth used was 14nm; for 2 and 3 kV, the bottom of the resist film, or 20nm, was used. A typical fixed-depth energy deposition profile for nested 70nm lines at 1,2, and 3kV is shown in figure 3.6.

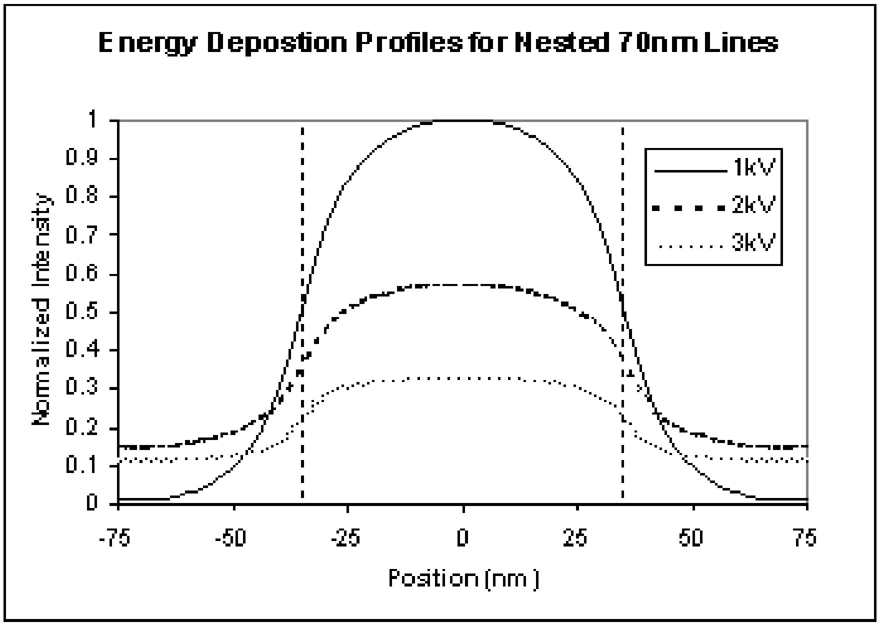

Figure 3.6: Energy deposition profiles at 1, 2, and 3kV (dotted lines show feature edge).

The experimental EL data is shown in Table 3.2, along with the predicted EL using a threshold model and the NLS model. Overall, the threshold model performed poorly, but the NLS model using typical resist parameters for α and β did a fairly good job.

Table 3.2: Experimental exposure latitude for various imaging conditions vs. theoretically predicted values

	NLS	Exp. EL (%)	Threshold Model EL (%)	Typical Resist EL (%) α=8.1, β=1.1
1kV (nested 30nm)	2.4	0	50	11
1kV (isolated 70nm)	6.3	44	65	42
1kV (nested 70nm)	6.3	44	65	42
2kV (isolated 70nm)	4.4	22	43	27
2kV (nested 70nm)	4.0	13	39	23
3kV (nested 70nm)	4.4	22	42	27

e. Effect of Base Quenchers on Top Surface Imaging Resolution and Line Edge Roughness

In formulating a traditional chemically amplified resist, one typically adds four components: polymer, solvent, photo-acid generator, and a "quenching" base. The polymer contains polar phenolic or carboxylic acid groups that are protected with acid labile protecting groups. The deprotection of these groups enables the solubility switch (and in this TSI system, generates a reactive –OH site). Within the exposed areas, the photo-acid generator produces a strong acid which catalytically deprotects numerous sites in the vicinity of where it was formed. The acid is thought to diffuse until the acid is either quenched by a basic site, or until it is trapped in a low diffusion area of the polymer. From a simplistic perspective, the quenching base decreases the number of deprotection incidents, thus pushing the required imaging dose to higher levels. Practically, many bases perform this action in a surprising way. Rather than changing the slope of a deprotection vs. dose curve, the base causes the initiation of the deprotection reaction to move to a higher dose. However, the slope itself doesn't change dramatically. The fundamental reason for this is likely the fast rate of the acid-base reaction relative to the deprotection reaction. The effect of this onset shift is extremely beneficial to resist performance since it serves to increase the contrast of the resist. The critical parameter for contrast in resists is the relative change in deprotection per *relative* change in dose, not relative change of deprotection per *absolute* change in dose. In mathematical terms, we care about I/ X (dX/dI), (equivalent to d lnX / d lnI), and not d lnX / dI, where X is the fraction of sites deprotected, and I is the dose. This increase in contrast greatly improves imaging performance of resists; it increases the resolution capabilities of a resist by allowing it to work with a lower image-log-slope (although these bases also may affect other parameters such as iso-nested bias). The influence of base quenchers on photoresists is further discussed in chapter 7.

In order to investigate the affects of additive base on the imaging performance of this TSI system, three formulations were tested at 248nm. Using a 248nm stepper at International SEMATECH, we were able to investigate LER and resolution more accurately than in the ebeam system due to the higher reproducibility of the 248nm aerial image as compared to that of the ebeam tool.

Three formulations of t-BOC Styrene were generated containing: 2wt% TPS-Nf / 10mol% TOA (mol% measured as base: PAG), 6wt% TPS-Nf / 30mol% TOA, and 6wt% TSP- Nf / 50mol% TOA. So, the ratio of overall base loadings was 1:9:15. The PAG loading was increased as well in order to keep the dose reasonable. These resists were then exposed at 248 nm to determine the effect on LER. The resulting 200nm images are shown in Figure 3.7. As can readily be seen, line edge roughness decreased as base loading increased. In fact, the high base loading resist was capable of resolving down to 160nm, far lower than the other two resists. Unfortunately, the high base resist required a dose of 115 mJ / cm^2, far higher than would be practical for application. However, as we shall see, at 1kV the shallow deposition profile decreases the required dose by so much that we can still work at a reasonable level compared to tradition electron lithography tools.

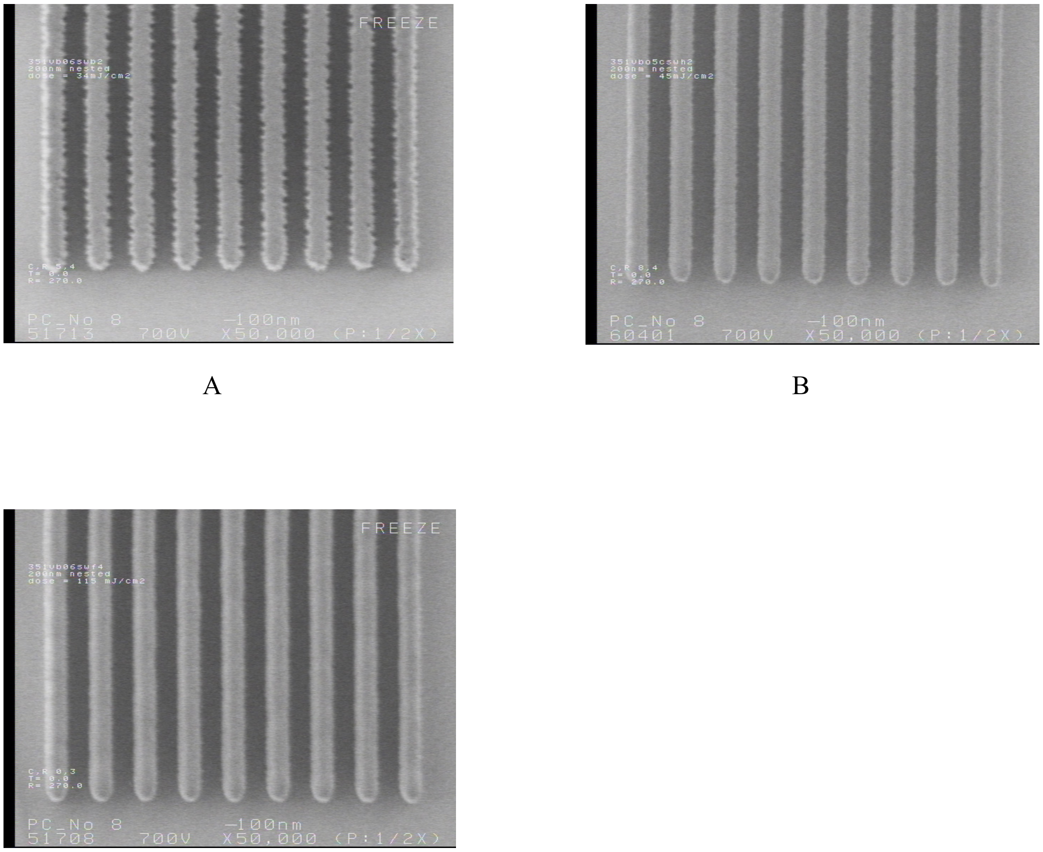

A

B

C

Figure 3.7: Effect of variable TOA and TPS-Nf concentration on LER. Nested 200nm lines exposed with 248nm illumination using a) 2wt% TPS-Nf / 10mol% TOA, b) 6wt% TPS-Nf / 30mol% TOA, c) 6wt% TSP- Nf / 50mol% TOA.

f. Low voltage electron beam exposure using TSI.

The high base formulation discussed in the previous section was exposed at 1kV. The resulting images are show in Figure 3.8. Two different thicknesses of resist were imaged in order to limit feature collapse at the smaller features. As can readily be seen, very small features were patterned, with only moderate levels of line edge roughness. Dose to size for all of these features was less than 6 μC / cm^2.

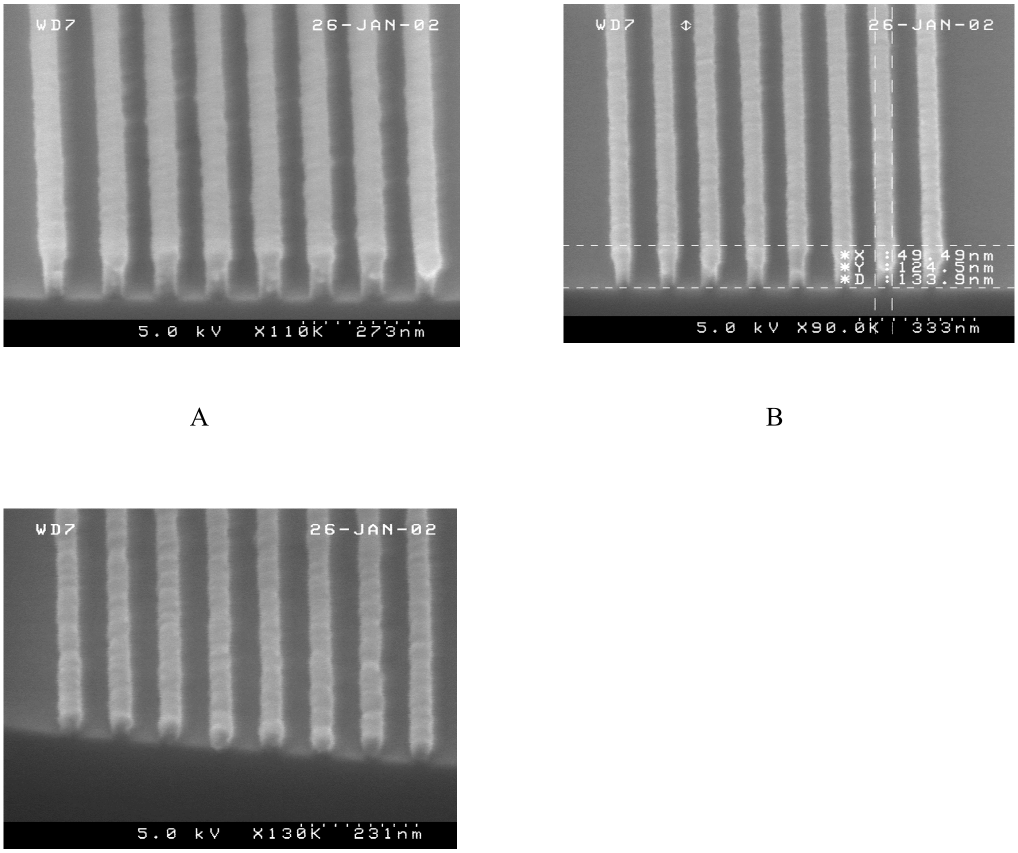

A

B

C

Figure 3.8: High resolution imaging using TSI at 1kV. a) 60 nm nested features in ~120 nm of resist, b) 50 nm 1:1.5 features in ~120nm of resist c) 40 nm 1:1.5 features in ~50nm of resist.

CONCLUSIONS

Low voltage electron beam imaging was investigated using an HSQ-bilayer resist platform and a TSI resist platform. High resolution, high aspect ratio patterns were generated that had extremely low line edge roughness using HSQ. At 70nm, 1kV imaging showed no evidence of proximity effects, where 2 and 3kV did show moderate levels. The results of Monte Carlo simulations were using the method of Kim were compared qualitatively with experimental results. Top surface imaging generated high resolution, high aspect ratio images with only moderate levels of LER, using a resist formulation containing high levels of quencher base.

References:

(1) Pease, R. F. W. *The IEEE 9th Annual Symposium on Electron, Ion, and Laser Beam Technology, Edited by RFW Pease (San Francisco, CA)* **1967**, 176.

(2) Yau, Y. W.; Pease, R. F. W.; Iranmanesh, A. A.; Polasko, K. J. *Journal of Vacuum Science & Technology* **1981**, *19*, 1048-1052.

(3) McCord, M. A.; Newman, T. H. *Journal of Vacuum Science & Technology B* **1992**, *10*, 3083-3087.

(4) Peterson, P. A.; Radzimski, Z. J.; Schwalm, S. A.; Russell, P. E. *J. Vac. Sci. Technol., B* **1992**, *10*, 3088-3093.

(5) Lee, Y. H.; Browning, R.; Maluf, N.; Owen, G.; Pease, R. F. W. *J. Vac. Sci. Technol., B* **1992**, *10*, 3094-3098.

(6) Polasko, K. J.; Yau, Y. W.; Pease, R. F. W. *Proc. SPIE-Int. Soc. Opt. Eng.* **1982**, *333*, 76-82.

(7) Stark, T. J.; Edenfeld, K. M.; Griffis, D. P.; Radzimski, Z. J.; Russell, P. E. *J. Vac. Sci. Technol., B* **1993**, *11*, 2367-2372.

(8) Chang, T. H. P.; Kern, D. P.; Muray, L. P. *J. Vac. Sci. Technol., B* **1992**, *10*, 2743-2748.

(9) Kratschmer, E.; Kim, E. S.; Thomson, M. G. R.; Lee, K. Y.; Rishton, S. A.; Yu, M. L.; Chang, T. H. P. *J. Vac. Sci. Technol., B* **1995**, *13*, 2498-2503.

(10) Kratschmer, E.; Kim, H. S.; Thomson, M. G. R.; Lee, K. Y.; Rishton, S. A.; Yu, M. L.; Chang, T. H. P. *Journal of Vacuum Science & Technology B* **1994**, *12*, 3503-3507.

(11) Kudryashov, V. A.; Krasnov, V. V.; Prewett, P. D.; Hall, T. J. *Microelectron. Eng.* **1997**, *35*, 165-168.

(12) Liu, W.; Ingino, J.; Pease, R. F. *J. Vac. Sci. Technol., B* **1995**, *13*, 1979-1983.

(13) Satyalakshmi, K. M.; Olkhovets, A.; Metzler, M. G.; Harnett, C. K.; Tanenbaum, D. M.; Craighead, H. G. *Journal of Vacuum Science & Technology, B: Microelectronics and Nanometer Structures* **2000**, *18*, 3122-3125.

(14) Boettcher, M.; Bauch, L.; Stolberg, I. *J. Vac. Sci. Technol., B* **1994**, *12*, 3473-3477.

(15) Lo, C. W.; Rooks, M. J.; Lo, W. K.; Isaacson, M.; Craighead, H. G. *J. Vac. Sci. Technol., B* **1995**, *13*, 812-820.

(16) Tanenbaum, D. M.; Lo, C. W.; Isaacson, M.; Craighead, H. G.; Rooks, M. J.; Lee, K. Y.; Huang, W. S.; Chang, T. H. P. *J. Vac. Sci. Technol., B* **1996**, *14*, 3829-3833.

(17) Whelan, C. S.; Tanenbaum, D. M.; La Tulipe, D. C.; Isaacson, M.; Craighead, H. G. *J. Vac. Sci. Technol., B* **1997**, *15*, 2555-2560.

(18) Schock, K. D.; Prins, F. E.; Strahle, S.; Kern, D. P. *J. Vac. Sci. Technol., B* **1997**, *15*, 2323-2326.

(19) Lee, K. Y.; Hsu, Y.; Le, P.; Tan, Z. C. H.; Chang, T. H. P.; Elian, K. *Journal of Vacuum Science & Technology, B: Microelectronics and Nanometer Structures* **2000**, *18*, 3408-3413.

(20) Siew, Y. K.; Sarkar, G.; Hu, X.; Hui, J.; See, A.; Chua, C. T. *J. Electrochem. Soc.* **2000**, *147*, 335-339.

(21) Belot, V.; Corriu, R.; Leclercq, D.; Mutin, P. H.; Vioux, A. *Chem. Mater.* **1991**, *3*, 127-131.

(22) Namatsu, H.; Takahashi, Y.; Yamazaki, K.; Yamaguchi, T.; Nagase, M.; Kurihara, K. *J. Vac. Sci. Technol., B* **1998**, *16*, 69-76.

(23) Namatsu, H.; Yamaguchi, T.; Nagase, M.; Yamazaki, K.; Kurihara, K. *Microelectron. Eng.* **1998**, *41/42*, 331-334.

(24) Maile, B. E.; Henschel, W.; Kurz, H.; Rienks, B.; Polman, R.; Kaars, P. *Japanese Journal of Applied Physics, Part 1: Regular Papers, Short Notes & Review Papers* **2000**, *39*, 6836-6842.

(25) van Delft, F. C. M. J. M.; Weterings, J. P.; van Langen-Suurling, A. K.; Romijn, H. *Journal of Vacuum Science & Technology, B: Microelectronics and Nanometer Structures* **2000**, *18*, 3419-3423.

(26) Harkness, B. R.; Takeuchi, K.; Tachikawa, M. *Macromolecules* **1998**, *31*, 4798-4805.

(27) Somervell, M. H.; Byers, J.; Willson, C. G. *Abstracts of Papers of the American Chemical Society* **1999**, *218*, 29-PMSE.

(28) Lee, Y.; Lee, W.; Chun, K.; Kim, H. *Journal of Vacuum Science & Technology B* **1999**, *17*, 2903-2906.

(29) Mack, C. A. *Opt. Eng. (Bellingham, Wash.)* **1993**, *32*, 3350-3362.

Chapter 4: Surface Energy Induced Low Frequency Line Edge Roughness in Top Surface Imaging

ABSTRACT:

Top Surface Imaging (TSI) is a lithographic technique that possesses many advantages over traditional processes. However, TSI suffers from the poorly understood phenomenon of line edge roughness. In this chapter, we propose that low frequency roughness in TSI systems is the result of the surface energy minimization of a low Tg polymer in a thermodynamically unstable geometry. We model the lithographic system as a truncated cylinder on a surface, and present a capillary instability analysis of two degradation pathways. Modeling demonstrates that in nearly all circumstances the geometries created in TSI are thermodynamically unfavorable.

INTRODUCTION

Surface energy induced instabilities occur in a variety of systems. The classic example of this phenomenon is the break-up of a liquid jet into small droplets; however, any system with the ability to flow is capable of minimizing its free surface energy and is therefore susceptible to this so-called Rayleigh or capillary instability. Interfacial instabilities have also been used to explain instabilities in numerous systems including, jets of liquid crystalline polymers[1], liquid metal in welding applications[2] and MEMs based atomizers[3] to name a few. One area where these phenomena are beginning to appear more regularly is nanostructures. Fundamentally, small-scale features (often created by lithography) have very large surface area to volume ratios. If the material can flow, the features have a tremendous driving force to rearrange themselves to minimize their surface free energy. This driving force dramatically increases as feature sizes decrease since the surface tension based Laplace pressure scales inversely with the radius of curvature of the feature. A good example of this phenomena was presented by Tanaka et al, who investigated degradations associated with the annealing of nanofabricated silicon structures, and attributed them to a Rayleigh instability[4].

In the semiconductor industry people strive to create very small features with sharp, uniform edges. Roughness in this edge is typically referred to as line edge roughness (LER). Top surface imaging (TSI) is an alternative lithographic process that has not been accepted into semiconductor manufacturing for various reasons, but one of the dominant problems associated with TSI is a large amount of LER. There have been many proposed explanations for LER in TSI systems[5, 6], but the problem has yet to be fully understood. Traditionally, line edge roughness has been characterized as either low or high frequency. High frequency LER is a very complicated phenomenon that has been studied extensively in both traditional wet-developed systems as well as in TSI systems[7-9]. Low frequency roughness is less well understood, but it is still a significant issue. Figure 4.1 shows a 120nm line and space pattern with a significant amount of low frequency LER. This paper seeks to explain this low frequency LER in terms of a capillary instability of the features that have been created by TSI.

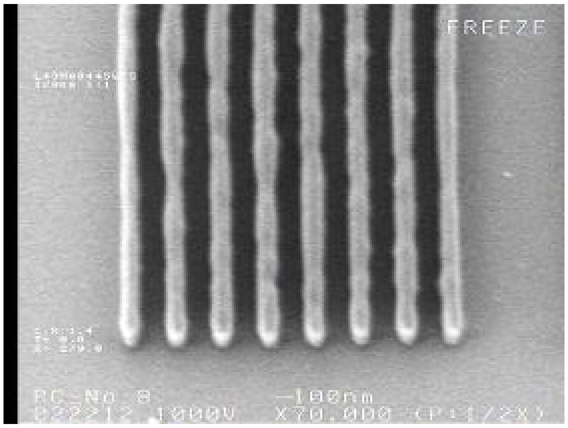

Figure 4.1. 120 nanometer lines and spaces generated with top surface imaging, showing significant low frequency LER [6].

A TSI process flow is shown schematically in figure 4.2. A single layer resist film is coated on a substrate and exposed to light or electrons, which chemically alters the film. If the resist is highly absorbing to the light, only the top portion of the resist is affected. Silicon is then selectively incorporated into the top portion of the film, often by exposure to a gas phase silylation agent. This process leads to a resist film containing silicon in the exposed regions and none in the unexposed regions (or vice versa, depending on the chemistry). The material is then etched in an oxygen plasma, where the incorporated silicon acts as a hard mask, providing etch resistance to the exposed regions. The fundamental advantage of TSI is that it works even when the photoresist is very absorbing to the wavelength of light to which it is exposed, making it easier to print using short wavelengths of light (thus enabling printing of smaller features, as dictated by the Rayleigh criterion).

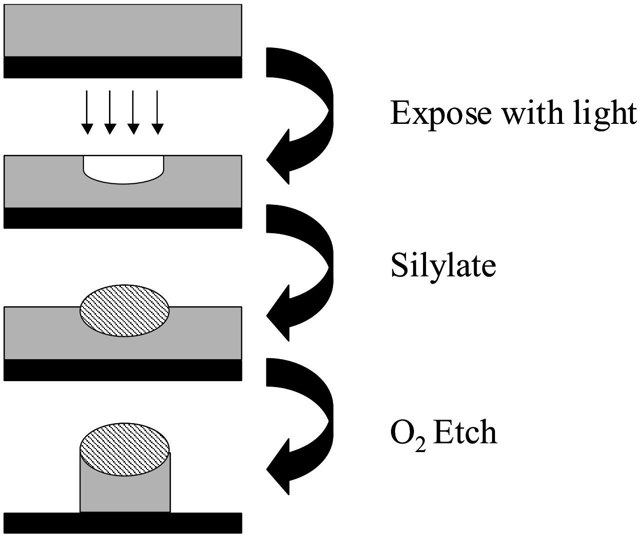

Figure 4.2. Process flow for a typical top surface imaging process. A resist film is coated, selectively exposed to light, silylated and Oxygen etched, forming high-resolution features.

As illustrated in Figure 4.2, the resist film often swells during the silylation step, creating a truncated cylinder of silylated polymer. Depending on the chemistry of the TSI system in use, this level of swelling can vary greatly. Figure 4.3 shows a cross sectional scanning electron micrograph of a group of lines that exhibit the swelling phenomenon prior to etch (the white caps are the silylated polymer).

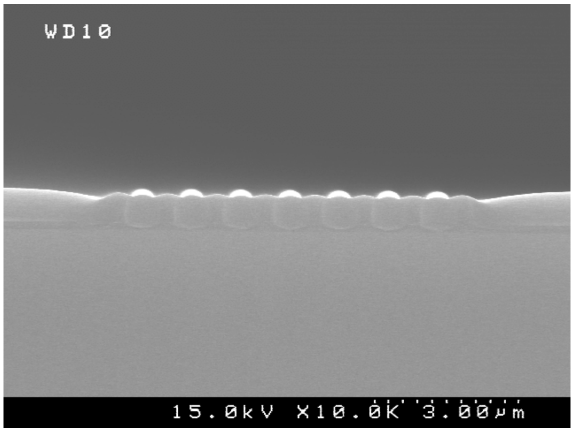

Figure 4.3. Scanning electron micrograph of a bank of lines prior to etch demonstrating the formation of truncated cylindrical cross-sections.

In order for a capillary instability to occur, the material must be sufficiently mobile to rearrange its surface. In the case of TSI, during the silylation step, the glass transition temperature (Tg) of the polymer greatly decreases, thereby lowering the polymer's viscosity[5]. Furthermore, an even lower Tg can be achieved during the etch process because oxidation of the silylated polymer can result in low Tg siloxane intermediates[10]. As the glass transition temperature of the silylated regions drops below the processing temperatures, the low Tg features gain the ability to flow; and the features thereby become susceptible to capillary instabilities.

This chapter seeks to explain low frequency line edge roughness in top surface imaging systems as a capillary instability of low Tg, silicon containing regions in the resist film. The system is modeled as a truncated, liquid cylinder bounded by a solid resist film below. Its stability to axial disturbances is tested by applying a low amplitude sinusoidal disturbance to the cylinder and examining the change in energy of the system.

Previous researchers have investigated similar geometries. Grinfeld[11] investigated a fixed and a variable footprint case with disturbances that allowed the radius of curvature to vary at a given cross-section, which does not closely match the observed phenomena in our small systems. Gratzke[2] investigated a fixed radius of curvature geometry that is similar to our system, but placed a disturbance the radius of curvature while allowing the width and the contact angle to float. Neither of these disturbances adequately described our observations.

In this work, two cases are examined. In the first case, the cylinder is assumed to have a fixed footprint on the resist film below. In other words, the bottom portion of the truncated cylinder is assumed to be in contact with a fixed portion of the underlying substrate. In the second case, the footprint of the cylinder is allowed to vary but the cylinder maintains a fixed contact angle with respect to the substrate. Figure 4.4 shows an example of each type of perturbation considered.

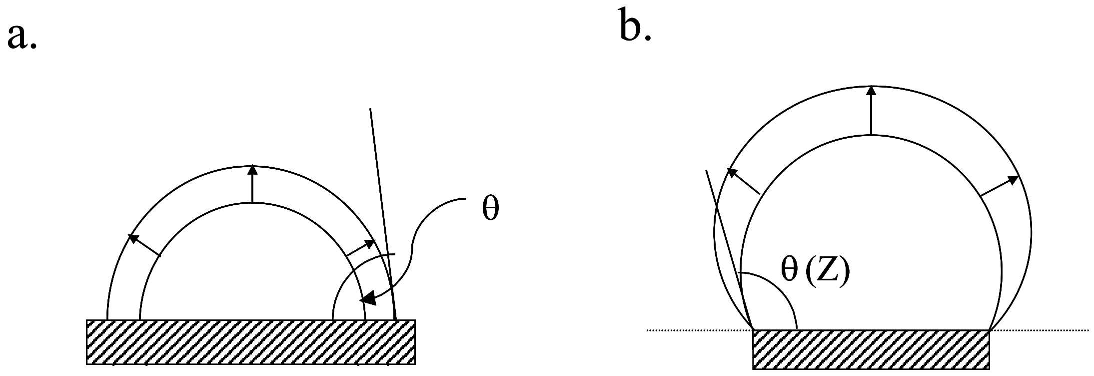

Figure 4.4. Two perturbations on a truncated cylinder: **(a)** a perturbation on the width of the cylinder footprint, with a constant contact angle, and **(b)** a perturbation on the contact angle of the cylinder, θ, on a fixed footprint.

EXPERIMENTAL SECTION

A traditional binary chemically amplified top surface imaging scheme based on the work of Somervell[5] was employed to generate the truncated cylinder topographies discussed earlier. TBOC styrene was synthesized and formulated in a propyleneglycol methylether acetate solution containing 2% (by weight) of the photo acid generator triphenylsulfonium nonaflate. The solution was spin cast on an anti-reflection coated silicon substrate using an FSI Polaris 2000 and post application baked for 1 min. at 100°C. The wafer was exposed at 248 nm on a SVGL Micrascan III using binary illumination (NA = 0.6, $\sigma = 0.6$). It was then post exposure baked for 1 minute at 90°C. Silylation was performed on a Genesis

Microstar 250 using 30 torr of dimethylaminodimethylsilane (purchased from Silar Laboratories) at 90°C for 1 min (or for 10 min in the long-time case). Scanning Electron Micrographs were produced on a Joel Tilt SEM, and a Hitachi S 4500. All processing and exposures were performed at International SEMATECH on 8 inch silicon wafers.

RESULTS

Two line space patterns were prepared by TSI. One was swollen by a small amount, whereas the other was swollen greatly. Figure 4.5 shows the results of these experiments. Figure 4.5a shows the truncated cylinder geometry at low levels of swelling. The lines appear smooth and uniform. Figure 4.5b shows lines that were allowed to swell. These lines are much less smooth and appear to have undergone an instability-based degradation. The results of this experiment tend to indicate that higher degrees of swelling lead to more susceptibility to capillary instability.

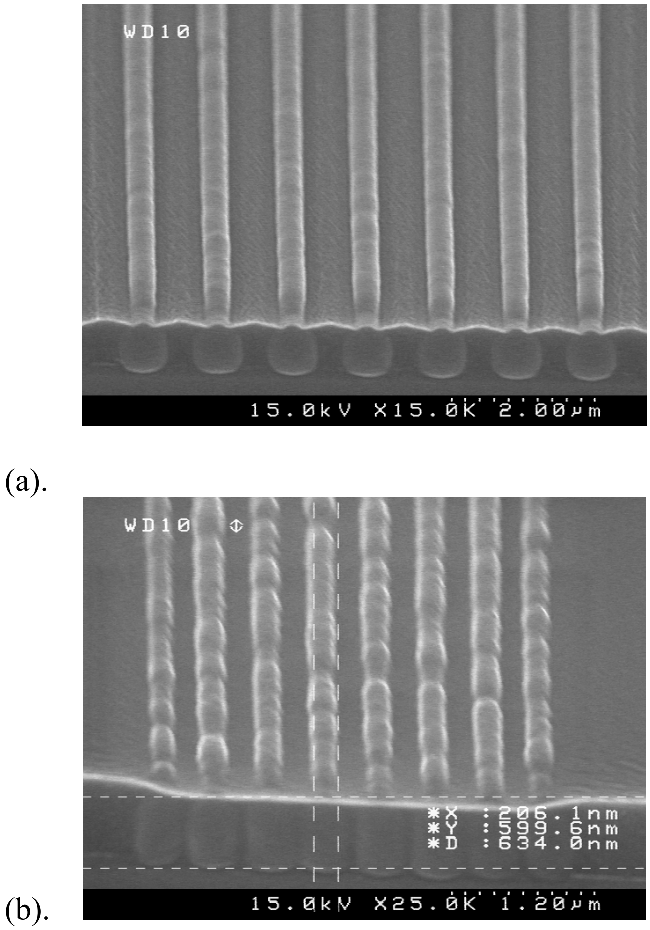

Figure 4.5. **(a)** A tilted cross-sectional micrograph showing smooth truncated cylinders created with TSI and **(b)** a tilted cross-sectional micrograph showing truncated cylinders at a larger level of swelling that appear to have undergone a capillary instability.

In order to demonstrate that this phenomenon was induced by capillary instabilities, an attempt was made to generate the results on a bulk scale. Liquid was placed in a trench with fluoropolymer surroundings. In almost all cases, the liquid immediately formed a single bulge at one place along the line. It became apparent that this was the stable equilibrium state. A TSI sample was held at high temperature for a long period of time to determine if it achieved the same geometry. The results are shown in Figures 4.6a and 4.6b.

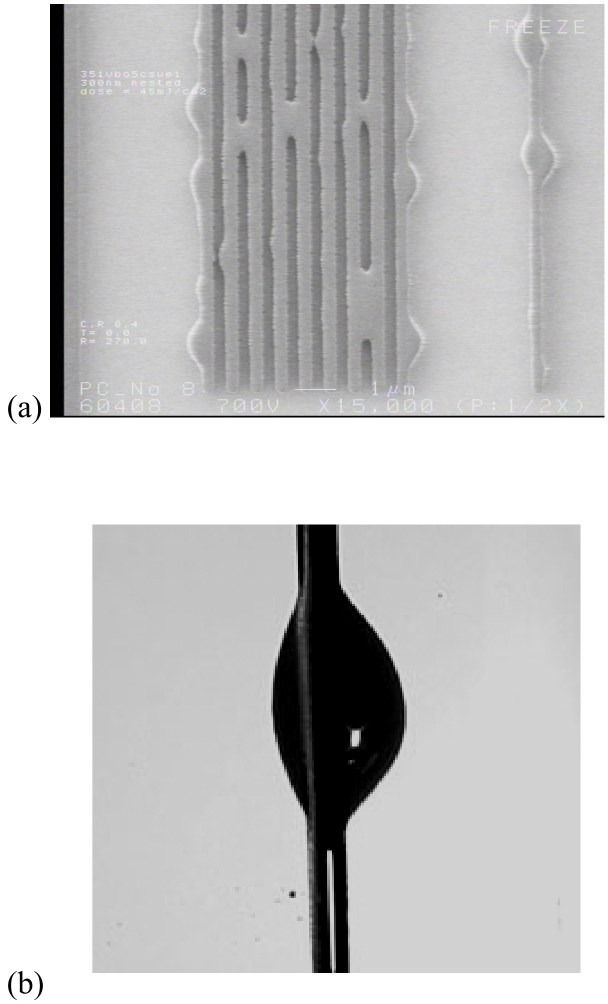

Figure 4.6. a) A SEM of a line space pattern created by TSI. This pattern was held at high temperature for a prolonged period of time, allowing the sample to achieve a more stable configuration. b) A photograph of water in a macroscopic fluoropolymer trench showing a similar stable configuration.

THEORETICAL ANALYSIS

Capillary instabilities are driven by the minimization of surface free energy in systems that are capable of flow. This phenomenon can be investigated by examining the energy of a system when subjected to a small perturbation. If the energy of the perturbed system is less than the energy of the unperturbed system, the perturbation will grow and therefore, the system is unstable and will tend to evolve to a lower surface energy state. The type of perturbation typically used for this type of analysis is a low amplitude sinusoidal variation in a variable that describes the geometry of the system. Because all perturbations can be broken down into a summation of sinusoids via Fourier transforms, this type of perturbation is generally applicable to any arbitrary disturbance or perturbation. In this specific case, the system of interest is modeled initially as cylindrical cap of liquid on a surface. The liquid is assumed to be infinitely long in the axial, or *z*, direction and is assumed to have a cylindrical cross-section. All changes in the energy of the system under consideration are changes in surface energy, which are directly proportional to changes in surface area. Thus, by comparing the surface area of the original truncated cylinder to the surface area of the perturbed cylinder, including any interactions between the liquid and the surface it is resting upon, one can determine the stability of the original system. It should be noted that the geometry we are investigating is not, per se, the exact geometry that always occurs in these systems, but it is representative of that which occurs.

The most convenient coordinate system for performing these calculations is cylindrical coordinates as shown in Figure 4.7. As can be seen, the origin is located centrally on the surface upon which the liquid rests. The variable w represents the half width of the cylinder and θ represents the contact angle of the liquid. The variables r, ϕ, and z are standard cylindrical coordinates.

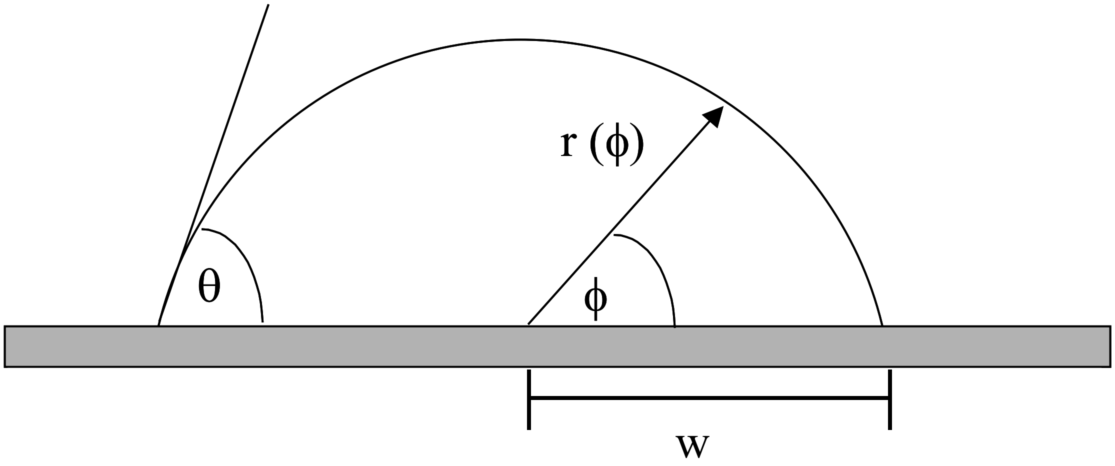

Figure 4.7. The geometry of the cross section of the line of fluid.

The top surface of the truncated cylinder is given by

$$r(\phi) = \frac{w}{\sin\theta}\left[\left(1-\cos^2\theta\cos^2\phi\right)^{\frac{1}{2}} - \sin\phi\cos\theta\right]. \tag{4.1}$$

Given this coordinate system, one can compute the surface area of this shape by applying:

$$S = \iint_{Surface} \left|\mathbf{r}_\phi \times \mathbf{r}_z\right| \cdot d\phi \cdot dz\ , \tag{4.2}$$

where $\mathbf{r}_\phi$ and $\mathbf{r}_z$ are tangent vectors given by

$$\mathbf{r}_\phi = \left\langle \frac{\partial x}{\partial \phi} \ , \ \frac{\partial y}{\partial \phi} \ , \ \frac{\partial z}{\partial \phi} \right\rangle \tag{4.3}$$

$$\mathbf{r}_z = \left\langle \frac{\partial x}{\partial z} \ , \ \frac{\partial y}{\partial z} \ , \ \frac{\partial z}{\partial z} \right\rangle \tag{4.4}$$

and x, y and z equal $r \cos\phi$, $r \sin\phi$, and z, respectively.

As stated earlier, a fixed footprint model and a variable footprint model were examined. The fixed footprint model would apply to a TSI system that could swell but for which the swollen material would remain in the silylated region. The variable footprint model would govern a system in which the swollen cylinder was able to move into the surrounding region. It is possible that energetic interactions or degree of swelling could govern which model is applicable.

Case A: Fixed Footprint Analysis

In this case, the cylinder maintains a constant footprint; hence, the interactions with the substrate are the same for both the perturbed and unperturbed cases and therefore can be neglected. As a result, any changes in energy in this system will be proportional to the change in surface area of the disturbed cylindrical cap. Mathematically, one could impose this disturbance in any number of forms, but in this case, the disturbance was modeled as a sinusoidal disturbance to the contact angle,

$$\theta(z) = \theta_o\left(1 + A\sin\left(\frac{2\pi z}{L}\right)\right) \tag{4.5}$$

where A represents the amplitude and L represents the wavelength of the sinusoidal perturbation. For this disturbance, the total volume of a length L of the undisturbed cylinder must be conserved. To satisfy this constraint, θ_o was determined based on conservation of volume between the initial and final state. The volume of the perturbed cylinder can be easily calculated by integrating the cross sectional area of the cylinder along the z axis. Setting this integral equal to the volume of the perturbed integral yields

$$Lw^2\left(\frac{\theta_i}{\sin^2\theta_i} - \frac{1}{\tan\theta_i}\right) = V = \int_0^L w^2\left(\frac{\theta(z)}{\sin^2\theta(z)} - \frac{1}{\tan\theta(z)}\right)dz\,, \tag{4.6}$$

where θ_i is the undisturbed contact angle. Equation 4.6 was solved numerically to give the correct value for θ_o. Once this parameter was determined, the surface area was computed by combining equations 4.1 through 4.4 and numerically integrating. This process was repeated for a range of L/w ratios and at a variety of contact angles. The amplitude of the disturbance was fixed at one percent. The normalized energy change due to the perturbation is plotted against *L/w* for various contact angles in Figure 4.8.

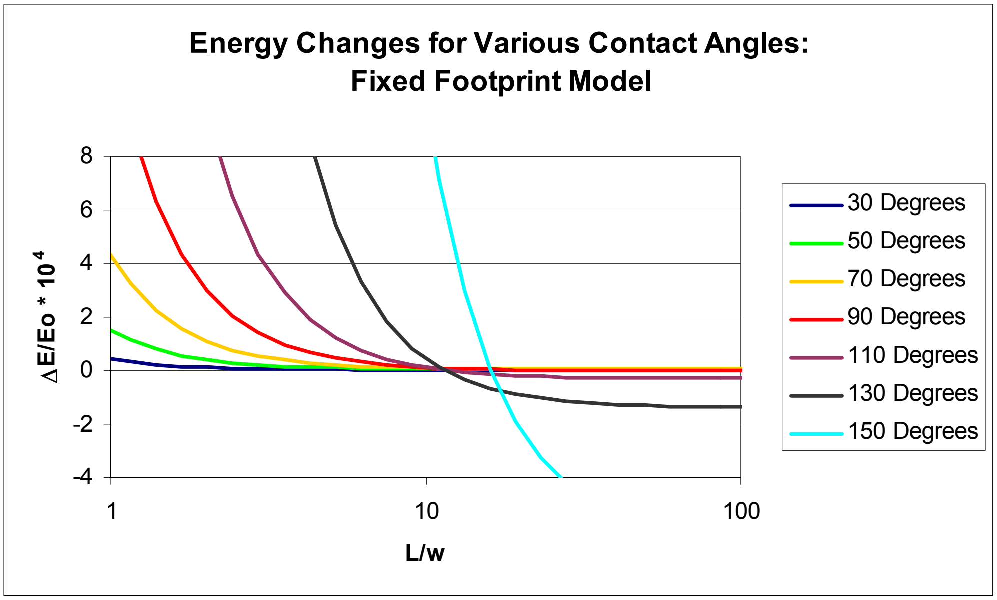

Figure 4.8. Surface area change as a function of normalized disturbance wavelength for several initial contact angles

The point on the graph where the change in energy equals zero corresponds to the normalized wavelength at the onset of instability. This wavelength is plotted against contact angle in Figure 4.9. The system is unstable to disturbance wavelengths longer than the critical wavelength.

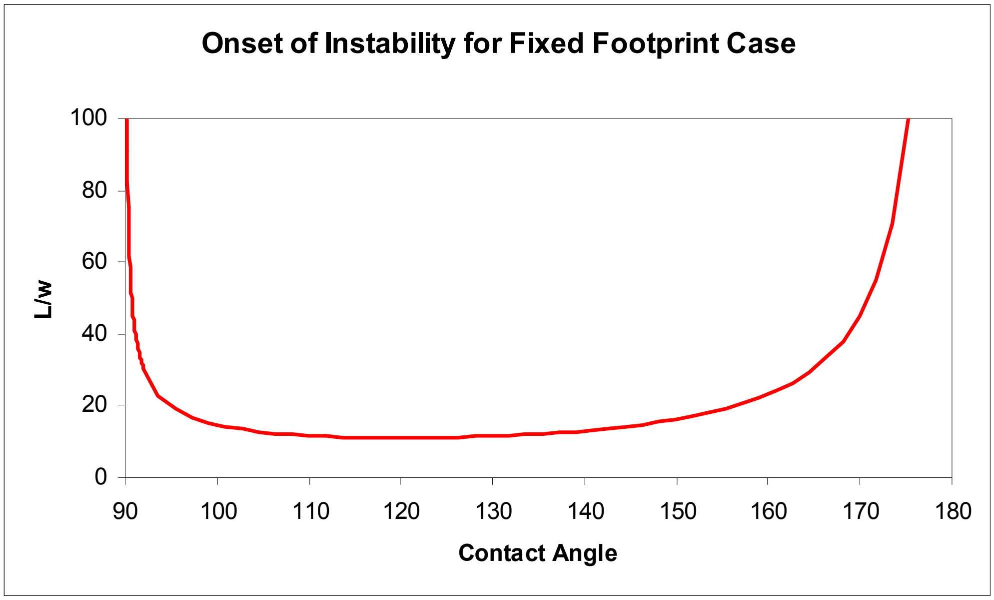

Figure 4.9. Critical Wavelength for the onset of instability for contact angle disturbances

Case B: Variable Footprint Analysis

In the case of the variable footprint disturbance, a similar perturbation,

$$w = w_o\left(1 + A\sin\left(\frac{2\pi z}{L}\right)\right), \tag{4.7}$$

was applied to the cylinder. The parameter w_o was determined by conservation of volume as before. In this case, an additional complexity arises from the interactions of the cylinder with the surface. The change in energy for this case can be described as

$$\frac{\Delta E}{\gamma} = \Delta S + \left(2w_i L - 2w_o L\right)\cos\theta\,, \tag{4.8}$$

where ΔE is the change in energy of the system, γ is the surface energy of the liquid, w_i is the initial drop half width, w_o is the average perturbed drop half width, and ΔS is the change in surface area of the cylinder. This equation is derived from an energy balance around the system and a force balance at the three phase boundary. From Equation 4.8, it is clear that the energy change is proportional to the change in surface area plus a small correction factor. As above, this energy change is plotted as a function of L/w and contact angle in Figure 4.10.

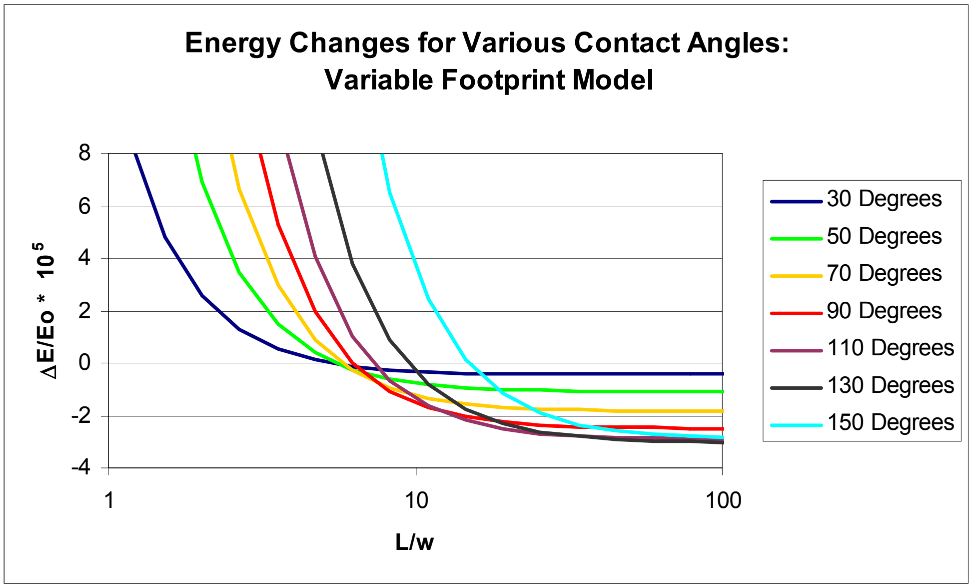

Figure 4.10. Surface area change as a function of normalized disturbance wavelength for several contact angles

The point on the graph where the change in energy equals zero corresponds to the normalized wavelength of the onset of instability. This wavelength is plotted against contact angle in Figure 4.11.

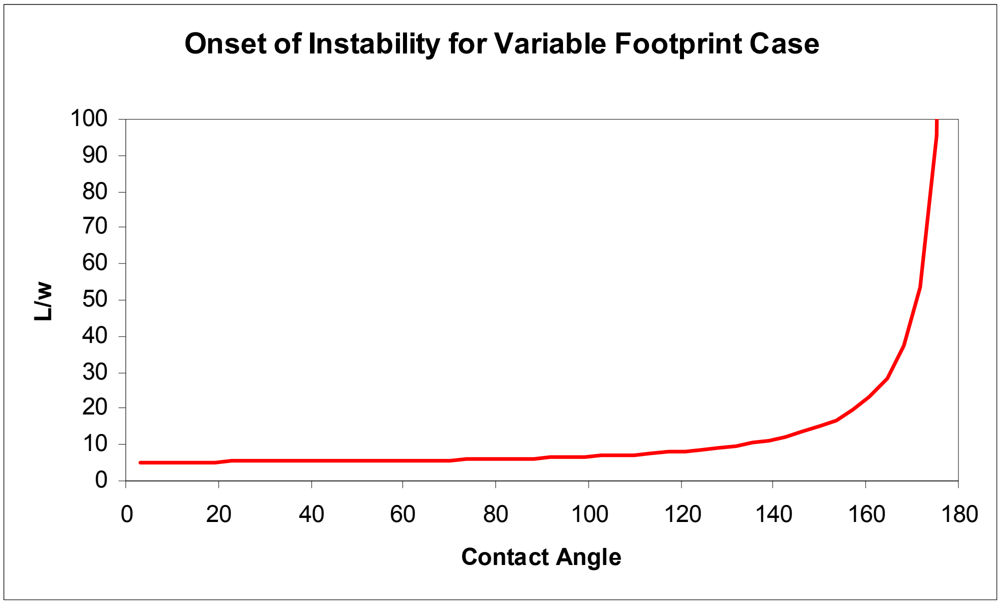

Figure 4.11. Critical wavelength for the onset of instability for variable footprint disturbances

DISCUSSION

Simulation indicates that a truncated cylinder with a fixed footprint is stable for contact angles less than 90° and unstable for contact angles greater than 90°. For the variable footprint case, it was found that the system was unstable for all contact angles. Figures 4.9 and 4.11 above show the critical wavelength at which the system becomes unstable. The system is unstable to wavelengths longer than the critical wavelength.

Rayleigh demonstrated that a cylinder is unstable at a critical wavelength to radius ratio of 2π. This case is similar to the situation in which we have a *w* perturbation to our half cylinder at a contact angle of 90^o. The numerical simulation also predicts the onset of instability to occur at an *L/w* ratio of 2π.

These results are similar to those of the literature[2, 11], but with two significant differences. First, our model found that the fixed angle case is unstable over all contact angles, contrary to the results of Grinfeld, which found the instability only in contact angles lower than 90^o. However, it is possible that the truncated cylinder is stable to his particular disturbance, but unstable to those presented here, rendering the system unstable overall. We find a similar contradiction in the fixed width case as the contact angle approaches 180^o. Our critical wavelength increases towards infinity as the contact angle approaches 180^o, whereas the solutions in the other two papers come to finite values. This is likely due to the nature of the angular disturbance at high contact angles, and likely indicates that the truncated cylinder is unstable to their short-wavelength disturbances, but not ours, and is thus unstable overall.

Combining the results of our model with those of the literature, we can compare experiments to theory. Experiments show that as the truncated cylinders increase in swelling they begin to degrade. This phenomenon occurs at a contact angle of less than 90°. A comparison of the wavelength of the disturbance versus what is predicted by the constant contact angle model shows good agreement. The dominant periodic structures have wavelengths on the order of 6-10 times the half-width of the trench, which is of the correct size (at 70°, *L* ~7 w). This indicates that as the polymer swells it is modeled well with the fixed footprint model. At low degrees of swelling, no instability was observed. This result indicated that at low degrees of swelling perhaps the constant contact angle model is more appropriate. This result can be explained qualitatively by comparing the surface energy of the silylated polymer to the unsilylated material around it. Clearly these two energies are quite different. As a result, the silylated polymer will tend not to swell into the surrounding material; hence the constant footprint model is appropriate. As increased swelling occurs, however, the cylindrical cap on the polymer will grow larger and larger, approaching the contact angle of the liquid on its surroundings. Upon reaching this contact angle, the polymer footprint will begin to encroach into the surrounding material. At that point, the variable footprint model becomes applicable, and the system can begin to degrade by capillary instabilities.

CONCLUSIONS

These results indicate that in TSI systems, the polymer will swell to a certain degree, at which point the swollen polymer will wet the surrounding material. At that point the system will become unstable. As a result, low frequency LER could be reduced or eliminated by choosing high glass transition temperature materials and by reducing the amount of swelling.

References:

(1) Fel, L. G.; Zimmels, Y. *Los Alamos National Laboratory, Preprint Archive, Condensed Matter* **2002**, 1-25, arXiv:cond-mat/0211045.

(2) Gratzke, U.; Kapadia, P. D.; Dowden, J.; Kroos, J.; Simon, G. *Journal of Physics D: Applied Physics* **1992**, *25*, 1640-1647.

(3) Kong, Y.-P.; Tay, F. E. H.; Xu, Y. *Proceedings of SPIE-The International Society for Optical Engineering* **2000**, *4230*, 89-99.

(4) Tanaka, S.; Umbach, C. C.; Blakely, J. *Surface Science* **1997**, *372*, L298-L300.

(5) Somervell, M. H.; Fryer, D. S.; Osborn, B.; Patterson, K.; Byers, J.; Willson, C. G. *Journal of Vacuum Science & Technology, B: Microelectronics and Nanometer Structures* **2000**, *18*, 2551-2559.

(6) Jamieson, A. T.; Somervell, M. H.; Tran, H. V.; Hung, R. J.-P.; MacDonald, S. A.; Willson, C. G. *Proceedings of SPIE-The International Society for Optical Engineering* **2001**, *4345*, 406-416.

(7) Stewart, M. D.; Schmid, G. M.; Goldfarb, D. L.; Angelopoulos, M.; Willson, C. G. *Proceedings of SPIE-The International Society for Optical Engineering* **2003**, *5039*, 415-422.

(8) Peters, R. D.; Amblard, G. R.; Lee, J.-J.; Guenther, T. *Proceedings of SPIE-The International Society for Optical Engineering* **2003**, *5039*, 393-403.

(9) Cobb, J. L.; Rauf, S.; Thean, A.; Dakshina-Murthy, S.; Stephens, T.; Parker, C.; Peters, R. D.; Rao, V. *Proceedings of SPIE-The International Society for Optical Engineering* **2003**, *5039*, 376-383.

(10) Chan, V. Z. H.; Thomas, E. L.; Frommer, J.; Sampson, D.; Campbell, R.; Miller, D.; Hawker, C.; Lee, V.; Miller, R. D. *Chemistry of Materials* **1998**, *10*, 3895-3901.

(11) Grinfeld, M. *Mechanics Research Communications* **1994**, *21*, 613-616.

Chapter 5: Synthesis and Evaluation of Polymers for Top Surface Imaging Applications.

BACKGROUND:

It has been proposed that line edge roughness (LER) in top surface imaging systems is the result of silylated polymer mobility. Materials that are capable of flow may rearrange themselves to attain the minimum energy state through processes such as phase separation at the feature edge or Rayleigh instability. The argument is that the decreased mobility of a polymer with a high Tg could kinetically hinder these phenomena. This was consistent with the fact that the single TSI system that printed smoothly, PFAS, had significantly higher Tg than it's processing conditions[1]. Work discussed in chapter 2 with the high-Tg polymer, poly(NBHFA) indicated that a high glass transition temperature might not be sufficient to improve LER. In collaboration with chemists from the Willson group, a number of polymers were synthesized and evaluated to test if LER can be improved by raising the Tg.

Polymers were synthesized and purified in a chemistry laboratory. Typical parameters such as molecular weight (GPC), purity (IR, NMR), Tg (DSC) and blocking fraction were measured. Once the polymer was prepared and its material properties evaluated, it was dissolved in a casting solvent with additives such as photo-acid-generators and bases, and properties are evaluated in the chemical engineering laboratories. These properties include: deprotection kinetics, silylation kinetics and ability to coat out typical solvents. Only once a polymer behaves well in all of these respects was it brought to International Sematech for imaging experiments.

Approximately twenty polymers were synthesized and evaluated. None of them printed smoothly. Overall, increased glass transitions improved low-frequency roughness resulting from Rayleigh instabilities, but high frequency roughness did not change dramatically. The purpose of this chapter is to document these results. The first section presents a summary of all the polymers that were synthesized and tested, as well as their mechanism of failure. The rationale for the creation of each polymer is discussed as well. The second section of the chapter contains a step-by-step analysis of a maleimide polymer. This analysis is representative of the normal evaluation process for all polymers.

SECTION A: POLYMERS EXAMINED IN THIS THESIS.

Introduction to TSI polymers:

There are a number of requirements that must be met for a polymer to form an image using a chemically amplified, negative tone TSI process. First, the polymer must contain a group that reacts irreversibly and readily with a silylation agent. Typically, an alcohol with a pKa of ~12 is used to react with an amino-silane. Second, the reactive group must be completely protected prior to exposure in order to limit reactions with the silylation agent in unexposed areas. Third, in order for the silylated polymer to be etch resistant, it must contain ~12wt% Si after the silylation reaction. This requirement is typically challenging to meet. The fourth requirement, common to all photoresists, is that the polymer must be etch resistant in plasma processes for silicon and silicon dioxide removal. The plasma conditions used in silicon and silicon dioxide etches are typically harsh. Mixtures of chlorine and bromine are used for the former, while fluorine is used for the latter. This requirement is met by incorporating functional groups that are highly unsaturated (such as rings and double bonds). In general terms, this etch resistance is obtained by using aromatic rings, such as benzene, and alicyclic rings like adamantane and norbornane. In traditional, wet-developed resist systems, the former was used at 248nm, and the latter at 193nm, where each is transparent. The polymers synthesized and examined in these experiments can be broken into two groups: phenolic polymers and fluorinated norbornene alcohol polymers.

Phenolics

As a functional group, phenol is nearly perfect for TSI. It is easy to protect the phenolic hydroxyl group with either a tBOC protecting group, or an acetal protecting group. The group has a pKa of ~12 and is reactive with aminosilanes. The silicon content of a phenol group reacted with DMADMS is more than 18wt%, leaving significant design latitude for the rest of the structure. Typically, it is incorporated into a polymer using hydroxystyrene (hydroxystyrene is not a stable compound, and polymerizations are usually performed with acetoxystyrene or tBOC styrene). The benzene ring is very etch resistant.

The silylation of polyhydroxystyrene (PHS) introduces significant challenges. While the Tg of PHS is high (~150C), upon silylation with DMADMS, it drops to an unacceptable level of <65C. This low Tg causes many of the problems discussed in chapter 4. The low Tg of the silylated polymer is likely the caused by the lack of significant steric hindrance on the backbone, coupled with the low intermolecular interaction associated with the silicon-containing group. The long bond-length of the Si-O bond adds flexibility to the structure, making the Tg lower. Although there is some design latitude for the polymer, without use of a dual silicon silylation agent, such as DMADMDS, it doesn't have high enough silicon content to allow the major structural changes that are needed to greatly modify the Tg. The second portion of this chapter one of very few methods devised to alter the Tg significantly of a PHS system.

Fluorinated Norbornenes

The norbornene functional group is etch resistant, and the fluorinated species tend to be somewhat transparent in the UV, giving them utility for single layer applications at 157nm. Many of the monomers and polymers studied here are by-products of the 157nm program in the Willson chemistry group. There are numerous synthetic routes to polymerize norbornenes, such as metal catalyzed addition polymerizations, ring-opening methathesis polymerizations, and copolymerizations with a number of co-monomers including sulfur dioxide, carbon monoxide, and acrylates. Norbornene monomers are readily available from Diels Alder reactions of cyclopentadiene with alkenes. The pKa of hexafluroalcohol is nearly identical to that of phenol, making it readily silylated. The norbornene group is highly etch resistant to silicon and silicon dioxide etch processes. Additionally, norbornene homopolymers are extremely hindered along their backbone, and have very high Tg's as a result.

From a design standpoint, the fluorinated norbornene systems suffer from a couple of flaws. First, fluorine has a fairly substantial molecular weight of 19 g /mole. Therefore, the electronegative hexafluoro group that is required to shift the pKa of the acid to the same level as phenol contains as much mass as a benzene ring. A single alcohol group must then react with a two-silicon silylation agent in order to achieve an adequate level of silicon in the final structure; one silicon is needed to compensate for the etch resistant norbornene, the other to for the hexafluro group. Dual silicon silylation agents either suffer from low reaction rates, as is the case with pentamethyldisilyldimethylamine, or are extremely difficult to obtain, even in small quantities, as is the case with DMDSDMA. Fluorinated monomers are often challenging to synthesize, and often difficult to polymerize. There is the added worry that the evolved fluorine from the etch step could interact unfavorably with the silicon dioxide hardmask that is the basis of the TSI transfer etch step. These challenges make the fluorinated norbornenes difficult to work with, but the availability of the monomers and polymers from the 157nm single layer program made them appealing nonetheless.

All polymers synthesized in the course of these experiments are shown in figures 5.1 & 5.2. Mark Somervell investigated a number of polymers as well, of which only PFAS printed smoothly. These polymers are shown in Figure 5.3. Table 5.1 summarizes the behavior of the polymers synthesized and tested in both Mark's and my work.

Figure 5.1: Phenolic TSI polymers that were synthesized and evaluated.

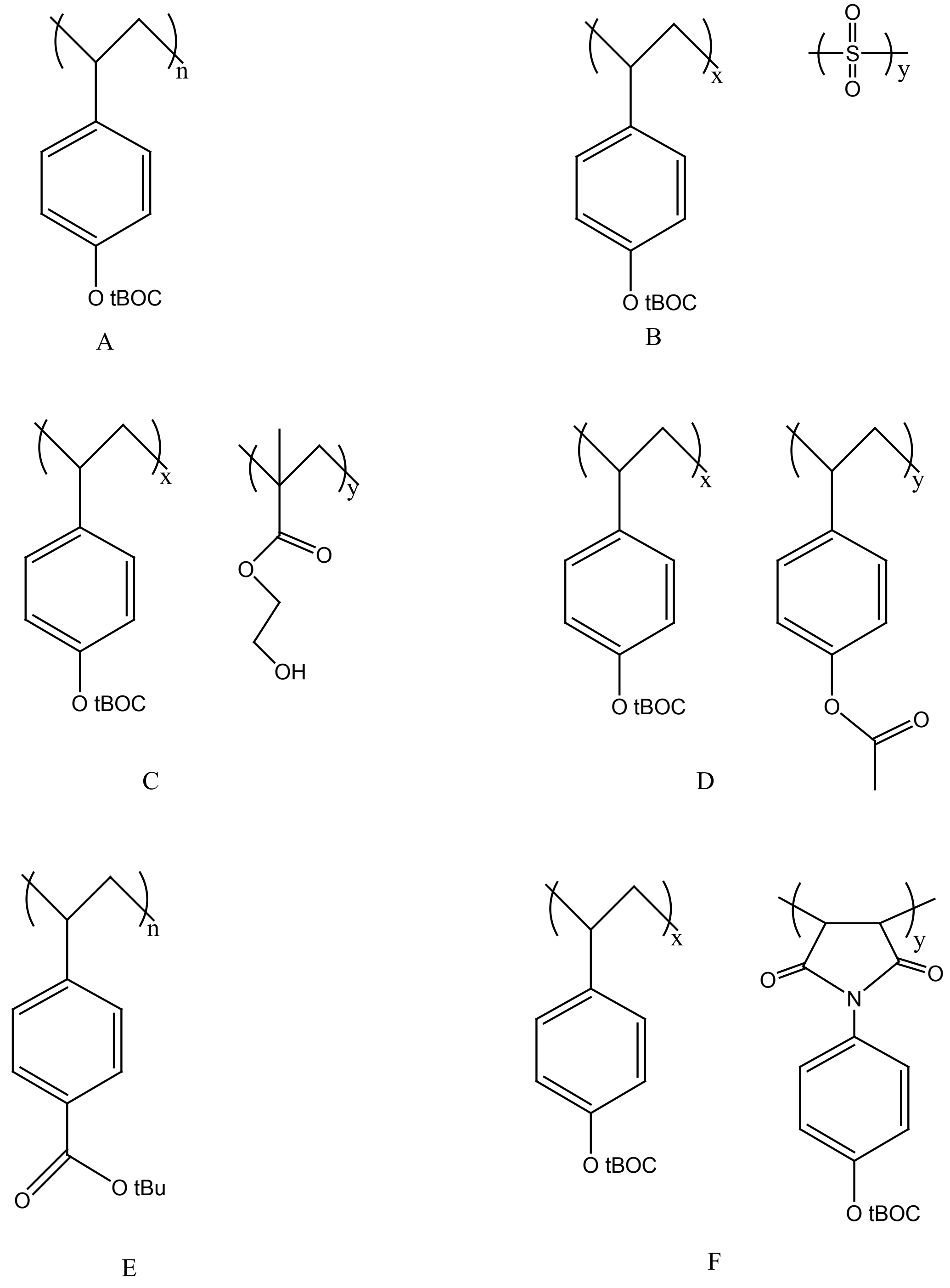

Figure 5.2: Fluorinated Norbornene polymers that were synthesized and evaluated.

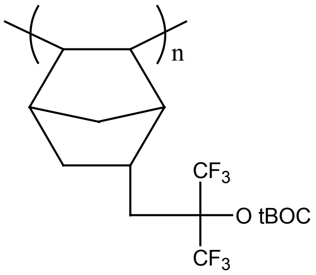

G

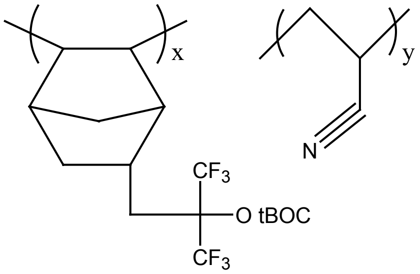

H

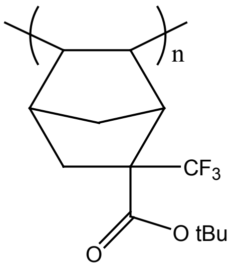

I

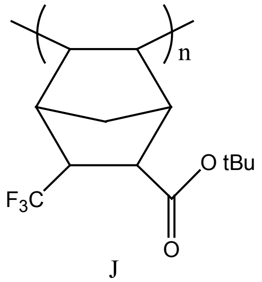

J

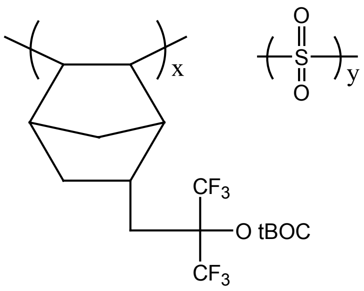

K

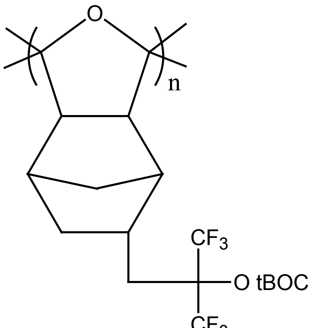

L

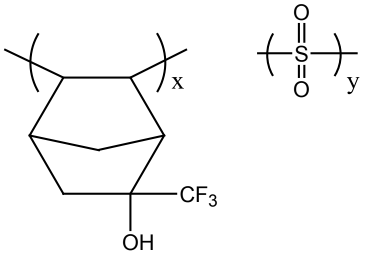

M

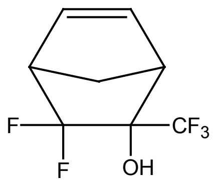

N

Figure 5.3: Mark Somervell's polymer that were synthesized and evaluated.

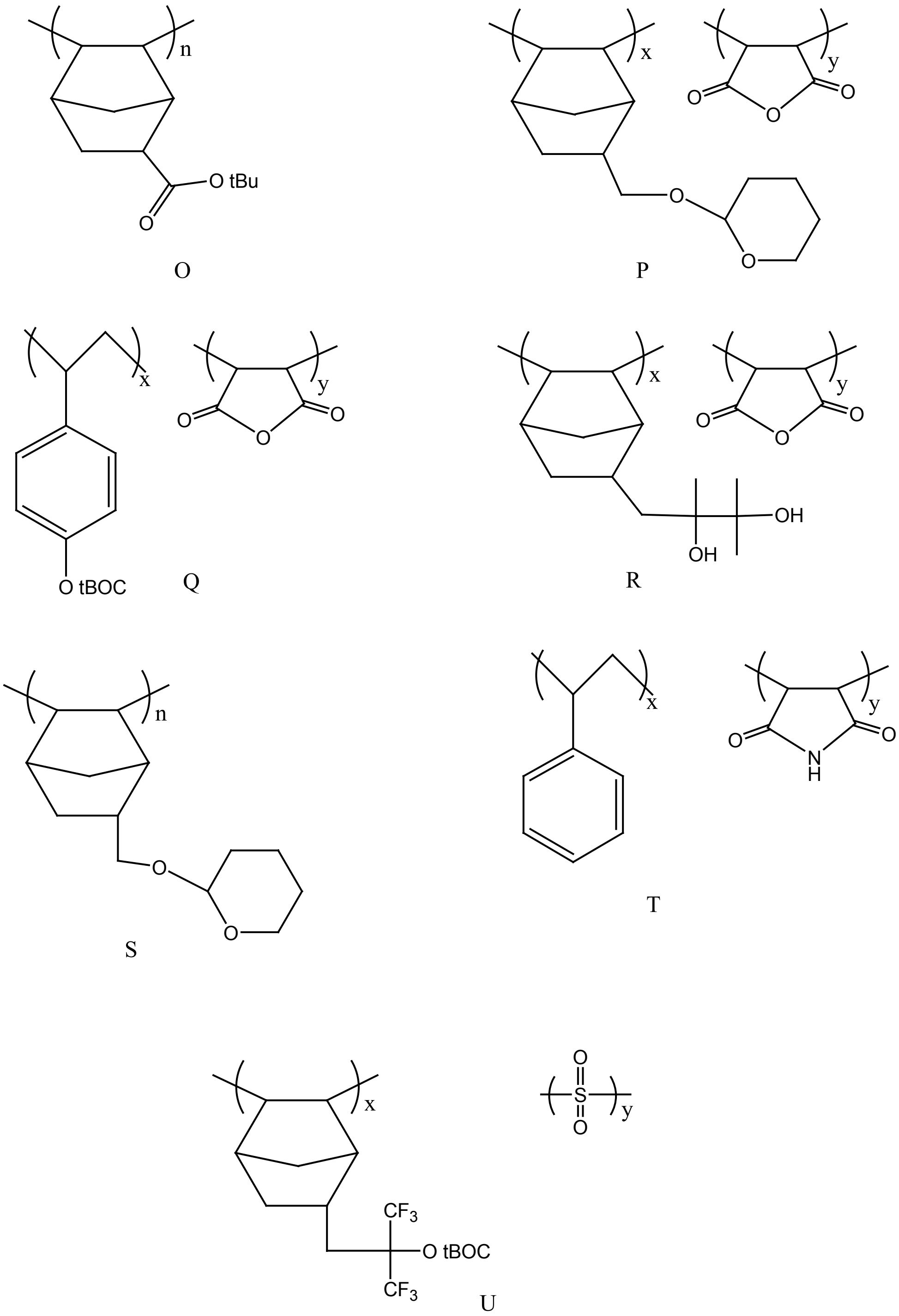

O

P

Q

R

S

T

U

Table 5.1: Summary of polymer development & evaluation

Polymer	Spin Coat?	Deprotects?	Silylates?	Images?	Smooth?	Synthesized by:
A	Yes	Yes	Yes	Yes	No	Numerous
B	Yes	Yes	Yes*	Yes	No	Lucent
C	Yes	Yes	Yes	Yes	No	Jamieson
D	Yes	Yes	Yes	Yes	No	Somervell
E	Yes	Yes	No	No	No	Pinnow
F	Yes	Yes	Yes	Yes	No	Hogan
G	Yes	Yes	Yes	Yes	No	Yamada
H	Yes	No	No	No	No	Jamieson
I	Yes	Yes	No	No	No	Pinnow
J	Yes	No	No	No	No	Pinnow
K	Yes	Yes	Yes	Yes	Yes	Somervell
L	Yes	Yes	Yes	Yes	No	Chiba
M	Yes	NA	No	No	No	Hung
N	No	No	No	No	No	Not made
O	Yes	Yes	No*	No	No	Somervell
P	Yes	Yes	No	No	No	Somervell
Q	Yes	Yes	Yes*	No	No	Somervell
R	Yes	Yes	No	No	No	Somervell
S	No	No	No	No	No	Somervell
T	Yes	NA	No	No	No	Somervell

Motivations for each polymer:

A. This is the standard TSI polymer. It has high silicon content and a low Tg in the silylated state. The majority of the thesis is based on investigations of this polymer.

B. The only polymer that has printed smoothly contained sulfur dioxide. Sulfur dioxide as an added gas to etch processes has been shown to improve LER. This polymer was used to verify that sulfur dioxide was not the cause of the smooth imaging of PFAS; it wasn't.

C. HEMA has been shown to crosslink under acidic conditions. If phase separation were occurring, it was possible that crosslinking the system could inhibit it. Different incorporation ratios were investigated, namely 5:95, 15:85, and 25:75 (HEMA: tBOC styrene, respectively). Evidence existed that the system was crosslinking, but the imaging was not improved.

D. Poly(acetoxystyrene) has a higher Tg than the silyated form of PHS. These copolymers were synthesized due to their higher Tg's in the silylated state (by Fox's rule, the Tg should raise appreciably). Different copolymer ratios were investigated, namely 96:4, 20:80, 40:60, 60:40, and 80:20, (acetoxystyrene: tBOC styrene, respectively). By using the dual silicon silylation DMDSDMA, images were created with acetoxystyrene incorporation ratios up to 60:40. Nonetheless, the images printed roughly.

E. It has been reported by Somervell[2] that aliphatic carboxylic acids silylate, but subsequently hydrolyze. This polymer was an attempt to duplicate this result with an easily accessible polymer. It hydrolyzed, as expected.

F. This polymer is discussed in depth in the second section of this chapter. It has an extremely high Tg, and thus it was hoped to print well. It too printed roughly.

G. This polymer has an extremely high Tg as well (>200C). It requires the use of DMDSDMA and was discussed more thoroughly in chapter 2. Overall it prints roughly.

H. This polymer was an attempt to duplicate the polarity of PFAS, without the problems associated with the sulfone group. Unfortunately, the basic nature of the cyano group caused the acid-catalyzed deprotection to be inhibited.

I. This polymer, along with J, is contains a t-butyl ester that was synthesized in the hopes of avoiding the hydrolysis problems discussed with E. Ideally, the non-polar nature of the fluorine groups would decrease water absorption into the film, thereby decreasing the hydrolysis rate to a reasonable level. Unfortunately this did not work in either polymer.

J. See I.

K. This was the single polymer that printed smoothly. Originally synthesized by Ito[3] , and investigated for TSI by Somervell[1], this polymer and its results have been repeated and studied thoroughly. It is the only polymer that prints well.

L. This spiroketal polymer has an extremely low molecular weight, probably degrading it's imaging quality significantly. This polymer was made in an attempt to duplicate the polarity of PFAS, without the problems associated with the sulfone groups. It printed very roughly.

M. This trifluoroalcohol polymer appeared great on paper. It was extremely close in structure to PFAS, but with a significantly lower monomer molecular weight. If it were to have silylated, we thought the polymer might have been a higher Tg alternative to A. Unfortunately, it did not silylate.

N. This monomer had great potential as well. The pKa should have been very comparable to that of the hexaflouroalcohol, but the monomer repeat unit was much smaller. However, a reasonable synthetic route for polymerization was not developed for this monomer.

O-T. See M. Somervell's thesis

SECTION B: TYPICAL POLYMER EVALUATION.

This section presents a typical procedure for synthesizing and evaluating a polymer. As is shown here, it involves an enormous amount of work. Much of this work was performed in collaboration with chemists. In this particular case, a very talented undergraduate student, Zach Hogan, synthesized the polymer with assistance from Matt Pinnow, a chemist in the group. Zach Hogan and I performed the evaluation in chemical engineering.

To test the hypothesis that line edge roughness could be improved by raising the glass transition of the polymeric species, poly[*p*-(*tert*-butoxycarbonyloxy] styrene-alt-N-(*p*-(*tert*-butoxycarbonyloxy) phenyl) maleimide) (tBOCMAST) was synthesized. The acronym MAST refers to the maleimide styrene base polymer with an alcohol functionality. High and a low molecular weight samples (545,000 and 4000) were synthesized and tested for imaging performance.

Polymers described in the literature having structures similar to the silylated form of *t*-BOCMAST have T_g values above 220 ^{o}C[4]. It was hoped that using *t*-BOCMAST would decrease or eliminate LER due to its high T_g. Along with a high T_g value, *t*-BOCMAST's synthetic route was fairly straightforward. An added benefit of the MAST system is that the low molecular weight of the repeat unit allows for the use of dimethylaminodimethylsilane for silylation. This is in contrast to previous work with high Tg systems that contain the hexafluoroalcohol moiety that necessitated the use of the dangerous and rare compound dimethylaminodimethyldisilane. Additionally, the absence of fluorine in this system alleviates worries about the evolution of fluorine during the etch step affecting the silicon dioxide etch mask. It was hoped that these factors, high T_g, ease of synthesis, use of commercial SA, and absence of fluorine would open up a new group of high T_g photoresist polymers for further study in TSI systems

Experimental

Synthesis of High MW MAST

Synthesis of poly(*p*-(*tert*-butoxycarbonyloxy) styrene-alt-N-(*p*-(*tert*-butoxycarbonyloxy) phenyl) maleimide) (*t*-BOCMAST) was based on previous work by Turner, et al[5]. The synthesis steps are shown in Figure 5.4.

Figure 5.4. Synthesis of *t*-BOCMAST

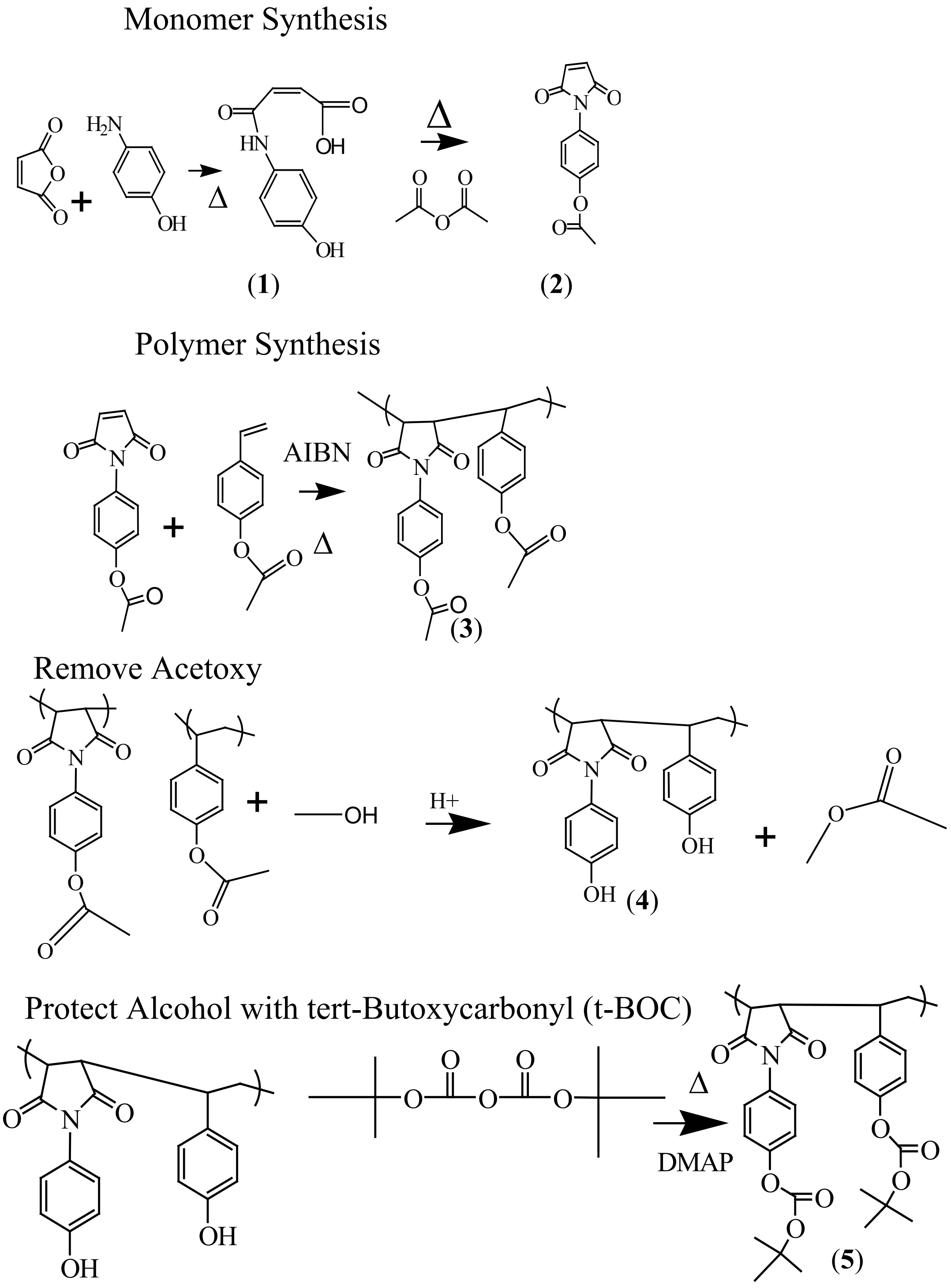

N-(p-Hydroxyphenyl)maleamic Acid (1)

To a round bottom flask (500 ml) was added maleic anhydride (50 g, .51 mol), 4-aminophenol (56 g, .59 mol) and 200 ml of toluene. The reaction mixture was heated at reflux for 15 min. The solution was filtered warm via vacuum filtration and washed with toluene to yield **1** as a lime-green solid. MP 225-228 ^{o}C. ^{1}H NMR (DMSO-d_6, 300 MHz), 6.277 (d, $\sigma = 12.3$, 1H), 6.4505 (d, $\sigma = 12.3$, 1H), 6.7165 (d, $\sigma = 9$, 2H), 7.406 (d, $\sigma = 9$, 2H), 9.338 (s, 1H), 10.355 (s, 1H). Mass spect (CI, CH_4) 108 (m + 1).

N-(p-Acetoxyphenyl)maleimide (2)

To a round bottom flask (500 ml) was added a solution of **1** (20 g, .10 mol) and sodium acetate (4 g, .05 mol) in acetic anhydride (200 ml). The solution was heated at 85 ^{o}C for 4 hours under a nitrogen atmosphere then cooled to room temperature and finally poured into an Erlenmeyer flask (4 L) filled with ice. This mixture was stirred overnight and the resulting tan precipitate was collected via vacuum filtration and dried to yield **2.** MP 163-165 ^{o}C (lit 158-160 ^{o}C[5]. ^{1}H NMR ($CDCl_{3,}$ 300 MHz, ppm), 2.291 (s, 3H, -CH_3), 6.835 (s, 2H, maleimide), 7.177 (d, $\sigma = 4.5$, 2H, aromatic), 7.358 (d, $\sigma = 4.5$, 2H, aromatic). Mass Spect (CI, CH_4) 232 (m +1)

*Poly(***p***-(acetoxystyrene-alt-N-(***p***-(acetoxyphenyl)maleimide) (3)*

To a round bottom flask (500 ml) was added **2** (6 g, .026 mol), acetoxystyrene (4.5 g, .027 mol), azobisisobutyronitrile (.12 g) and acetone (50 ml). The solution was put through a freeze-pump-thaw cycle (x3). The reaction solution was heated at 60 °C for 24 hours under a nitrogen atmosphere. The reaction was cooled and additional acetone (50 ml) was added before precipitation into methanol (2 L). The precipitant was vacuum filtered and dried in a vacuum oven to yield **3** as a white solid.

*Poly(*p*-(hydroxystyrene)-alt-N-(*p*-hydroxyphenyl)maleimide) (4)*

To a round bottom flask (500 ml) was added **3**, p-toluene sulfonic acid (1.8 g, .01 mol), acetone (345 ml) and methanol (45 ml). The mixture was heated and acetone and methyl acetate were distilled off until the total volume was 200 ml. The resulting polymer was precipitated into hexane (2 L). The precipitant was vacuum filtered and then dried in a vacuum oven to yield **4** (6.6 g, .02 mol, 82% yield) as a brown solid: ^{1}H NMR (DMSO-d_6 300 MHz, ppm), 1-4, 6-7, 9.1-9.8. IR (KBr, cm^-1) 3429 (OH), 1767, 1700 (C=O maleimide ring).

*Poly (*p*-(*tert*-butoxycarbonyloxy) styrene-alt-N-(*p*-(*tert*-butoxycarbonyloxy) phenyl) maleimide) (*t*-BOCMAST) (5)*

To a round bottom flask (500 ml) was added **4** (3.3 g, .0095 mol), di-tert-butyldicarbonate (3.3 g, .015 mol), N-N dimethylaminopyridine (50 mg), and dry THF (200 ml). This solution was heated at reflux for 12 hours. The mixture was then cooled and precipitated into hexane (2 L). The precipitate was vacuum filtered and dried in a vacuum oven to yield **5** as a white solid (3.56 g, .007 mol, 74% yield): GPC analysis in THF gave Mw = 544,700, Mn = 123,600, MWD =

4.41 ^{1}H NMR (DMSO-d_6 300 MHz, ppm), 1.2-1.8, 6.4-7.4. IR (KBr, cm^-1)1762 (t-BOC C=O) 1716 (maleimide C=O). TGA, loss onset at 180 ^oC, 37.2 % (theoretical loss = 39.7%).

Synthesis of Low Molecular Weight MAST

N-(p-Hydroxyphenyl)maleamic Acid (**2**) was synthesized as described earlier and recrystallized in acetone. The product had identical analytical results to earlier samples.

The effect of chain transfer agents in polymerizations has been well explored in polymer chemistry. These agents operate by transferring the radical from a propagating chain to a monomer. This serves to reduce the molecular weight of the polymer and to control the polydispersity.

Low molecular weight poly(*p*-(acetoxystyrene-alt-N-(*p*-(acetoxyphenyl)maleimide) (3)

To a 250 ml round bottom flask was added 3 g of **2**, 2.25 g Acetoxystyrene, .24 g AIBN, 50 ml of acetone and 1.4 g dodecanethiol. This mixture was heated at 60 ^oC under nitrogen for 20 hours. The polymer was precipitated in 2 L of methanol, filtered and then dried for 24 hours at 50 ^oC in a vacuum oven to yield 3.76 g of **3** (yield=71.6%.) GPC revealed a much lower molecular weight: GPC analysis in THF gave Mw=3837, Mn=3004, MWD=1.277. H-NMR and IR results match previous results.

*Low Molecular Weight Poly(*p*-(hydroxystyrene)-alt-N-(*p*-hydroxyphenyl)maleimide) (4)*

Deprotection followed the previous method with the exception that the precipitation was carried out in water rather than hexane.

*Low Molecular Weight Poly(*p*-(*tert*-butoxycarbonyloxy) styrene-alt-N-(*p*-(*tert*-butoxycarbonyloxy) phenyl) maleimide) (*t*-BOCMAST) (5)*

Followed previous method described earlier. H-NMR and IR are the same as higher molecular weight polymer. GPC analysis in THF gave Mw=4000, Mn=300, MWD=1.3.

Evaluation of Photochemistry and Silylation

The high molecular weight *t*-BOCMAST was formulated into a photoresist and evaluated. The formulation consisted of 1 gram of high molecular weight polymer in 15 grams of PGMEA and 4% weight triphenyl sulfonium nonaflate (TPS-Nf.). This formulation was filtered using a 0.2 μM PTFE filter and spin-coated at 3000 rpm for 30 seconds. Films underwent a post-application bake (PAB) for 2 minutes at 90^{o}C and were then flood exposed for 60 seconds under an unfiltered mercury arc lamp. The post-exposure bake (PEB) was 2 minutes at 90^{o}C. Infrared spectra of both exposed and unexposed films were measured. Silylation was then carried out using DMADMS at 90^{o}C and 66 torr in the *in-situ* ellipsometry chamber (discussed in chapter 6). The infrared spectrum was taken of the silylated polymer. FTIR spectra revealing deprotection and silylation are shown in Figure 5.5.

Figure 5.5. IR of *t*-BOC MAST Deprotection and Silylation

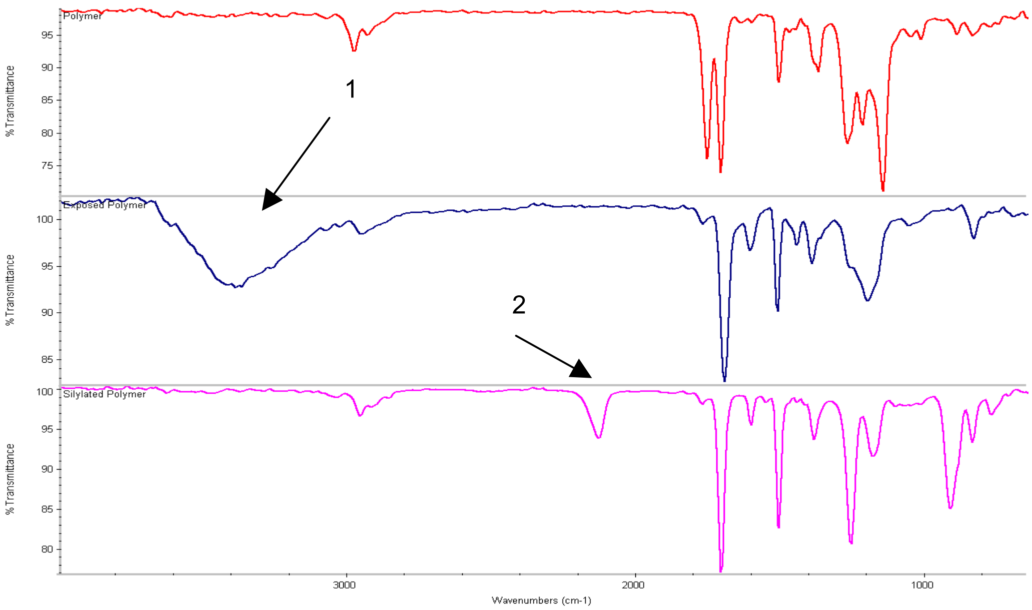

1. Deprotection of co-polymer upon exposure. Monitor IR at 3100-3400 cm^(-1)

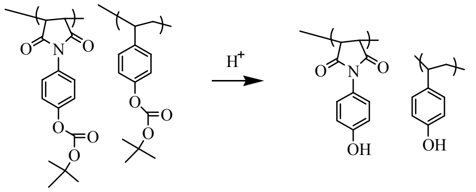

2. Silylation with dimethylaminodimethylsilane (DMADMS). Monitor IR at 2250 cm^(-1)

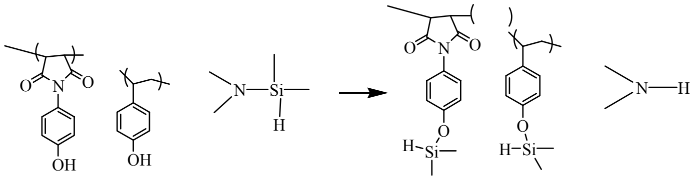

Ellipsometry of MAST Polymer

A film formulated identically to those used in the IR studies, but cast at 2000 rpm, with a PAB at 120°C and a PEB at 120°C was silylated with DMADMS. Simultaneously the reaction was monitored by ellipsometry (as discussed in chapter 6). Figure 5.6 shows a two-layer fit to the reaction data. As the unsilylated polymer layer is consumed, the silylated polymer layer grows in a linear relationship. The figure also reveals satisfactory reaction speed.

Figure 5.6. Two Layer Fit of Silylation Ellipsometry Data

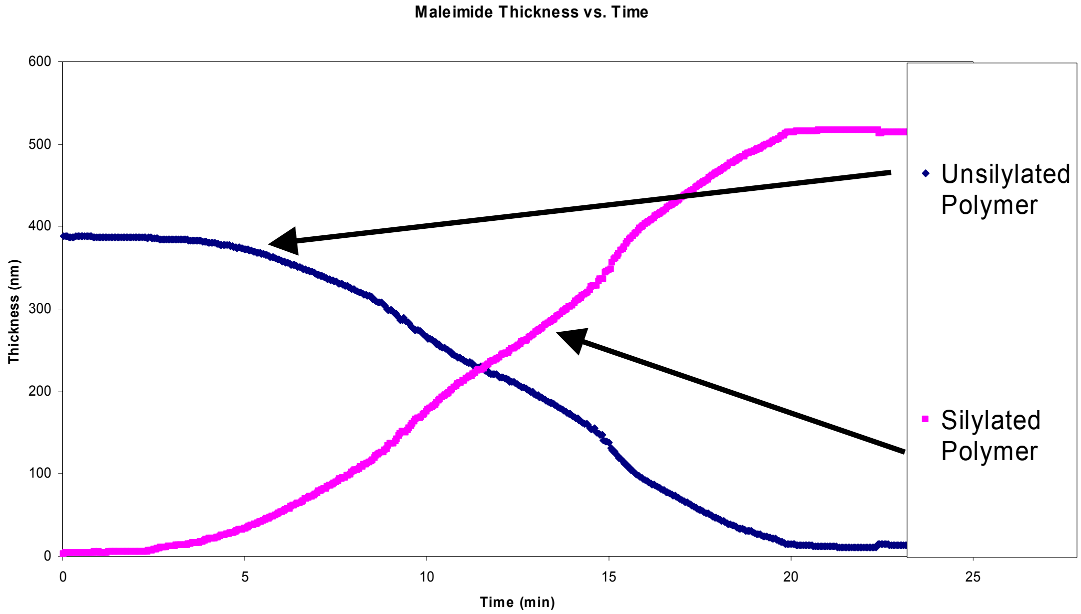

T_g Measurement by Ellipsometry

The T_g of a polymer thin film can be measured by a number of techniques by probing a number of variables, such as mechanical properties, or index of refraction. Due to the possibility of hydrolytic degradation of the silylated films, the most convenient method to determine the Tg is to monitor the thermal expansion coefficient using real-time ellipsometry *in-vacuo*. A graph of thickness versus temperature reveals the T_g as a change in the thermal expansion coefficient.

The Tg of a spun-cast polymer film will vary based on the molecular weight, polydispersity, rate of heating or cooling, solvents in the film and others factors. More broadly, the major factor that determines a polymer's Tg is intermolecular forces. The stronger a polymer's interactions within a chain or between chains, the higher the T_g. For example, polystyrene (PS) has a T_g of 94-97 ^oC while PHOST, with its hydrogen bonding, has a T_g of 140-160 ^oC[6]. Another major factor in a polymer's T_g is the amount of rigidity of the polymers backbone. A polymer backbone that allows rotation of monomer units around the backbone will have a much lower T_g than a polymer that does not allow rotation.

A LabView program was written to ramp the temperature of the heating stage at a constant rate while recording the temperature at controlled time intervals. While the temperature ramp was occurring, ellipsometric data was collected using the chamber discussed in chapter 6. Following completion of the run, the ellipsometric data was used to find thickness as a function of time. These files were analyzed to yield a thickness versus temperature graph from which a change in the thermal expansion coefficient can be discerned. The accuracy of the technique was analyzed by measuring the Tg of thin-film Polystyrene and comparing with literature. Additionally, in order to validate the technique's application to silylated systems, the Tg of silylated poly(hydroxystyrene) was measured.

T_g Sample Preparation and Analysis

Polyhydroxystyrene was obtained from Triquest Chemical Company. Polystyrene (PS) samples were acquired from Aldrich at a weight average molecular weight of 270,000. Low molecular weight tBOC-MAST was used, requiring deprotection. This was accomplished by preparing a solution of polymer in PGMEA with a ratio of 1:30. To this solution triphenylsulfonium nonaflate (TPS-nf), a photoacid generator, was added to an amount of 4% of total weight of dissolved compounds. Following coating, these samples were post-application baked (PAB) at 90^{o}C for 2 minutes. The films were then exposed with 40 mJ/cm^2 at 248 nm and post-exposure baked (PEB) at 120^{o}C to cause deprotection.

All films were prepared on 2-inch wafers and annealed at 150^{o}C in a vacuum oven for at least 12 hours. Following annealing, the samples were cooled under vacuum to room temperature to avoid hydrolysis of the silylated samples. Before collecting data on the annealed silylated samples, a resilylation step was performed to ensure a fully silylated films. This was performed at 80^{o}C and 16 torr DMSDMA and monitored by ellipsometry. Resilylation changed the thickness by several percent. After this step, the sample was cooled for the T_g run. The data acquired during the first ramp typically did not have a sharp glass transition, and as such, the second and subsequent ramps were used for reported values.

Results

Thickness versus temperature data was collected on polystyrene (PS), silylated PHOST, and silylated MAST. Figure 5.7 shows an example of how the graphs were used to determine T_g.

Figure 5.7. T_g Determination of Silylated PHOST at Vacuum

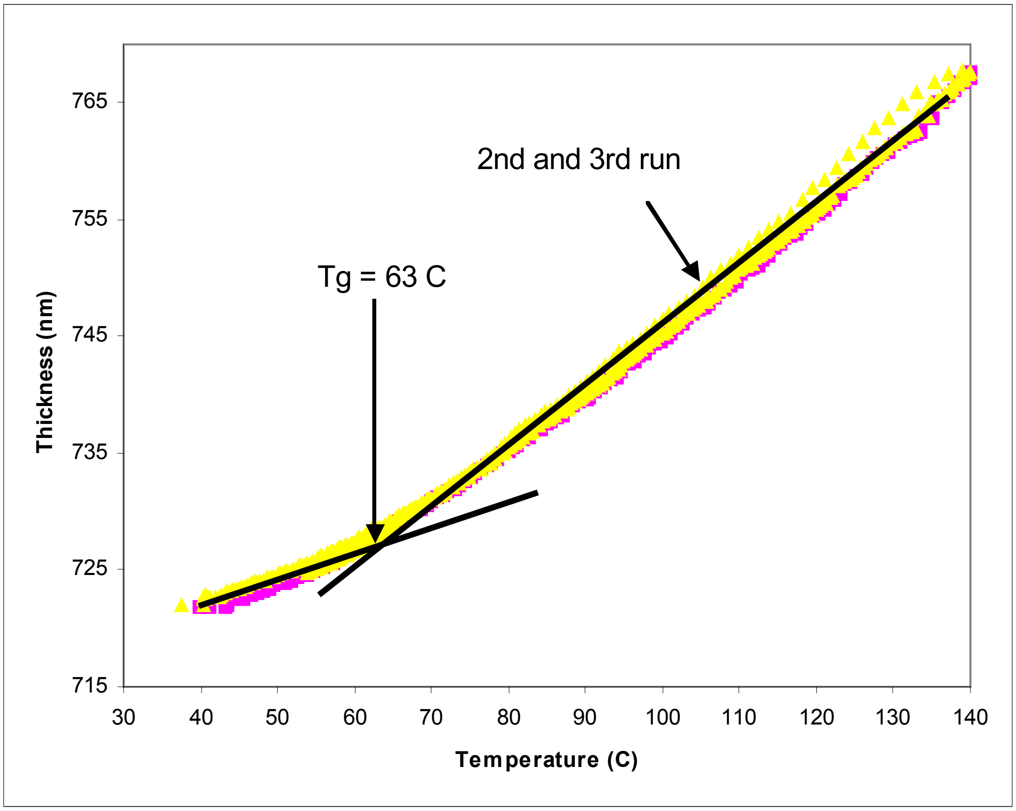

Two different linear thermal expansion regimes can be seen in this graph. The intersection of these two lines is the T_g. Values of the T_g were collected and are listed in Table 5.2. The two numbers represent the 2^{nd} and 3^{rd} temperature ramp cycle.

Table 5.2: T_g of Polymers

Polymer	**Tg**
Polystyrene	100 ^{o}C, 99 ^{o}C ref. 94-97 ^{o}C[6]
Silylated PHOST	63 ^{o}C, 65 ^{o}C ref 65 ^{o}C[2]
MAST	No clear value below 150 ^{o}C
Silylated MAST	No clear value below 150 ^{o}C

Discussion of Tg measurements

The measurement of T_g again shows the usefulness of *in-situ* ellipsometry to characterize thin-films. The T_g of silylated PHOST shows how close the polymer is to its T_g even at the lowest processing temperatures. Given this fact it is clear that PHOST is going above its T_g during silylation. In contrast, the MAST has a much higher T_g in its silylated form. This polymer was synthesized to test the effect of high T_g on the imaging process in the hopes a high T_g would reduce the high frequency LER. The T_g is clearly high enough to claim that the polymeric species should not have significant mobility at the operating temperatures used.

Exposure and Processing for High Molecular Weight Polymer

The high molecular weight MAST polymer was then processed at International SEMATECH. The film underwent a PAB for 1 min at 100°C. The PEB was 1 min at 90 °C. Silylation was performed on a Genesis Microstar 250 using 50torr of DMADMDS at 90 °C for 10 min. 248 nm imaging was performed at International SEMATECH on a SVGL Microscan III using a binary mask (NA = 0.6, σ = 0.6). Etch was performed at International SEMATECH using a Lam 9400 SE operated with a top and bottom power of 260W and 75W respectively. The pressure was 2.5mTorr of Oxygen at a flowrate of 60sccm and a chuck temperature of -25 °C. Following etch, the two wafers were examined using a Joel Tilt SEM. Figure 5.8 shows an example of the features obtained.

Figure 5.8. SEM of Features Formed with High Molecular Weight MAST

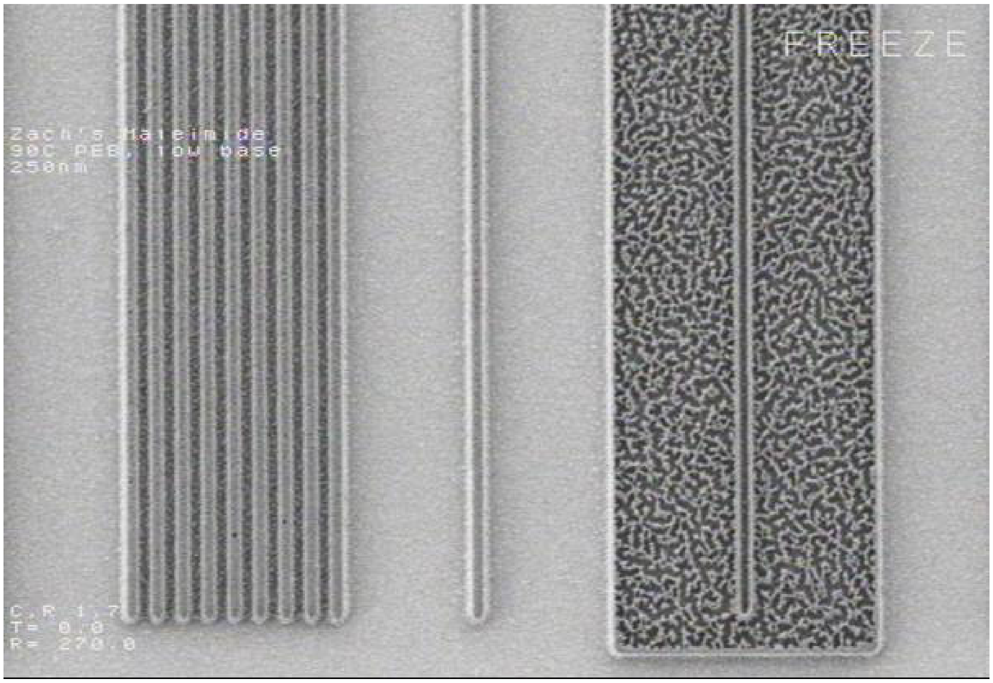

The feature on the right side of the micrograph is an isolated trench in an area of silylated polymer. This large area of silylated polymer appears to lack etch resistance. Note that the moderate exposure dose at the large feature edge, and throughout the nested lines possessed adequate etch resistance. A possible cause for the low etch resistance at high exposure doses is diffusional limitations in this high molecular weight polymer. The high molecular weight could introduce silylation agent diffusion limitations (other commercial TSI schemes have used photo-induced crosslinking to create silylation agent diffusivity-based contrast). The higher exposure dose could induce acid-catalyzed crosslinking. A lower molecular weight version would test this hypothesis. As such, the low Mw version of MAST was created, and silylated with the smaller DMADMS

SEM Images and Results for Low MW MAST

Following initial imaging with the high molecular weight MAST, it was decided to test a lower molecular weight version. This polymer was synthesized as described previously. Imaging was carried out at Sematech using the same procedure as before. The silylation agent used was DMADMS rather than DMADMDS. This silylating agent barely generates the requisite 12wt% Si needed for etch resistance. Figure 5.9 shows an SEM image of features produced with this polymer.

Figure 5.9. SEM of Features Formed with Low Molecular Weight MAST

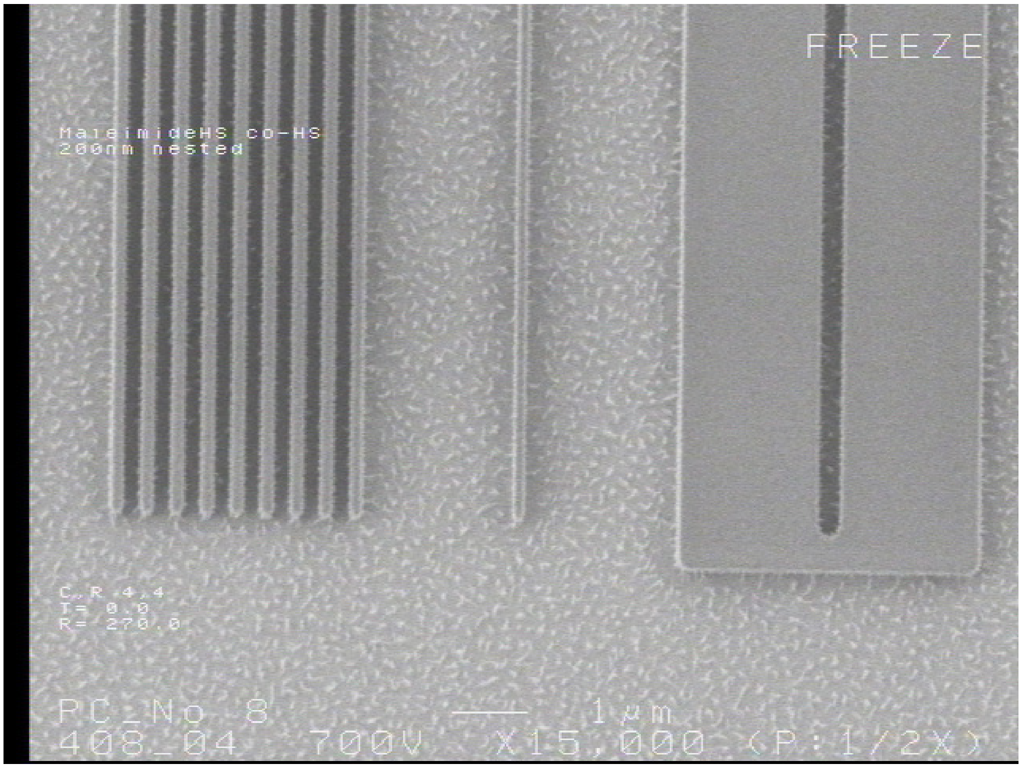

This is the same feature as the micrograph of the high molecular weight MAST. The features were etch resistance due to the increased silicon incorporation in the low molecular weight sample with DMADMS. In the high molecular weight sample silylated with DMADMDS, the diffusion of the SA into the film was likely limited and resulted in etching of exposed areas. The features shown in figure 5.9 still show evidence of some background silylation. The background silylation is due to the difficulty of protecting all hydroxyl groups with *t*-BOC on a polymer chain, or sorption. Unfortunately, the features still exhibit evidence of high frequency LER, but at least show no evidence of low frequency LER.

DISCUSSION AND CONCLUSION ON MALEIMIDE POLYMER

MAST demonstrates that a maleimide containing family of co-polymers appears to improve low frequency LER in TSI. The high frequency LER present in the MAST SEMs shows that this phenomenon is not tied to T_g, but related to some other property of the TSI process.

References:

(1) Somervell, M. H.; Fryer, D. S.; Osborn, B.; Patterson, K.; Byers, J.; Willson, C. G. *Journal of Vacuum Science & Technology, B: Microelectronics and Nanometer Structures* **2000**, *18*, 2551-2559.

(2) Somervell, M. Doctoral, University of Texas, Austin, 2000.

(3) Ito, H. S., N.; Sato, R.;Nakayama, T.;Ueda, M *Micro- and Nanopatterning Polymers*; ACS, 1998.

(4) Chiang, W. Y.; Lu, J. Y. *Journal of Polymer Science, Part A: Polymer Chemistry* **1991**, *29*, 399-410.

(5) Turner, S. R.; Arcus, R. A.; Houle, C. G.; Schleigh, W. R. *Polymer Engineering and Science* **1986**, *26*, 1096-1100.

(6) Ngai, P. In *Physical Properties of Polymers Handbook*; American Institute of Physics, 1996, pp 139.

Chapter 6: The Kinetics of poly(hydroxystyrene) Silylation by Dimethylaminodimethylsilane.

ABSTRACT:

Real-time variable angle spectroscopic ellipsometry was used to monitor the reaction of dimethylaminodimethylsilane gas with spin cast films of poly (hydroxystyrene) at temperatures between 70-120^{o}C, and at pressures up to 50 Torr. The reaction progresses by a reaction limited, front propagated mechanism in which the gas phase agent is highly soluble in the silylated film, but much less so in the unreacted film. Ellipsometry was capable of differentiating between the two layers, and the reaction was monitored by measuring their thicknesses. The extent of reaction as measured ellipsometrically was compared with that monitored by Fourier transform infrared spectroscopy and decoration etch techniques, and showed good agreement. The rate of silylation has a linear response to silylation agent pressure, indicating first order dependence on the silylation agent concentration in the reacted film. The overall reaction rate has an Arrhenius dependence on temperature, and the activation energy for the reaction can be extracted by taking into account the temperature dependence of Henry's law coefficients.

BACKGROUND:

Top surface imaging is a lithographic technique that involves the selective photochemical creation of reactive alcohol sites at the surface of a film[1, 2]. These alcohol groups serve as reactive sites for selective incorporation of silicon into the film. The incorporated silicon, in turn provides etch resistance in an oxygen plasma. The anisotropic oxygen etch process dry develops the film to create features in the areas where alcohols were generated. The reaction of the alcohol with silicon containing compounds is called a silylation reaction, and is typically performed with gas phase treatments. The reaction studied in this experiment is shown in Fig. 6.1. In its most common form, the gas phase reaction is undertaken by heating the <1μm spun cast polymer on a silicon wafer to between 70°C and 120 °C in a rough vacuum (<0.1 Torr), and introducing a silylation agent at a pressure of between 20 and 100 Torr. The reaction in the thin film is typically completed in less than 5 minutes.

Figure 6.1: The gas phase silylation of poly (hydroxystyrene) with dimethylaminodimethylsilane.

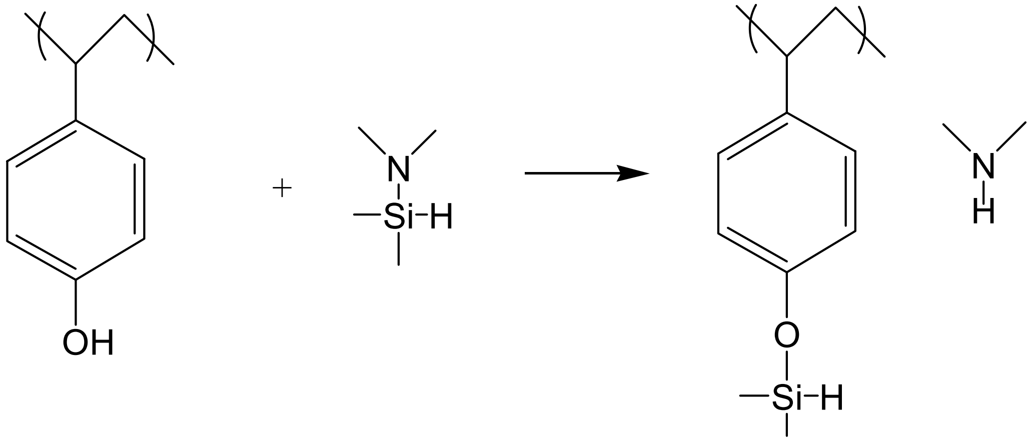

Although research has been performed to gain an understanding of the reaction limitations, most analyses neglect the effects of silylating agent solubility in the polymer film[3-11]. Additionally, with a few exceptions[6, 8], nearly all investigations have been performed in a batch manner with reaction steps followed by monitoring, leading to somewhat imprecise data.

Recent developments in real-time ellipsometery present the opportunity for careful measurement of both film index and thickness as a function of time. For a review of ellipsometry, the reader is referred to papers by Woolham et al[12-15]. Ellipsometry is beginning to be used more frequently in the polymer field[16, 17]. This work describes the construction and implementation of a controlled atmosphere chamber that allows for the accurate monitoring of the silylation reaction. By monitoring the thickness gain associated with altering the pressure of silylation agent above a film, the amount of silylation agent that is absorbing into the film can be measured.

An understanding of the phenomena that dictate reaction time in these thin films is required for optimizing existing processes, as well as for the development of new polymers and silylation agents. A quantitative measure of silylation agent absorption in these systems is of particular interest. It is of great importance from a lithographic standpoint that the materials remain immobile, and hence the process must be performed below the glass transition temperature (Tg) of the polymeric photoresist resin. If significant absorption occurs, the Tg can drop due to plasticization effects.

It has been proposed that the silylation process is limited by a front propagated reaction mechanism in which the silylation agent is highly soluble in the reacted film, and relatively insoluble in the unreacted film[18]. In this model, the overall silylation rate is limited by the first order reaction kinetics at the interface between these two polymers. As such, the silylation process is closely tied to the solubility of the agent in the reacted film. Starting with first order reaction kinetics:

$$Rate = k\ C_{SA} C_{OH} \tag{6.1}$$

where C_{SA} is the concentration of silylation agent in the silylated polymer, and C_{OH} is the concentration of alcohol groups in the polymer, the overall reaction rate as a function temperature can be derived. Assuming a Henry's law dependence of silylation agent concentration in the silylated film, and a rate constant with an Arrhenius dependence on temperature, we find:

$$Rate = A \exp(-Ea/RT)\ k_H(T)\ P_{SA} C_{OH} \tag{6.2}$$

where A is the Arrhenius pre-exponential, Ea is the reaction activation energy, $k_H(T)$ is the Henry's law coefficient, and P_{SA} is the pressure of silylation agent. By using the ellipsometer to monitor the thickness of the film as a function of time at various temperatures and pressures information about the overall kinetics can be obtained. After the reaction is complete, the sorption amounts can be determined by varying the pressure of silylation agent, and monitoring thickness changes resulting from swelling and contraction of the polymer. By taking into account the Henry's law dependence on temperature, we are able to accurately calculate reaction activation energies.

In addition to direct measurement of Henry's law values, the Flory-Huggins relationship can be used to approximate sorption. The Flory-Huggins equation allows a convenient way to approximate Henry's Law coefficients based on the enthalpy of vaporization, and a measured χ parameter. To obtain the relationship in an appropriate form, the basic Flory-Huggins equation is used,

$$\mu_{F-H} = k_B T\left(\ln(1-\phi_p)+\phi_p+\chi\phi_p{}^2\right) \tag{6.3}$$

where $\mu_{F\text{-}H}$ is the chemical potential of the solvent-polymer mixture, ϕ_p is the solvent fraction in the polymer film, T is the temperature and χ is the interaction parameter. By equating this with the gas phase chemical potential of k_B T ln(P / P^{sat}), inserting the Clausius-Claperyon equation for P^{sat}, and rearranging, we find:

$$\ln\left(\frac{P}{P_b}\right)-\frac{\Delta H^{vap}}{R}\left(\frac{1}{T_b}-\frac{1}{T}\right)=\ln\left(1-\phi_p\right)+\phi_p+\chi\,\phi_p{}^2 \tag{6.4}$$

where ΔH^{vap} is the enthalpy of vaporization of the solvent, and T_b is the boiling point at a pressure P_b (typically atmospheric pressure). Due to the low levels of sorption, ϕ_p can be approximated to equal one in the last two terms, and rearrangement and insertion of $1-\phi_p = \phi_s$ gives:

$$\phi_S = \frac{P}{P_b} \exp\left(-\frac{\Delta H^{rap}}{R} \left(\frac{1}{T_b} - \frac{1}{T} \right) - 1 - \chi \right) \tag{6.5}$$

By including Scatchard-Hildebrand solubility theory for χ, one finds the following useful relationship:

$$\phi_S = \frac{1}{P_b} \exp\left(\frac{-\Delta H^{vap}}{RT_b} - 1 \right) \exp\left(\frac{\Delta H^{vap} - \nu_1 (\delta_1 - \delta_2)^2}{RT} \right) * P \tag{6.6}$$

where ν_1 is the solvent molar volume, and δ_1 and δ_2 are the solubility parameters for the solvent and the polymer respectively. This derivation of Henry's law shows that the Henry's law coefficient should scale with an Arrhenius type dependence on temperature if operating within the low sorption regime.

Experimental

Ellipsometry and Silylation Chamber

Experiments were monitored using a Woollam VASE M-2000, capable of measuring the parameters psi and delta (which with optical modeling allows calculation of film thickness and index) at a measurement rate of more than 10Hz. A custom silylation chamber was constructed out of a stainless steel block with optical windows for the ellipsometry beam to pass through. A schematic of the custom chamber is shown in Fig. 6.2. The ellipsometry beam passed through ConFlat fused silica windows purchased from Kurt J. Lesker Company. Heating was accurately controlled using a custom designed aluminum heating stage, controlled by LabView software. The stage has a temperature uniformity of ~1^{o}C. Chamber atmosphere was controlled using a pneumatic manifold mounted inside an oven, a schematic of which is shown in Fig. 6.3. The LabView software allows for simultaneous control of 7 temperature zones, as well as the 6 pneumatic valves. Typically, the stainless steel block is heated to a temperature ~20 ^{o}C less than the stage. This temperature is hot enough to avoid silylation agent condensation but cold enough to allow a reasonable opposing driving force necessary for control of the aluminum heating stage. It was verified experimentally that the stainless steel block temperature did not affect reaction rates or sorption values. The windows were typically heated to 20 ^{o}C higher than the sample to ensure no cold spots caused condensation on the optical paths.

Figure 6.2: Schematic diagram of controlled environment silylation chamber for use with Woolham M2000 Ellipsometer.

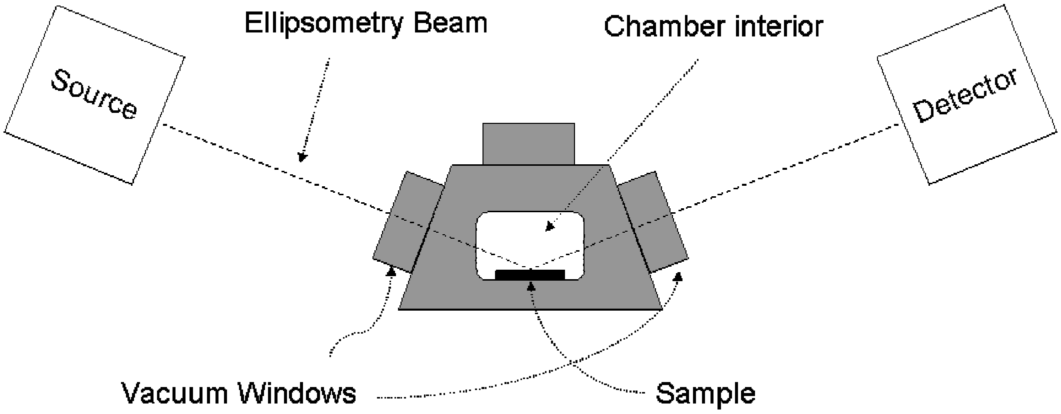

Figure 6.3: Schematic of the gas manifold for environmental control

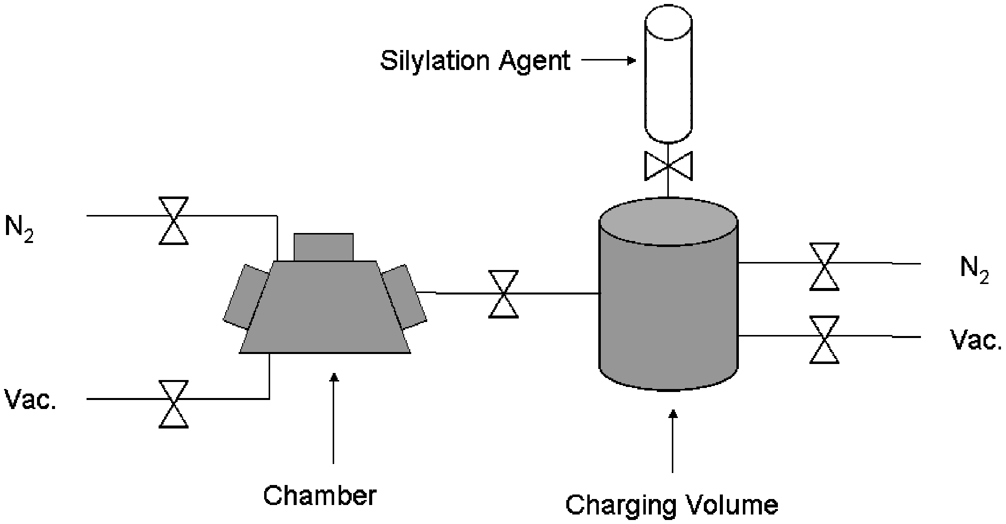

MATERIALS AND PROCESSING

Solutions of poly(hydroxystyrene) (obtained from ChemFirst in electronics grade form with Mw = 56,000) were dissolved in propyleneglycol methylether acetate (PGMEA), filtered through 0.2µm PTFE filters and spin cast on bare silicon wafers. The resulting samples were baked at 120 °C for 60s to remove residual casting solvent. The samples were placed in the controlled environment chamber described previously, and the pressure was dropped to <0.1torr, as measured by an Edwards Barocel 622 Capacitance Manometer. A concentrated gas of dimethylaminodimethylsilane (obtained from Silar laboratories in liquid form, and further distilled to increase purity) was then introduced at various pressures, and the reaction kinetics were measured. Typically, it was possible to accurately monitor the thickness of the bottom layer (unreacted) and top layer (reacted) thickness, due to the slight difference in index of refraction between the two polymer species and the assumed sharp front between them. A representative plot of the extent of reaction is shown in Fig. 6.4, and a plot of the two layer fit is shown in Fig. 6.5. The rate of reaction (in nm/s of PHS consumed) was measured ellipsometrically at a number of temperatures and pressures, and the resulting data is shown in Fig. 6.6. In order to validate the ellipsometric methodology, five samples were coated on double polished, aluminum backed wafers suitable for reflectance IR measurements. The reactions were truncated prior to completion at varying times. The integrated Si-H stretch frequency in the infrared at ~2100cm^{-1} was measured by a Nicolet Magna IR 550 with an external reflectance sensor (described previously by Burns et al[19] and compared to the ellipsometry based technique, also shown in Fig. 6.4. These samples were cleaved to reveal layer profiles using an oxygen decoration etch procedure with a Plasma Technology µ80 etcher. The cross-sectioning and decoration etch allows the reaction front to be seen on a SEM. The thickness of the two layers as measured by the ellipsometer and the SEM is shown in Fig. 6.5, along with two typical SEM pictures.

Figure 6.4: Silylation of poly(hydroxystyrene), as measured by ellipsometry & Infrared Spectroscopy.

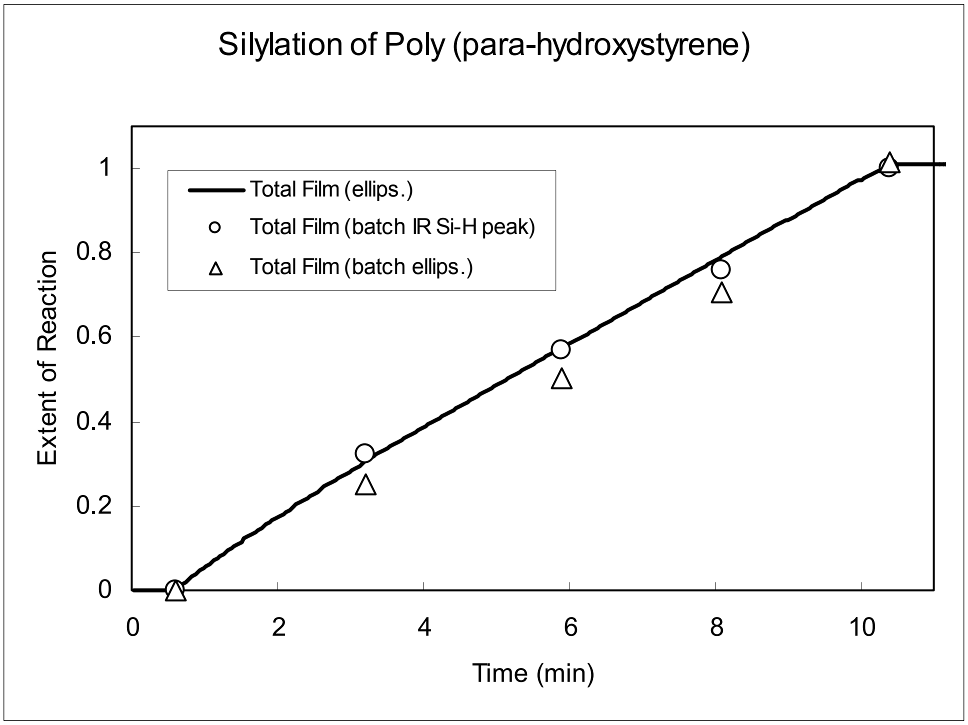

Figure 6.5: Silylation of poly(hydroxystyrene), (A) as measured by ellipsometry using a two-layer fit & by staining techniques & (B&C) typical SEMs of stained PHS, 3 minute & 8 minute silylations respectively.

A.

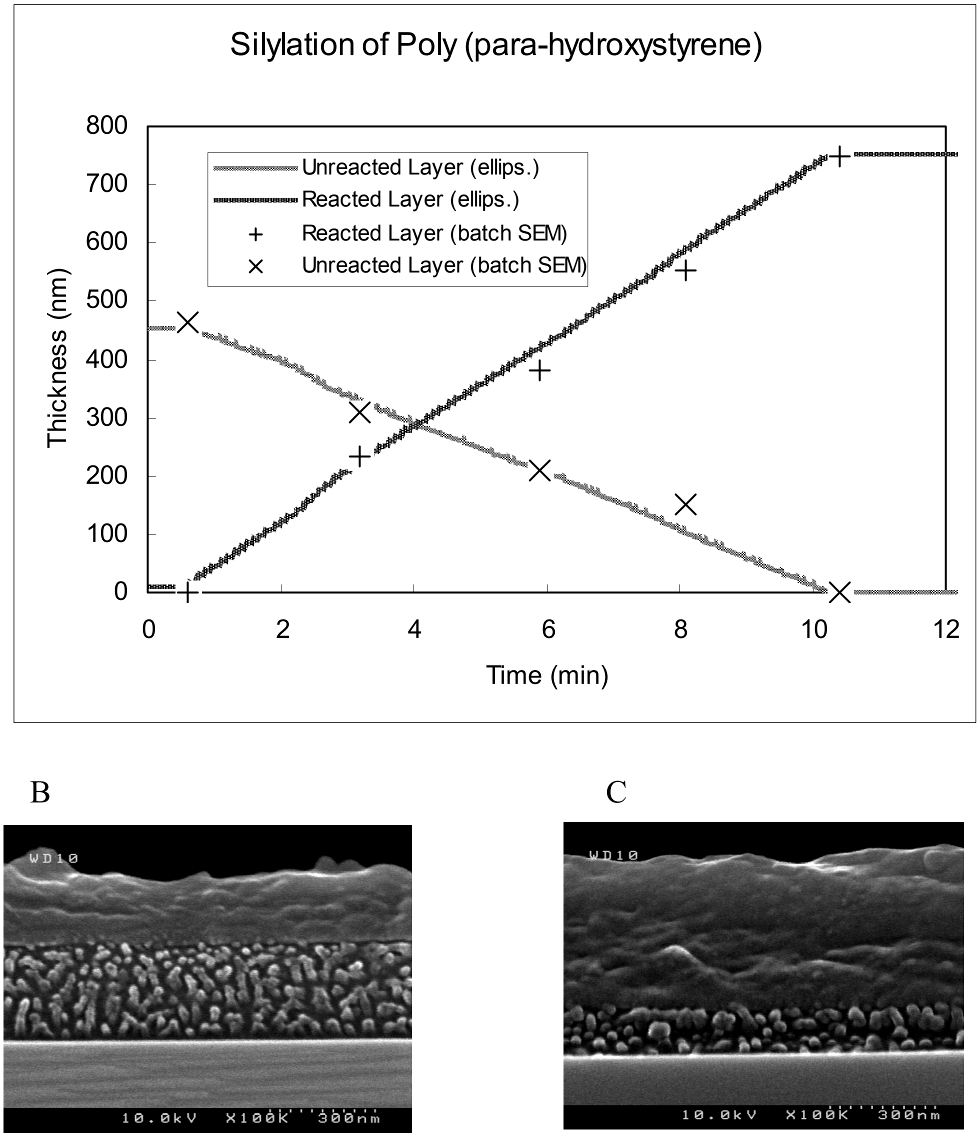

Figure 6.6: Reaction Rate as a function of temperature and pressure as measure ellipsometrically.

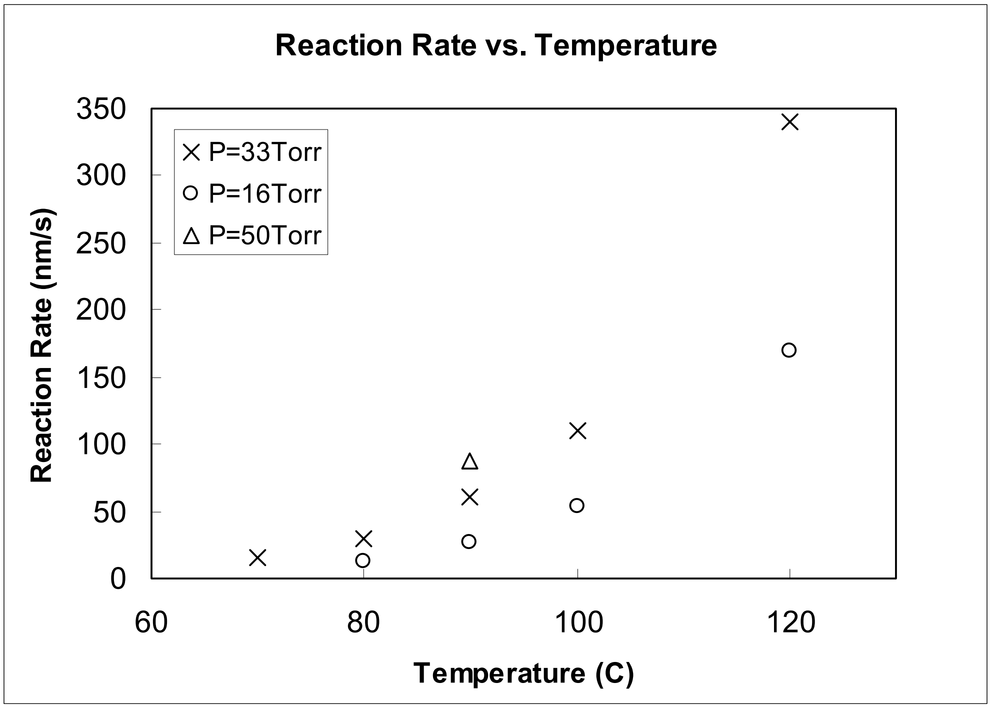

At each temperature, after reaction completion, Henry's law parameters were measured. To this end, the chamber pressure was dropped to <0.1 Torr then the film was exposed to alternating environments of gas and vacuum. By measuring the uniaxial expansion and contraction of the film during this process Henry's law coefficients can be approximated. This technique was compared to previous work by Wong[20] and Zimm[21] using the Toluene / Polystyrene system at 50 ^{o}C, and had very close agreement. A typical Henry's law curve, as measured by the ellipsometer, is shown in Fig. 6.7. The experimentally determined Henry's

Law coefficients measured at various temperatures are shown in Fig. 6.8 along with a curve based on the Flory-Huggins relationship (using physical properties and a value for $\nu_1(\delta_1-\delta_2)^2$ of 1.1 kJ/mol, as the single fitting parameter in the model). By measuring the vapor pressure as a function of temperature of dimethylaminodimethylsilane, the Enthalpy of vaporization could be extracted from the Clausius Claperyon equation, and was found to be 31.5 kJ/mol. This value is in close agreement with the Trouton's constant calculated value of 30 kJ/mol using the measured boiling point of 68°C.

Figure 6.7: Sorption and desorption curve of dimethylaminodimethylsilane in silylated poly (hydroxystyrene) at 60°C.

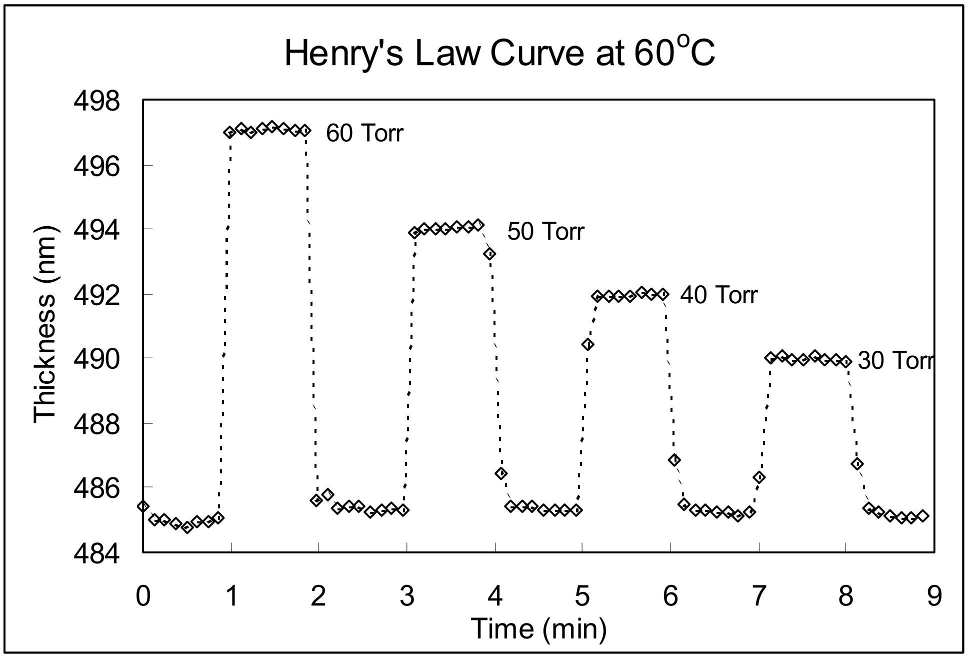

Figure 6.8: Henry's law coefficients as a function of temperature. The points represent experimental data, and the curve represents the simple Flory-Huggins model.

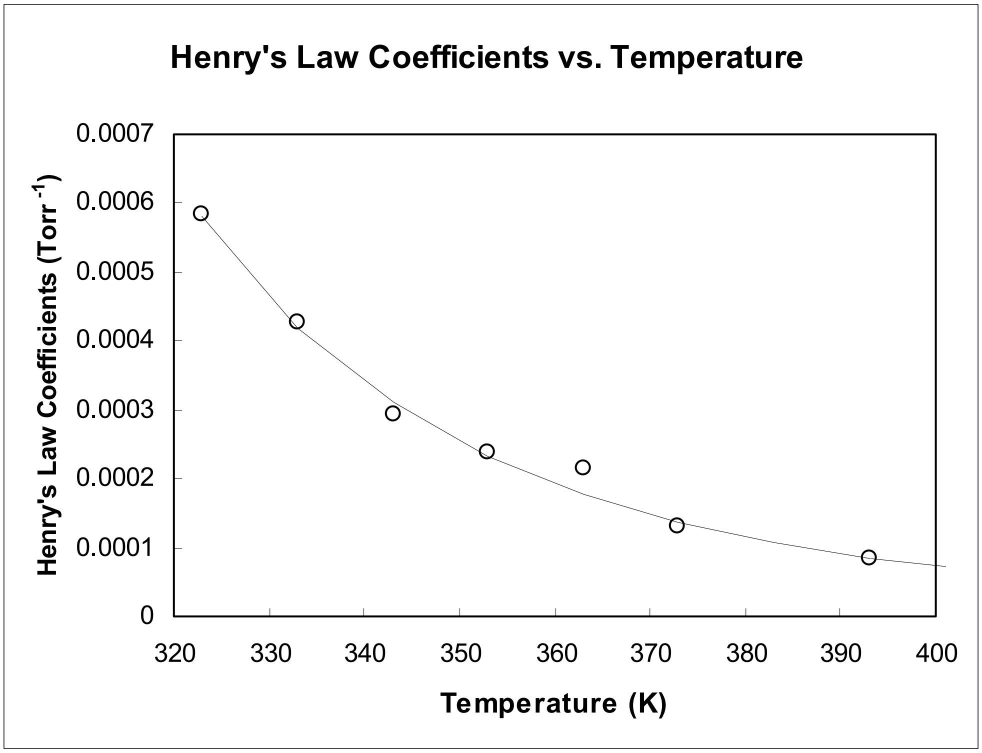

DISCUSSION OF RESULTS

The close agreement between the ellipsometric data and more traditional techniques (infrared spectroscopy and decoration etch) demonstrates its validity. The Flory-Huggins relation closely matched the measured sorption data. The Flory-Huggins relationship was designed for weakly interacting solvent / polymer systems, and at first glance one might assume it would be inappropriate in this case due to the presence of a strongly interacting amino group in the silylation agent. However, the tertiary nature of the amine, coupled with the non-polar nature of the silylated film, makes it reasonable for approximation purposes. The magnitude of the sorption suggests that a significant T_g depression could be occurring in these films. This is especially true in the low temperature, high pressure regime, where the absorbed agent amounted to ~4% of the film by volume. Previous work with CO_2 by other researchers has demonstrated T_g depressions up to 10°C / wt % solvent[22], indicating the risks associated with using polymers with moderate T_g's.

Figure 6.9 shows a plot of reaction rate / C_{SA} vs. the reciprocal temperature in semi-log coordinates. As can be seen, the data is linear, which is in agreement with the front-propagated, reaction rate-limited theory. The activation energy can be extracted from the slope of this plot and equals 100 kJ / mol. If one were to neglect the temperature dependant variations in silylation agent concentration within the film, as other researchers have done, one could calculate an overall activation energy, equals 70 kJ / mol. Clearly the silylation agent concentration plays a significant role in these experiments.

Figure 6.9: A semi-log Arrhenius plot of silylation rate divided by the concentration of silyation agent vs. the inverse temperature.

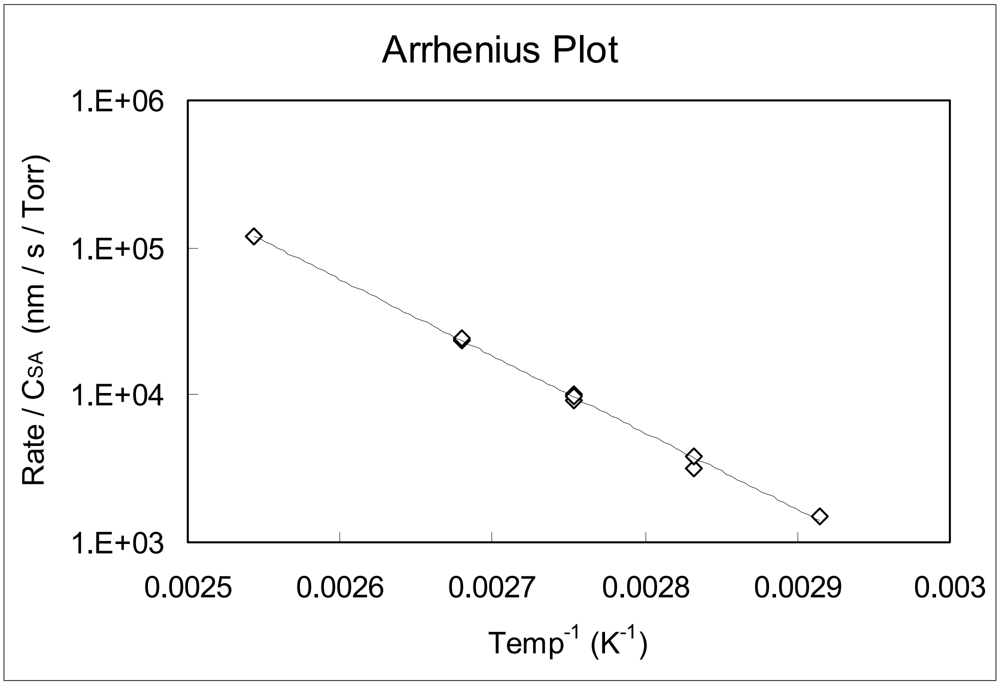

CONCLUSIONS

Ellipsometry is an effective method to evaluate reaction rates and approximate sorption in gas phase reactions with polymer films. The vapor phase silyation of poly (hydroxystyrene) by dimethylaminodimethylsilane appears to be limited by the reaction rate at the interface between reacted and unreacted polymer. Silylation agent pressure affects the reaction rate through a Henry's law dependence of the concentration at the reaction front on the pressure.

References:

(1) MacDonald, S. A.; Schlosser, H.; Ito, H.; Clecak, N. J.; Willson, C. G. *Journal of Photopolymer Science and Technology* **1991**, *4*, 487-495.

(2) Somervell, M. H.; Fryer, D. S.; Osborn, B.; Patterson, K.; Byers, J.; Willson, C. G. *Journal of Vacuum Science & Technology, B: Microelectronics and Nanometer Structures* **2000**, *18*, 2551-2559.

(3) Matsuzawa, N. N.; Mori, S.; Endo, M.; Morisawa, T.; Kaimoto, Y.; Kuhara, K.; Sasato, M. *Journal of Photopolymer Science and Technology* **1998**, *11*, 625-632.

(4) Mori, S.; Matsuzawa, N.; Morisawa, T.; Kaimoto, Y.; Endo, M.; Matsuo, T.; Kuhara, K.; Sasago, M. *Journal of Photopolymer Science and Technology* **1997**, *10*, 603-608.

(5) Simakov, N. N. *Mikroelektronika* **1995**, *24*, 108-112.

(6) Nicolau, D. V.; Jinescu, G.; Fulga, F. *Proceedings of SPIE-The International Society for Optical Engineering* **1992**, *1672*, 461-471.

(7) Dao, T. T.; Spence, C. A.; Hess, D. W. *Proceedings of SPIE-The International Society for Optical Engineering* **1991**, *1466*, 257-268.

(8) Pierrat, C.; Paniez, P.; Martin, P. *Proceedings of SPIE-The International Society for Optical Engineering* **1991**, *1466*, 248-256.

(9) Goethals, A. M.; Lombaerts, R.; Roland, B.; Van den Hove, L. *Microelectronic Engineering* **1991**, *13*, 37-40.

(10) Ellington, J. C., Jr.; Arnett, E. M. *Journal of the American Chemical Society* **1988**, *110*, 7778-7785.

(11) Visser, R. J.; Schellekens, J. P. W.; Reuhman-Huisken, M. E.; Van Ijzendoorn, L. J. *Proceedings of SPIE-The International Society for Optical Engineering* **1987**, *811*, 62-68.

(12) Woollam, J. A.; Bungay, C.; Hilfiker, J.; Tiwald, T. *Nuclear Instruments & Methods in Physics Research, Section B: Beam Interactions with Materials and Atoms* **2003**, *208*, 35-39.

(13) Woollam, J. A.; Green, S. E.; Hilfiker, J. N.; Tiwald, T. E.; Bungay, C. L.; Synowicki, R. A.; Meyer, D. E.; Herzinger, C. M.; Pfeiffer, G. L.; Cooney, G. T. *Proceedings of SPIE-The International Society for Optical Engineering* **2000**, *4099*, 197-205.

(14) Woollam, J. A.; Hilfiker, J. N.; Bungay, C. L.; Synowicki, R. A.; Tiwald, T. E.; Thompson, D. W. *AIP Conference Proceedings* **2001**, *550*, 511-518.

(15) Woollam, J. A.; Johs, B.; Herzinger, C. M.; Hilfiker, J.; Synowicki, R.; Bungay, C. L. *Critical Reviews of Optical Science and Technology* **1999**, *CR72*, 3-28.

(16) Sirard, S. M.; Green, P. F.; Johnston, K. P. *Journal of Physical Chemistry B* **2001**, *105*, 766-772.

(17) Sirard, S. M.; Ziegler, K. J.; Sanchez, I. C.; Green, P. F.; Johnston, K. P. *Macromolecules* **2002**, *35*, 1928-1935.

(18) Somervell, M. Doctoral, University of Texas, Austin, 2000.

(19) Burns, S. D.; Medeiros, D. R.; Johnson, H. F.; Wallraff, G. M.; Hinsberg, W. D.; Willson, C. G. *Proceedings of SPIE-The International Society for Optical Engineering* **2002**, *4690*, 321-331.

(20) Wong, H. C.; Campbell, S. W.; Bhethanabotla, V. R. *Fluid Phase Equilibria* **1997**, *139*, 371-389.

(21) Zimm, B. H.; Lundberg, J. L. *Journal of Physical Chemistry* **1956**, *60*, 425-428.

(22) Condo, P. D.; Paul, D. R.; Johnston, K. P. *Macromolecules* **1994**, *27*, 365-371.

Chapter 7: The Effects of Base Additives on Contrast in Acid-Catalyzed Chemically Amplified Photoresists.

ABSTRACT

Addition of base quenchers to acid-catalyzed chemically amplified photoresists greatly improves their performance. This improvement derives from changes in acid diffusion and from effects associated with the introduction of a threshold dose to initiate deprotection in a resist. The effects of the latter on resist contrast are considered here. Using a high-performance 248nm ESCAP polymer (a ter-polymer of styrene, hydroxystyrene and t-butylmethacrylate commonly used in 248nm photoresists), the effects of base type and loading on contrast were systematically investigated. It was found that quenchers improve imaging in part due to increasing contrast in the chemical reaction step and the subsequent reduction of the transition region from protected to deprotected.

BACKGROUND:

As critical dimensions in photolithography continue to shrink, the demands placed on photoresists become more difficult to meet. Furthermore, some of these demands on photoresist performance contradict one another. For example, photoresists need to be highly photosensitive to minimize the exposure time per wafer, yet the resulting images need to be nearly free of line edge roughness. High photosensitivity requires imaging with as few photons as possible, but using fewer photons tend will tend to increase line edge roughness. The development of chemical amplification nearly two decades ago improved photosensitivity dramatically, but there are issues that may limit the utility of these resists at dimensions smaller than ~30-50nm. These issues are related to photoacid diffusion and its stochastic effects on the deprotection reaction. For the industry to continue to enjoy the benefits of chemically amplified resist technologies, a more rigorous fundamental understanding of the mechanisms associated with chemical amplification is needed.

The fundamental idea of chemical amplification is to use a photosensitive catalyst generator to enable a chemical reaction to occur in a region around the catalyst upon exposure. A single photon can chemically alter a number of sites, rendering them soluble or insoluble in a developer. In its most common form, this idea is implemented by the creation of superacids from photoacid generators and the subsequent catalytic removal of acid labile protection groups on alcohol groups or carboxlic acid groups bound to a polymer. Typical polymer bound functional groups include tBOC or acetal protected alcohols, and esterified carboxylic acids. The superacid is not consumed in the reaction, and can chemically alter a number of sites. The deprotected polymer is soluble in aqueous base developer, while the protected polymer is not.

Resist modeling has mostly assumed that the resist film begins at a neutral pKa and becomes acidic in the exposed areas. In fact, nearly all chemically amplified resists also contain basic additives that greatly improve their imaging performance. Many of the improvements in performance are tied to the fact that the base introduces a threshold exposure dose that must be overcome in order to initiate chemical amplification. This threshold dose has a number of benefits. It improves the resist's response to airborne base contamination by decreasing the relative significance of atmospheric contamination to total base levels. It also helps limit the effect of stray light which can be caused by diffraction, (as is the case in a dense line and space pattern), or by flare. The other major effects are tied to the base's response to spatial concentration gradients that are present in a patterned film. The base additive quenches acid that diffuses from an exposed area into an unexposed one, thereby decreasing diffusion induced blurring of the aerial image. This scavenging effect is particularly important due to the fact that the acid deprotection process is a random walk, and stray acids can potentially travel long distances. These far traveling molecules can greatly affect the roughness of the feature edge. Modeling of these base effects has not been published in the literature. However, nearly every commercial photoresist contains base quenchers, and their effects need to be carefully considered as we approach dimensions where roughness specifications are comparable to the deprotection volume of a single acid.

This chapter investigates the effects of base additives on contrast in chemically amplified resist systems. In simple terms, contrast is the ability of a photoresist to take a diffuse aerial image and transform it into a sharp solubility transition that enables the full resist thickness to be developed. It is becoming ever more challenging to produce a sharp aerial image at the feature sizes that are being produced today, so a high contrast resist is a necessity. Following the definition of Mack[1], contrast, γ, is

$$\gamma = -\frac{\partial \ln R}{\partial \ln I} \tag{7.1}$$

where R is the development rate, and I(x,z) is the spatial intensity of light within a film. The logarithmic nature of the numerator can be rationalized due to the fact that we are interested in *relative* changes in development rate, dR / R, and not absolute changes. This can be seen by the fact that it is not useful to have development rate change of a large amount if the initial development rate is already very large (a resist with an initial development rate of 1,000 nm/s that increases by 100 nm/s upon exposures won't work well, whereas the same development rate change in a resist with an initial development rate of only 1 nm/s could perform well). The logarithmic nature of the denominator is due to the constant *relative* intensity profile that is produced in a thin film upon interaction with an aerial image. We can change the absolute dose that a point in the film receives by changing the incident dose, but cannot affect the relative intensity without altering exposure conditions. The contrast of a resist affects numerous resist performance metrics, including resolution, line edge roughness (LER), process windows, etc. The lithographic imaging equation,

$$\frac{\partial \ln R}{\partial x} = -\gamma \frac{\partial \ln I}{\partial x} \tag{7.2}$$

where x is the spatial position in the plane of the wafer, illustrates why the contrast plays such an important role. The first term, d(lnR) / dx is the development rate gradient, and is a measure of the final resist performance. It plays a substantial role in all of the aforementioned performance metrics. The term d(ln I) / dx is commonly referred to as the image log-slope (ILS) and is a measure of the quality of the aerial image at a feature edge. Thus, contrast is a measure of a resist's ability to capture the information content produced by the stepper in the form of intensity modulation, and transform it into a topographical recording.

Historically, resist contrast has been measured by evaluating so-called Hurter-Driffield (H-D) curves. A H-D curve is created by exposing a photoresist to a series of exposure doses, processing the resist (PEB, development), and then measuring the remaining photoresist thickness for each dose. The contrast is then calculated using thickness as a substitute for development rate, which assumes a constant development rate. By dividing the difference between initial and final thickness by the initial thickness, and plotting this quantity vs log I, one can measure the slope to determine the contrast. This technique lacks the rigor of other techniques, such as use of a dissolution rate monitor[2]. Many of the weaknesses arise due to the potential for spatial intensity variations in a film (and hence spatial composition variations). However, the technique's accuracy can be improved if two rules are followed. First, the resist must be almost completely transparent so absorption does not decrease the exposure intensity with depth (although this can be worked around). Second, the photoresist must be on a optimized anti-reflection coating to eliminate standing waves that can greatly affect the through-depth spatial composition. However, even if these considerations are taken into account, it may still be very challenging to obtain all the desired information (as will be discussed later).

A difficulty associated with the metric for contrast is that it neglects the effects of diffusion within a resist. One can easily imagine a case where a photoresist has an extremely high measured contrast, but has such high acid diffusion lengths that all information content is diffused away, rendering it useless for actual imaging. The lithographic imaging equation places all resist performance issues in the contrast term. But for contrast to be an ideal metric, it would need to account for resist response to a very sharp aerial image (very high ILS). However, contrast is nonetheless an extremely useful metric, and base quenchers would only improve the diffusional characteristics of the resist, as discussed earlier.

THEORY

By assuming that the development rate is a function of polymer blocking only, equation 7.1 can be separated into a more useful form:

$$\gamma = -\frac{\partial \ln R}{\partial F}\frac{\partial F}{\partial \ln I} \tag{7.3}$$

where F is the fraction of blocking groups on a polymer that are blocked (going from 1 to 0 as exposure occurs). Note that the possibility that the salt resulting from the acid-base reaction could alter the dissolution rate's dependence on F is neglected here. Thus, it is assumed that the addition of base quenchers to a resist only alters contrast through a change in the way in which a photoresists blocking fraction's responds to light. In other words, base additives only affect contrast through alteration of the acid/ base/ blocking group chemistry and transport, and have little bearing elsewhere. The development contrast may also have enormous bearing on the overall contrast of the photoresist.

In this chapter, the effects of base on the chemical amplification contrast are considered. To monitor the fractional conversion we use a modified H-D type analysis. Rather than plotting the final developed thickness, the thickness is plotted here after the post-exposure bake. If it is assumed that all the volatile protection groups leave the film and the film compresses accordingly, the thickness loss will be directly proportional to the blocking fraction. This assumption is consistent with the results of Burns, et al[3], who demonstrated that the chemical conversion, as measured by infrared spectroscopy and the thickness loss metrics due to volatilization of protection groups is effectively identical for the poly (tBOC hydroxystyrene) system, (note that this is not true in many resist systems, although techniques such as infrared spectroscopy can be used as a substitute for thickness). By obtaining the blocking fraction as a function of dose, we can investigate the effect of bases on the chemical amplification contrast directly. The chemical amplification contrast dictates the width of the region in which the polymer transitions from fully protected to fully deprotected, also known as the "blend width". A resist with a higher chemical amplification contrast will have thinner blend widths, resulting in a higher overall contrast (and possibly reduced line edge roughness).

This chapter presents three simple models to illustrate how bases improve the chemical amplification contrast of a photoresist. First, a simple graphical model shows the concept intuitively. Second, a theoretical derivation relating contrast as a function of clearing dose (E0), which is a strong function of base loading, will be used to generate a broad methodology to look at contrast and diffusion. Finally, a simple kinetic model based on first order reaction kinetics is derived and quantitatively compared to experimental results.

Graphical Model

Consider the interaction of two hypothetical resists with an aerial image. Figure 7.1 shows an arbitrary aerial image for a 200nm space (note that this is a plot of *relative* intensity vs. position). Figure 7.2 shows a H-D type chemical amplification contrast curve of two hypothetical resists. The first contains no base, while the second contains a small amount. As the dose increases, the resist with base remains fully protected until all the base is consumed, and then deprotects over the same dose increment as the first resist (consistent with the results of Pawloski[4]). These hypothetical resists have doses-to-deprotection (Ed's) of 3 mJ/cm^2 and 9 mJ/cm^2 respectively. Their deprotection process take place over a dose increment, ΔE, of 2 mJ/cm^2. At the nominal feature edge of the aerial image, the relative intensity is 0.5 (as such, we'd need to expose the resist to ~2x the dose to clear to get the desired feature size). From the contrast curve for the first resist, the dose where deprotection begins is at 1/3 the dose of full deprotection, which corresponds spatially to nearly 50nm in figure 7.1 (the x position at which the intensity = 0.5 * 1/3). The second resist has a deprotection onset dose of only 7/9 of the dose to full deprotection, which corresponds to only 20nm spatially. In other words, the second resist makes the diffuse image much sharper, while the first resist doesn't perform nearly as well. This dramatic change in blend width is the result of the fortuitous fact that the addition of base doesn't dramatically alter the chemical amplification kinetics. The acid-base reaction is faster than the deprotection reaction, and once complete, the resulting salt plays little role in the deprotection reaction.

Figure 7.1: Arbitrary Aerial Image.

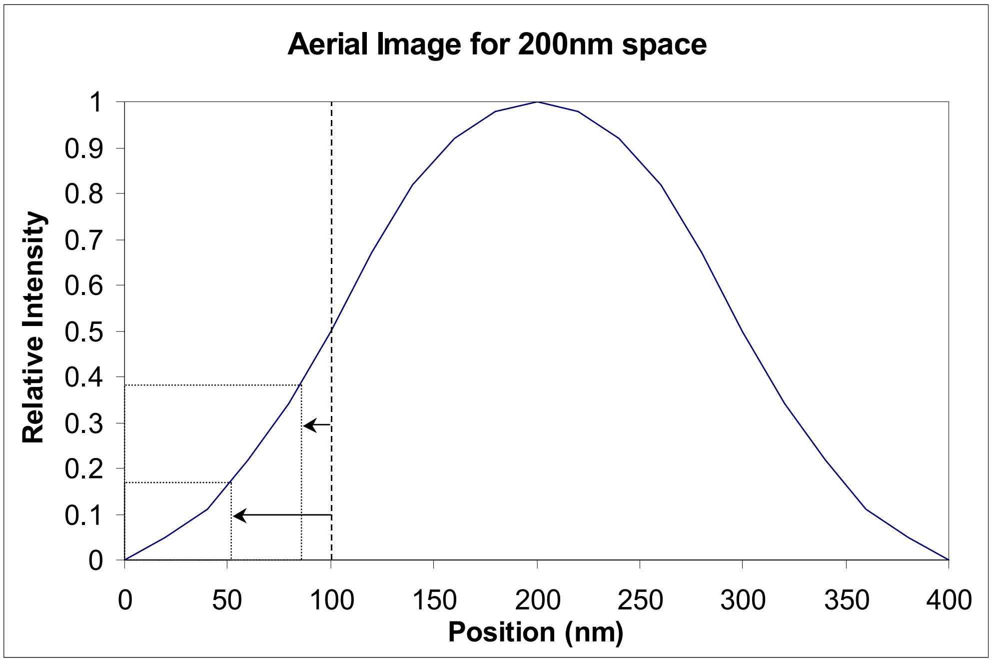

Figure 7.2: Chemical Contrast curves for two hypothetical resists.

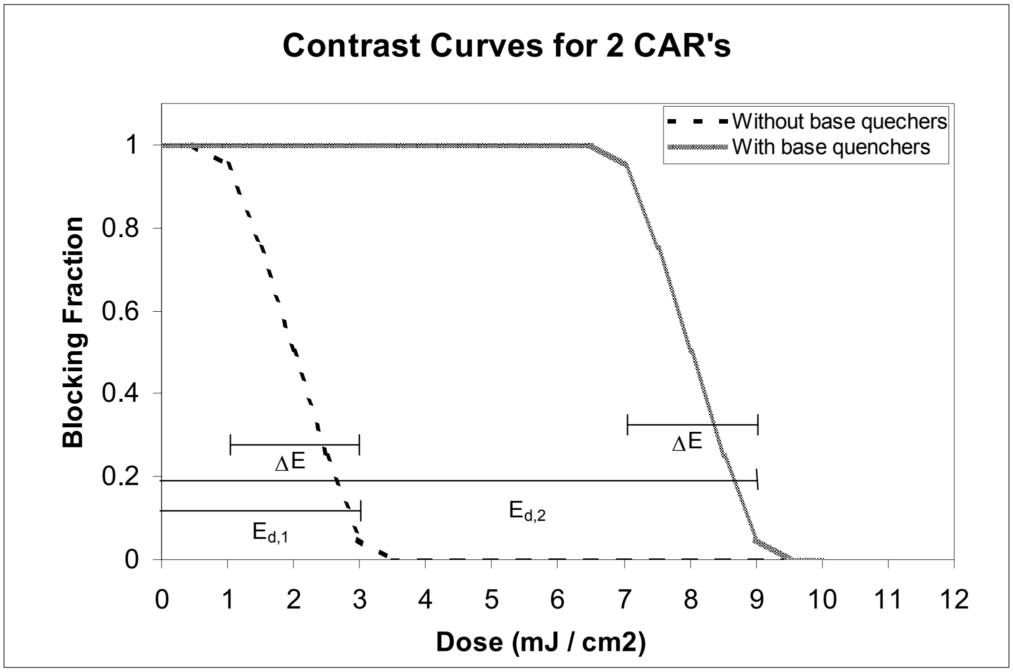

The effect can be seen mathematically as well. Starting with the definition of contrast from equation 7.3, we can see that if the functional form of d lnR / dF and dF / dI don't change with added base, then the contrast should go up linearly with the increasing dose requirements resulting from the added base. However, a small modification needs to be made. As base loading becomes a large fraction of the photoacid generator (PAG) loading, the slope of the deprotection curve will decrease as the concentration of PAG at the deprotection onset dose decreases. This can be seen by assuming that d F / dI will scale linearly with dG / dI, where G is the PAG loading. Assuming first order exposure kinetics, and the nomenclature of Dill, we see a new relationship:

$$\gamma \propto \frac{\partial \ln R}{\partial F} I\ C\ G_O \exp(-C\ I) \tag{7.4}$$

which clearly contains the effects of decreasing PAG concentration as a function of increasing base loading in the added decaying exponential.

Simple Kinetics Model

Starting with the contrast equation shown in equation 7.3, we can also solve for contrast as a function of dose assuming first order kinetics in exposure, the acid-base reaction and the deprotection reaction. This is an extremely simplified model, and a more thorough analysis is possible using a model similar to that of Hinsberg et al[5-7]. Additionally this model neglects effects such as non-stoichometric quenching of the base, as described by Pawlowski[4], and the effects of salt on the deprotection reaction. Overall, the utility of this simple model doesn't lie in its rigor, but rather in its illustration of the effects of bases. The first order equations are shown as equations 7.5-7.8.

$$H_o = G_o - G = G_o(1 - \exp(-CIt)) = G_o(1 - \exp(-CE)) \tag{7.5}$$

$$\partial H \big/ \partial t = -k_{quench}\, H\; B \tag{7.6}$$

$$\partial F \big/ \partial t = -k_{amp}\, H\; F \tag{7.7}$$

$$\partial B \big/ \partial t = -k_{quench}\, H\; B = \partial H \big/ \partial t \tag{7.8}$$

where H is acid concentration, H_o is acid concentration after exposure, G is PAG concentration, G_o is initial PAG concentration prior to exposure, C is Dill's parameter, *I t* is the total dose (equals E) and B is base quencher concentration. Solving for H and B as a function of time using equations 7.6 and 7.8, we find:

$$H = \frac{H_o H^E}{H_o - B_o \exp(-H^E k_{quench}\; t)} \tag{7.9}$$

$$B = \frac{-B_o H^E}{B_o - H_o \exp(H^E\; k_{quench}\; t)} \tag{7.10}$$

where H^E is the excess acid after exposure and quenching, equal to $H_o - B_o$. We can further solve for the polymer's blocking fraction as a function of time by plugging equation 7.9 into equation 7.7, integrating and rearranging:

$$F = F_o \left[\frac{H^E}{H_o \exp(H^E\; k_{quench}\; t) - B_o} \right]^{\frac{k_{amp}}{k_{quench}}} \tag{7.11}$$

where Fo is the initial blocking fraction. The fraction protected F, can be plotted against dose for a typical resist using typical resist parameters and equation 7.5 (Dill's first order exposure equation).

In order to see the dependence of contrast on base loading, we must first modify equation 7.3 using the chain rule.

$$\gamma = -\frac{\partial \ln R}{\partial F} E \frac{\partial F}{\partial E} \quad = \quad -\frac{\partial \ln R}{\partial F} E \frac{\partial F}{\partial H_o}\frac{\partial H_o}{\partial E} \qquad (7.12)$$

The first term, dlnR / dF will be treated as a constant for a given resin. The fourth term is obtained by simple differentiation of equation 7.5:

$$\frac{\partial H_o}{\partial E} = Go\, C \exp(-C\ E) \qquad (7.13)$$

The third term in equation 7.12 can be determined by differentiating equation 7.10 with respect to H_o to obtain the following:

$$\frac{\partial F}{\partial H_o} = -\frac{k_{amp}}{k_{quench}} F\left(\frac{1}{H^E} - \frac{\exp(k_{quench}\, t\ H^E) + H_o\, k_{quench}\, t \exp(k_{quench}\ \ t\ H^E)}{H_o \exp(k_{quench}\ \ t\ H^E) - B_o}\right) \qquad (7.14)$$

Contrast as a function of intensity is shown in figure 7.5 with experimental data. It is now clear that even with competition between the acid neutralization reaction and the deprotection reaction, contrast improves substantially with added base.

EXPERIMENTAL

Materials

An ESCAP ter-polymer made up of 60 % hydroxystyrene, 23% t-butyl methacrylate, and 17% styrene, donated by DuPont Electronic Polymers, was dissolved in PGMEA to create a stock polymer solution. The weight-averaged molecular weight of the polymer was of 12,300. Triphenylsulfonium Nonaflate (TPS-Nf), donated by AZ Clariant Corporation, was diluted in PGMEA to make a stock solution. Three bases were purchased from Aldrich Company, and used directly from previously unopened bottles. These included trioctylamine, triethanolamine, and tetrabutylammoniumhydroxide. Dissolving the bases in PGMEA created stock base solutions. From these stock solutions, thirteen resists were created. All resists contained 2 wt % TPS-Nf (relative to the polymer). The first solution contained no base, and the other 9 solutions were formulated by adding TPS-Nf and three different concentrations or 5, 10 and 20% (molar relative to the TPS-Nf) of each of the three bases. All materials used in the resists are shown in figure 7.3. Additional PGMEA was added to some of the formulations so that the polymer / solvent ratio was a constant, causing the solutions to coat at the same thickness for a given spin speed.

Figure 7.3: Materials used in these experiments

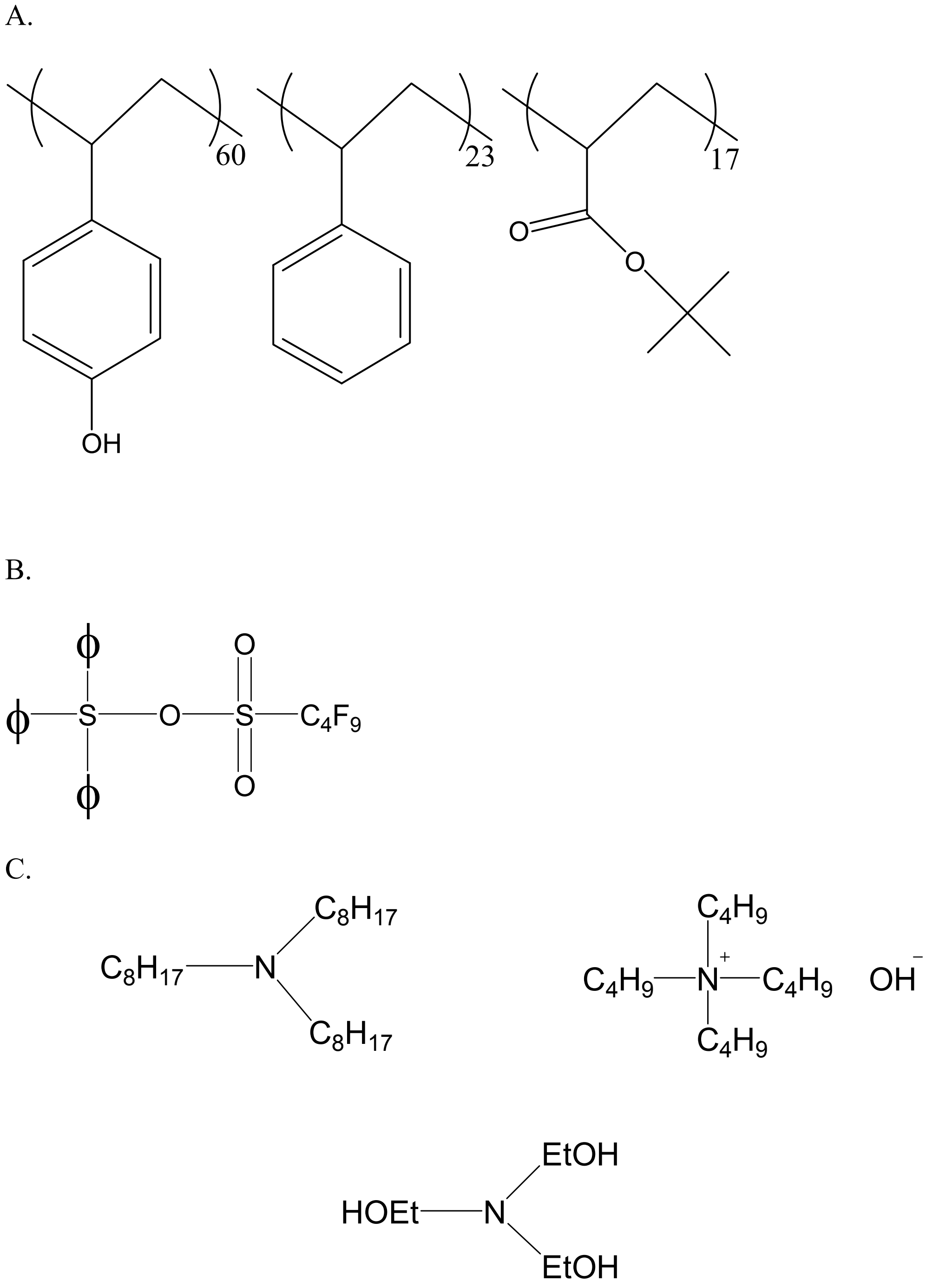

Processing

All experiments were performed at International SEMATECH. Wafers were coated, post apply baked, and developed on a FSI Polaris 2000. Wafers were exposed on a SVG Microscan III, using binary illumination (NA = 0.6, σ = 0.6), and post exposure baked on an in-line track. All bake conditions were 60s at 130^{o}C. Images were created using a binary mask. Development was performed for 60s using CD26 (a 0.26N, surfactant-free, aqueous TMAH developer). Resist thickness was measured with a Rudolph S300. All resists were coated on 59.5nm of Brewer Science DUV 30J (optimized for the first reflectivity minimum in UV6). All formulations were coated at 330nm in order to avoid swing curve effects from wafer to wafer. The absorbance of the resists was fairly low (~0.5 um^{-1}) in order to ensure that the energy deposition within the film was uniform.

The ten resists were coated on ARC, post application baked, and the initial thickness was measured in 62 locations. The resists were flood exposed in 61 locations with exposure doses between 2 and 52 mJ / cm^2 (1/2 mJ / cm^2 increments for the first 20 sites, and 1 mJ / cm^2 for the remainder). The thickness was measured after exposure, enabling us to determine the extent of protection. This is based on the idea that the volatilization of the protection group causes an instantaneous and proportional film thickness loss. Ito, et al showed that a small percentage of the deblocked t-butyl groups react with the film, and it was verified with infrared spectroscopy that this effect was minimal in this system (the precision associated with the thickness measurement process greatly outweighs the potential accuracy gains associated with infrared spectroscopy). The resulting thickness loss and chemical amplification contrast are shown as a function of dose in figures 7.4 and 7.5. Additionally, the three parameter fit kinetic model results are shown in figures 7.4 and 7.5. All theoretical curves use parameters of (k_{amp} = $0.42s^{-1}$, k_{quench} = $3.3s^{-1}$, and C = $0.028cm^2/mJ \cdot s$). The concentration variables are normalized to their initial values, with the exceptions of the acid and the bases, which are normalized to the initial PAG concentration. The zero-base, and 20mol% TOA resists were exposed with a binary mask, and 180nm nested features at best dose and focus are shown in figure 7.6.

Figure 7.4: Blocking fraction as a function of dose. Solid lines represent theory, triangles denote TOA, squares denote TBAH, and triangles triethanolamine.

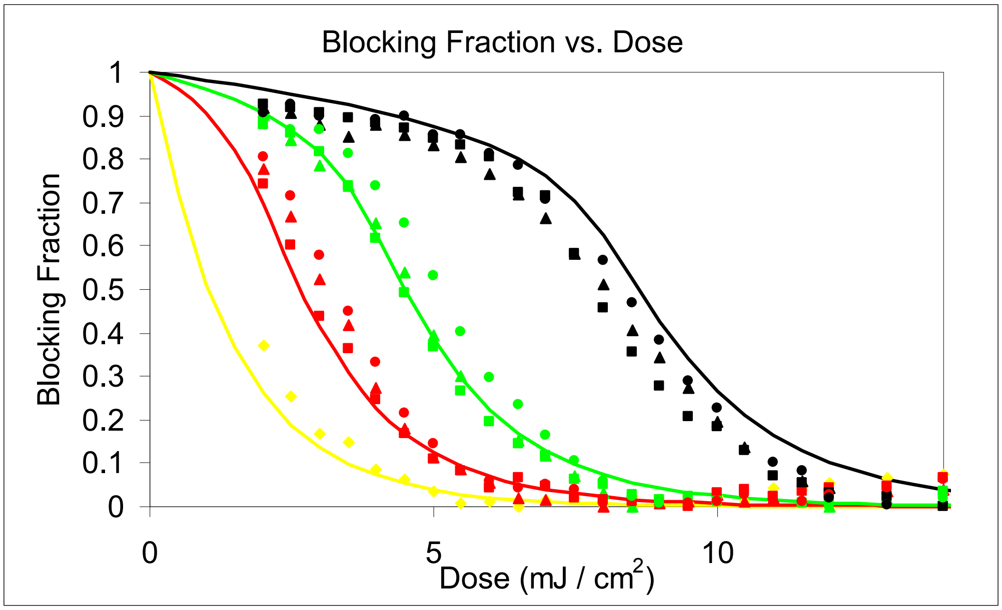

Figure 7.5: Chemical Contrast as a function of dose. Solid lines represent theory, triangles denote TOA, squares denote TBAH, and triangles triethanolamine.

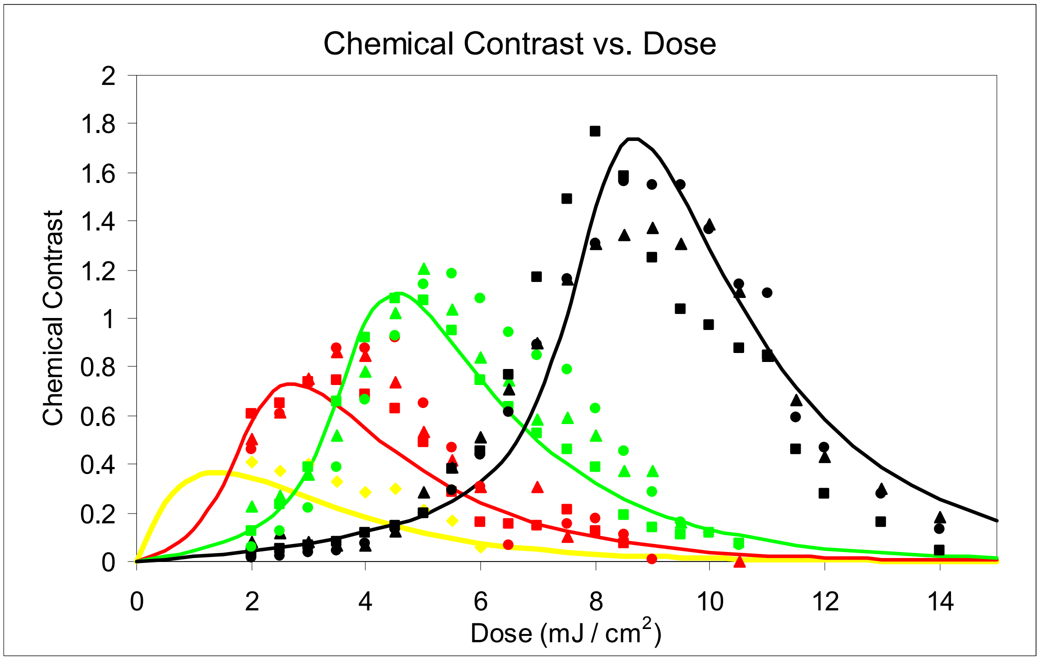

Figure 7.6: Top down and cross-section SEMs of 180nm nested lines with both the zero base (a & b), and 20mol% TOA (c & d) resists. Note the improved sidewall angles and lower line edge roughness in the 20mol% base case.

A&B: Zero Base

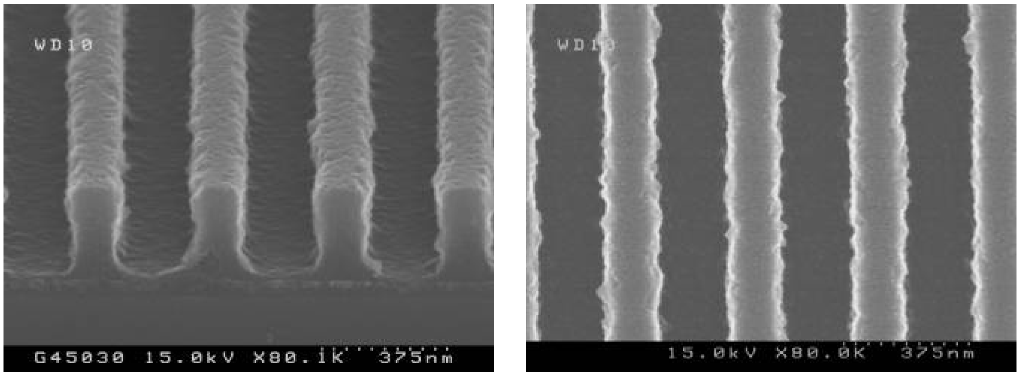

C&D: 20mol% TOA

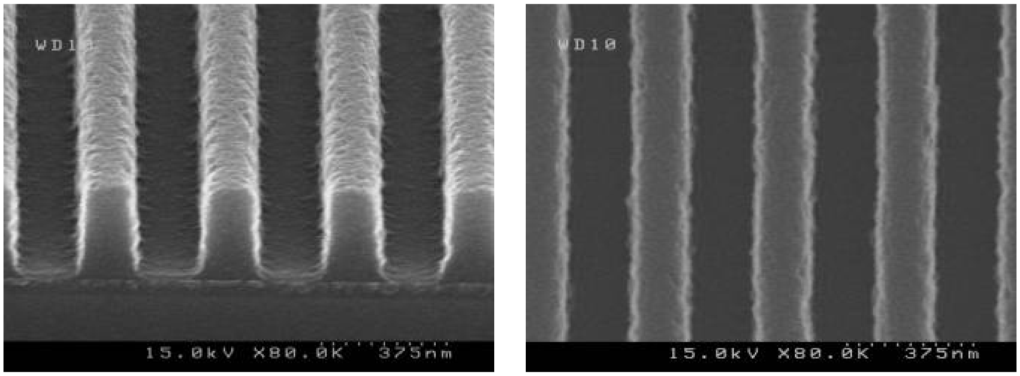

DISCUSSION OF RESULTS

Considering the limited accuracy of the first order reaction assumptions, theory fairly closely matches experiment, as can be seen in figures 7.4 and 7.5. The increase in chemical amplification contrast from a value of ~0.4 to a value of 1.7 with the addition of only 20 mol% base is quite impressive. This means the contrast of the overall resist is greatly improved. Additionally, the three bases behave similarly in these experiments. It is possible that their diffusive behavior could cause discrepancies in their imaging performance.

The antiflection coating used in these experiments dampened standing wave effects. However, standing waves were not entirely eliminated. Using Prolith, it was found that these exposures had an Imax / Imin ratio of <1.15, (using n & k data provided by the supplier for the ARC, and values measured on a Woollam ellipsometer for the resist). The magnitude of these standing waves was sufficiently small that we could obtain rough kinetics of deprotection. In fact, the real chemical amplification contrast values are likely larger than those we measured, as a result of the imperfect ARC. Diffusion of the generated acid would make these effects smaller. The standing waves make it difficult to measure accurately the dissolution rate as a function of conversion, due to the extreme sensitivity of the dissolution rate to blocking fraction.

As mentioned previously, the separation of diffusion effects from contrast effects on final resist imaging performance is challenging. However, it is clear that the addition of base to resists improves the acid profile dramatically prior to the bulk of the deprotection process. Diffusion may degrade the effects of the addition of base, but the improved starting point surely improves the final image. The images shown in figure 7.6 clearly indicate the great improvement in performance of the resist. Line edge roughness is substantially improved, as is the profile. A more thorough analysis of the imaging effects of base is underway, and should be available soon.

CONCLUSIONS

Base additives play an enormous role in the performance of chemically amplified photoresists. Analysis of the standard photoresist metric, contrast, clearly illustrates one of the mechanisms by which this improvement occurs. The relatively close agreement between the experimental data and a simple kinetic model shows that the theories presented here capture the effects of bases on contrast. As patterned photoresist sizes approach the deprotection dimensions of many acids, a proper understanding of the nature of the chemical ampification reaction as it occurs in a resist film is becoming more important than ever. This understanding cannot occur without taking into account the effects of bases.

References:

(1) Mack, C. A. *Inside ProLith*, 1997.

(2) Burns, S. D.; Schmid, G. M.; Trinque, B. C.; Willson, J.; Wunderlich, J.; Tsiartas, P. C.; Taylor, J. C.; Burns, R. L.; Willson, C. G. *Proceedings of SPIE-The International Society for Optical Engineering* **2003**, *5039*, 1063-1075.

(3) Burns, S. D.; Medeiros, D. R.; Johnson, H. F.; Wallraff, G. M.; Hinsberg, W. D.; Willson, C. G. *Proceedings of SPIE-The International Society for Optical Engineering* **2002**, *4690*, 321-331.

(4) Pawloski, A. R.; Christian; Nealey, P. F. *Chemistry of Materials* **2002**, *14*, 4192-4201.

(5) Houle, F. A.; Hinsberg, W. D.; Morrison, M.; Sanchez, M. I.; Wallraff, G.; Larson, C.; Hoffnagle, J. *Journal of Vacuum Science & Technology, B: Microelectronics and Nanometer Structures* **2000**, *18*, 1874-1885.

(6) Hinsberg, W.; Hoffnagle, J.; Houle, F. *Microlithography World* **2000**, *9*, 16, 18, 20-22.

(7) Houle, F. A.; Hinsberg, W. D. *Book of Abstracts, 219th ACS National Meeting, San Francisco, CA, March 26-30, 2000* **2000**, CHED-998.

Chapter 8: Summary & Future Work.

SUMMARY

Top Surface Imaging is a technique that is capable of extremely high-resolution patterning. It possesses many advantages over traditional lithography, but also suffers from significant line edge roughness. Previous research demonstrated that it is possible to print smooth images by using the polymer PFAS. TSI using PFAS was investigated for application to 157nm lithography, and it performed well. However, while investigating 157nm lithography applications, it was found that previous theories about the requisite material properties for smooth imaging were not correct; high Tg and optical transparency are not sufficient for smooth TSI imaging. Using tBOC-styrene, TSI was then investigated for use in low-voltage electron beam lithography. Initially, the resist printed poorly with significant amounts of LER. However, by adding large amounts of base to the formulation, thereby altering the deprotection profile, the resist printed very well. A significant effort was made to understand the effects of bases on line edge roughness and initial theories were generated and tested, both for TSI and traditional base-developed systems. An enormous effort was made in conjunction with the Willson group chemists to duplicate the behavior of PFAS in new polymer systems. Although many interesting results came out of the work, no smooth images resulted. It became clear that mere alteration of the polymer structure could not easily fix the problem of line edge roughness. PFAS appeared to the anomaly of TSI, rather than the key to a new class of polymers that print smoothly. The high-Tg, low-mobility polymers that came out of the synthetic effort did improve low frequency roughness, a phenomena that was shown to be the result of surface area minimization, and could be analyzed by a Rayleigh instability analysis. In order to verify that sorption induced plasticization of the polymer was not occurring, a chamber was constructed to ellipsometrically monitor sorption and reaction kinetics in real time. The experiments enabled by the chamber shed light on the nature of the silylation reactions, and the sorption that occurs in these systems, but proved that line edge roughness was not being induced by mobility in the polymeric species. Overall, the only process variables that improved line edge roughness were the addition of base quenchers and improvement of aerial image.

DISCUSSION / CONCLUSIONS

TSI consists of three major process steps: 1) the exposure & generation of a deprotection profile, 2) the silylation of the deprotected region, and 3) the selective etch of the unsilylated regions. This work has largely focused on the investigation of problems that are associated with second step. The justifications for this focus were reasonable. The first step is identical to that performed in traditional, aqueous base-developed systems that contain less roughness than TSI. The third step is used commonly in industry for bilayer etch transfer processes, and the processes have been carefully optimized. Furthermore, the majority of previous research on TSI was focused on the etch transfer step, to no avail[1-6].

(Additional etch optimization was performed by the author, but is not presented here.) In the course of this dissertation, it has been shown that roughness likely does not result from the second process step. Numerous polymers were generated that have extremely high Tg's throughout all processing steps, and still print roughly. Additionally, it is likely that roughness is not the result of the etch process for the aforementioned reasons. Therefore, it is likely that the roughness is a result of the deprotection profile itself. This idea is supported by the fact that the addition of base quencher, which only affects the deprotection profile, was the only thing that greatly impacted roughness. In essence, TSI may be recording the deprotection profile more accurately than wet-developed systems do, to its detriment. This idea evokes two important questions. First, what is it about the deprotection profile of PFAS that enables it to print smoothly? Second, why do wet-developed systems print more smoothly than TSI systems with the same deprotection profile? Both questions probe at the fundamental nature of the deprotection reaction and the second includes the wet-development process. Trying to understand these fundamental areas is the subject numerous doctoral dissertations and papers. Researchers at NIST, IBM, UC Berkeley, UT, and elsewhere are studying topics such as the "sphere of influence", or the region around a photo-generated acid that is deprotected. The effects of acid diffusion on chemically amplified photoresists are the subject of two doctoral dissertations at UT alone and base-development process has been investigated extensively, and still is not fully understood. The consequences of these studies are of paramount importance to the continuation of high-photospeed, high-resolution lithography.

The two questions proposed earlier about the theory that roughness in TSI results from the deprotection profile are not unanswerable. From a peripheral standpoint, one can propose possible solutions. PFAS has an extremely strange deprotection profile, as was seen in chapter 2, and the small deprotection volume of that system may act as smaller pixelation, thereby improving roughness. It is possible that the deprotection profile of PFAS is the key to its performance. In the case of wet-developed systems, in order for development to occur, the entirety of a polymer chain must be deprotected to a certain fractional conversion, else it remains insoluble. This threshold criteria may act to smooth out a rough deprotection volume. Furthermore, in wet-developmed systems, stochastic noise associated with single stray acids affects only the area where the acid walks, whereas in TSI, due to the anisotropic etch step, they can affect the areas below them as well. These answers are conjecture at best, but point to an area that needs to be further investigated.

FUTURE WORK:

Background

The advantage of chemical amplification is that a single photon can alter a large volume, but that also may become its shortcoming. Photoacid generators are introduced in low concentrations (~4wt%), and at low photoacid conversion (<10%), all protection groups can be removed. A back of the envelope calculation shows that a single acid can deprotect a sphere with a radius of ~4nm (in collaboration with researchers at NIST & IBM the Willson gropu is probing this number more accurately, but this value is approximately correct). A deprotected sphere with a diameter of 8nm is enormous in light of the fact that line edge roughness targets aim for 3σ values of LER of < 4nm according to the ITRS. This is an especially large problem at the feature edge, where the concentration of acid is low, and isolated acids have large spheres of influence and they dictate roughness.

In reality, the deprotection process has a random nature, and the deprotection profile of a single acid is more accurately described with a random walk. This introduces further noise onto an already rough acid profile. The diffusion distance of a single acid can be as much as 40nm, as measured by UT, NIST and IBM[7, 8]. It is fair to say that the feature edge of a chemically amplified resist is a messy thing. The implications of the rough deprotection profile on TSI are not straightforward. It is well accepted that the deprotection profile at the feature edge is fairly rough, but it isn't obvious *a priori* which system, TSI or wet-developed, would behave better with a rough profile. Furthermore, the influences of bases on the deprotection profile are not fully understood. To this end, recommended future work on this project is to investigate the nature of the deprotection profile further, and create polymers that do not rely on chemical amplificiation. These topics are broken into three areas: 1) fundamental investigations on the nature of the deprotection process, and studies on the influence of base quenchers, 2) simple simulations focused on photoacid generation and its random walk, and 3) creation of a non-chemically amplified TSI scheme that enables high photospeed, and high resolution.

Future Work Topics

1. Fundamental investigations of line edge roughness & the deprotection profile:

Within the lithography community there is not a consensus on the origins of line edge roughness. Part of the difficulty in understanding LER likely arises from the fact that it can vary as a result of alteration of an enormous number of variables, including: polymer structure, polymer molecular weight, additives, developer concentration, developer additives and bake conditions. All of these parameters influence roughness in various ways, and the mechanisms by which each interacts are not straightforward. Furthermore, very little data is available in the literature. Most photoresist optimization is performed behind closed doors at resist companies, and seldom sees the light of day. The work that was begun on the effects of base quenchers in chapter 7 illustrates this idea well. The dramatic effects that base quenchers have on LER are very interesting, but their theoretical underpinnings are not well understood in the literature. It is obvious that resist companies have studied this area extensively, as they have been using base quenchers in photoresists for over a decade. Although it is possible that photoresist companies can shoulder the role of improving LER on their own, it may be too great a problem for individual companies to tackle. Collaboration between companies, universities and national labs may be necessary. In order for efficient optimization of these systems to occur, a systematic study of the effects of fundamental resist parameters on LER should be undertaken. There are numerous simulation packages, both academic and industrial that are capable of investigating roughness effects, but without a body of data to compare them to, they are hard to calibrate or evaluate.

The work presented here illustrates that the deprotection profile may be worse than previously thought, and present theory is incapable of proving or disproving this idea. All of the resist parameters listed earlier that effect LER also affect the deprotection profile through various mechanisms, so it is possible that it is the critical phenomenon. It is unclear if LER in TSI and wet-developed systems is a result of a noisy deprotection profile, or some other mechanism or mechanisms, but it is a possibility worthy of further research.

2. Basic simulations of the deprotection process

The deprotection reaction is a complicated thing- far more complicated than is alluded to in this document. In the deprotection process, reaction and diffusion are occurring simultaneously, and the diffusion coefficient is changing significantly as this occurs, causing numerous difficulties. Furthermore, the feature edge is quickly approaching size scales in which continuum diffusion models are no longer adequate for explaining the effects that are seen.

Work by Schmid, et al has shown that so-called “meso-scale” simulations are capable of capturing many of the trends that are present in chemically amplified photoresists[9-11]. These Monte Carlo based techniques, which represent photoresist components as discrete points with various connectivity and physical properties have shown many of the trends present in systems such as tBOC styrene. It may be very instructive to use these types of models with significant simplifications to investigate first-order effects on the deprotection profile. A streamlined model that neglects polymer lattice generation, reptation, and other polymer effects, and focuses on photoacid generation, movement and reactions with a static lattice would be useful. It could enable a better understanding of the effects of resist components on the deprotection profile from a given energy deposition profile without the rigor that can greatly increase simulation time.

3. Non-chemically Amplified TSI schemes.

If it is true that LER in TSI systems is a result of chemical amplification and its poor deprotection profile, then non-chemically amplified systems have the potential to print smoothly. At the very least, a non-chemically amplified TSI system would give insight into the origins of LER in these systems. If line edge roughness in wet-developed systems results from the same phenomena, then there is reason to believe that a non-chemically amplified TSI system would be one of the best methods to create a smooth imaging, high-resultion photoresist that has a fast photospeed.

In a non-chemically amplified scheme, each pixel, or chemical component must have some interaction with a photon. If an aqueous base developed system is to be used, the photoresist must be fairly transparent in order for the energy deposition profile to have square sidewalls. However, transparent components by definition do not interact strongly with photons, and do not easily undergo photochemistry while simultaneously being transparent. (Chemically amplified photoresist have a low concentration of photoactive components, thus the resin is transparent through dilution, while still retaining photoactivity). A non-chemically amplified system would run into the contradictory state of needing a high absorbance in order to have a fast photospeed, but simultaneously needing to be transparent enough to have a good energy deposition profile. (A way to get around this requirement would be to have a photoactive compound that "bleaches" or becomes transparent as the photochemistry occurs, but this just adds complexity to the design requirements.) This contradiction would not be present in a non-chemically amplified TSI system. In fact, the more absorbing the photo-active compound is, the faster the photo-resist would be (assuming a constant quantum efficiency). A TSI system may then be the easiest way to create a revolutionary non-chemically amplified resist scheme. It has the potential to be very photosensitive, while still having an energy deposition profile that can result in square sidewalls, due to the anisotropic etch step.

References:

(1) Wu, T.-J.; Lin, L.-T. S.; Chao, L.-C. In *U.S.*; (Taiwan Semiconductor Manufacturing Company, Taiwan). Us, 2003, pp 5 pp.

(2) Hutchinson, J.; Rao, V.; Zhang, G.; Pawloski, A.; Fonseca, C.; Chambers, J.; Holl, S.; Das, S.; Henderson, C.; Wheeler, D. *Proceedings of SPIE-The International Society for Optical Engineering* **1998**, *3333*, 165-175.

(3) Steinhausler, T.; Gabor, A. H.; White, D.; Blakeney, A. J.; Stark, D. R.; Miller, D. A.; Rich, G. K.; Graffenberg, V. L.; Dean, K. R. *Proceedings of SPIE-The International Society for Optical Engineering* **1998**, *3333*, 122-131.

(4) Goethals, A. M.; Van Roey, F.; Sugihara, T.; Van den hove, L.; Vertommen, J.; Klippert, W. *Journal of Vacuum Science & Technology, B: Microelectronics and Nanometer Structures* **1998**, *16*, 3322-3333.

(5) Huang, Z. S.; Melaku, Y.; Nguyen, W. *Japanese Journal of Applied Physics, Part 1: Regular Papers, Short Notes & Review Papers* **1998**, *37*, 2373-2380.

(6) Vertommen, J.; Goethals, A. M. *Journal of the Electrochemical Society* **1997**, *144*, 2461-2467.

(7) Lin, E. K.; Soles, C. L.; Goldfarb, D. L.; Trinque, B. C.; Burns, S. D.; Jones, R. L.; Lenhart, J. L.; Angelopoulos, M.; Willson, C. G.; Satija, S. K.; Wu, W.-l. *Proceedings of SPIE-The International Society for Optical Engineering* **2002**, *4690*, 313-320.

(8) Lin, E. K.; Soles, C. L.; Goldfarb, D. L.; Trinque, B. C.; Burns, S. D.; Jones, R. L.; Lenhart, J. L.; Angelopoulos, M.; Wilson, C. G.; Satija, S. K.; Wu, W.-l. *Science (Washington, DC, United States)* **2002**, *297*, 372-375.

(9) Schmid, G. M.; Burns, S. D.; Stewart, M. D.; Willson, C. G. *Proceedings of SPIE-The International Society for Optical Engineering* **2002**, *4690*, 381-390.

(10) Schmid, G. M.; Singh, V. K.; Flanagin, L. W.; Stewart, M. D.; Burns, S. D.; Willson, C. G. *Proceedings of SPIE-The International Society for Optical Engineering* **2000**, *3999*, 675-685.

(11) Schmid, G. M.; Stewart, M. D.; Burns, S. D.; Willson, C. G. *Journal of the Electrochemical Society* **2004**, 151, G155-G161.

Appendix A: Silylation Chamber Construction

BACKGROUND

A major goal of my dissertation was to develop new polymer / silylation agent systems for top surface imaging applications and to better understand their performance. The gas phase reaction step in which silicon is incorporated into the chemically reactive regions of the polymer is a complicated process. There exist many issues that are of utmost importance on the overall resist performance. There exist four fundamental properties of any resist / silylation agent system that need to be examined prior to imaging. The first is an examination of the reaction rate of the gaseous agent with the polymeric film. If the polymer doesn't react sufficiently quickly, it would be impractical for use. The second property is how the silicon is distributed within the film. If the polymer doesn't react fully within a reasonable time, the silicon content may be below the threshold 12 wt% required for adequate etch resistance, and render the resist useless. The third property is how the silylation step affects the glass transition temperature of the polymer, both after the reaction is complete, and while the reaction is taking place. Finally, one must be able to examine the chemical nature of the final film, to ensure that the final product is what one hoped for.

The last of the four desired pieces of information, the chemical nature of the film can be investigated by infrared spectroscopy of the final film. The first three pieces of information are substantially more challenging to accurately measure. One can monitor some of these properties by removing samples from a reaction chamber, and monitoring thickness and integrated infrared peaks, but this is a tedious and error filled process. For this reason, and others, it was very desirable to construct an apparatus that enabled in-situ monitoring of the reaction process, and subsequent interrogation of the film in a controlled environment.

GENERAL DESIGN CONSIDERATIONS

The final chamber needed to meet the following design criteria:

1. Overall temperature control, avoiding “cold spots” where condensation of the agent could occur.
2. Atmospheric to vacuum (down to 100mTorr) pressure control with very limited leaking (< 1Torr / hour)
3. Controlled silylation agent pressure control in order to allow for varied reaction conditions
4. Extremely precise and accurate control of the sample temperature. Additionally, controlled temperature ramping up to 200C for Tg measurements is desirable.
5. Small external chamber dimensions for incorporation with Woollam M2000 Spectroscopic Ellipsometer.

6. Heated, transparent, vacuum windows situated for 70^o (measured from normal) sampling using ellipsometer .

Design criteria 5 places the greatest limitations on overall design. The volume between the light source and the detector on the M 2000 is extremely limited. It was therefore decided that the only practical method for constructing this equipment was to make two main sections to apparatus. The first, would sit within the M 2000 was the sample section and have temperature control, easy sample loading and unloading, and a piped connection with the second section. The second section would be responsible for gas handling, and would be made up of pneumatically controlled valves within a moderately sized oven. The piping connecting the two sections would also be independently heated. The first section would contain heating elements, as well as thermal insulation for temperature uniformity and to prevent heating of the M2000 equipment. A schematic of the sample chamber and ellipsometer is shown in Figure A.1.

Figure A.1: Schematic of ellipsometry sample chamber

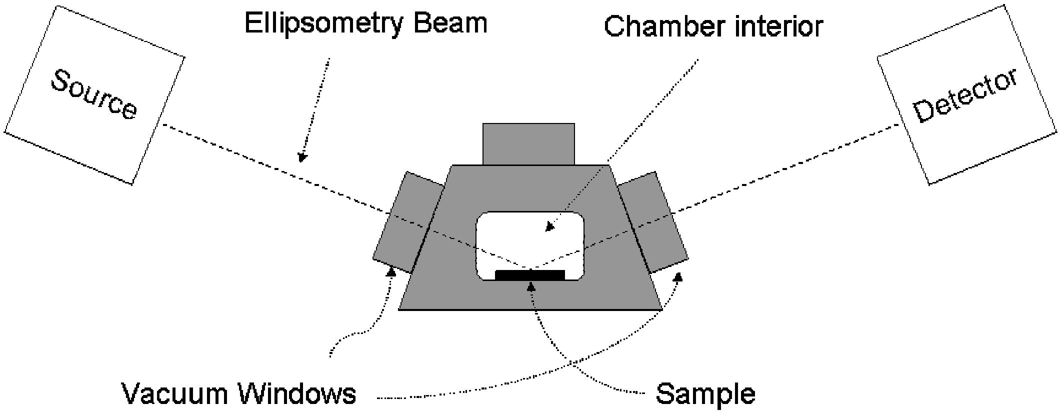

In order to meet design criteria 2, the low leak rate vacuum requirement, it was decided that windows and connections should be built based on Ultra High Vacuum technology (UHV). This meant using VCR and ConFlat connections throughout the system. Although this may seem to be over-engineered for such "high" pressures, the systems must be capable of sub-100mTorrr operation for significant amounts of time without active vacuum pumping, which is challenging with o-ring connections. Additionally, VCR and ConFlat systems employ various metal seals that limit the sorption of gaseous agents as compared to o-rings. The only exception to this design plan was the sample loading door, which needed to be constructed with a removable o-ring seal for ease in sample loading. VCR and ConFlat connections require stainless steel connections to be welded onto the chamber, forcing the chamber to be constructed of stainless steel. Stainless steel's chemical inertness is well suited to this application, but its poor heat transfer properties presented some challenges. This will be discussed further in the Thermal Management section. Additionally, the use of stainless steel presented machining challenges due to its hardness, but these were worked around by close collaboration with the machine shop.

SPECIFICS

Chamber

The top window port of the chamber allows for in-situ exposure of the wafer or in-situ infrared spectroscopy. The 1 1/3" ConFlat connections on the back wall exist for electrical and thermocouple feed-throughs. The ¼" VCR connections on the back wall exist for gas handling- one is for vacuum and nitrogen supply, while the other is used for silylation agent control.

2 ¾" ConFlat Fused Silica vacuum windows were purchased from Kurt Lesker Company for in-situ exposure and for ellipsometric probing. They have >80% transparency down to a wavelength of ~190nm, thereby covering the range of the ellipsometer. Their maximum heating rate is 2^{o}C / min, which will be discussed later.

The front wall of the chamber was polished, and the o-ring was place in a groove on the door. This was done in order to allow for flexibility in replacement of the o-ring, and repair work on the o-ring groove. The front door is held on by the pressure difference when the chamber is at vacuum.

The internal volume of the chamber was designed for ease of use with 2" and smaller wafers. On the bottom of the chamber sits the sample stage, consisting of a sandwich of 1/8" Aluminum, ¼" Teflon, a Kapton resistive heater, and 1/8" Aluminum (from the bottom to the top respectively). The sandwich is held together by Teflon bolts, and connected to the chamber bottom with Teflon bolts as well. The Teflon connectors and plate exist for uniform insulation. This assembly is motivated by the desire to overcome the temperature non-uniformity associated with the Stainless Steel, and to enable temperature ramping.

Valve Structure

The gas handling system is made up of a series of pneumatically controlled valves within a moderately sized oven. The oven system is connected to the sample chamber by two stainless steel pipes heated with resistive heaters and insulated with glass wool. A schematic of the valve structure is shown in Figure A.2.

Figure A.2: Schematic of Valve Stucture

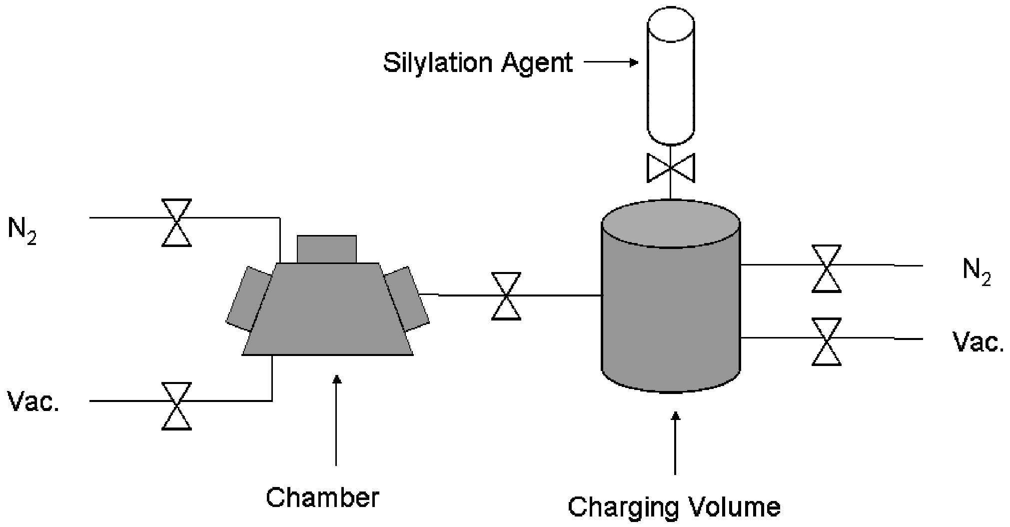

The primary operation scheme for the system is to use the vapor pressure of the agent in the sample chamber to place a known pressure of agent in the charging chamber. Upon equilibration, the valve between the charging chamber and the sample chamber is opened, instantly equilibrating the pressure between the two chambers. The thermal expansion issues associated with this process are discussed in the Thermal Management section. All valves are normally-closed, pneumatically actuated, bellows valves with maximum operating temperatures of 400°F.

The agent storage containers consist of a glass container vacuum-connected to a 2 ¾" CF. A 2 ¾" CF to ¼" VCR adaptor connects the glass container to a hand-turned ¼ VCR valve. An agent storage container is therefore easily disconnected and replaced with an alternate agent, all without exposure to the air.

The pressure is monitored by a 1000 torr capacitance manometer purchased from Edwards Vacuum Corporation. Capacitance manometers are known for their accuracy across a significant temperature range and their robustness in hazardous chemical environments. The manometer is attached to the charging chamber, so the pressure before and after equilibration can be monitored. Typical operation of the system is described later.

THERMAL CALCULATIONS

General Heating Background

The overall heating scheme for this system consists of 6 separate heating regions. Each region is controlled by a LabView based PID control algorithm (with the exception of the oven, which is controlled by the oven's thermostat). The six regions and their respective heaters are listed in table A.1.

Table A.1: Heating Configurations

Heating Region	Heater Type	Power	Power Type
Sample Chamber	(4) Omega ¼" diam. Cartridge- 2" long	80 W each	120 VAC
Sample Stage	(1) Omega Kapton Heater 2" square	40 W	28 VDC
Side Windows	(2) Omega 1"x 9" Silicone Heater	45 W each	120 VAC
Top Window	(1) Omega 1"x 9" Silicone Heater	45 W	120 VAC
Piping	(1) Glass lined Heating tape	~200W	120 VAC
Gas handling oven	(1) Fisher Scientific IsoTemp 500	~800 W	120 VAC

All temperatures are monitored with K type thermocouples purchased from Omega. The thermocouples are read with a National Instruments SCXI 1102 input board coupled with a 1303 Terminal Block. The National Instruments board is plugged into a SCXI 1000 Chassis connected to a National Instrument 6024 E DAQ board.

Chamber temperature uniformity

The construction of the sample chamber of stainless steel was necessitated by the use of UHV components throughout the system. This construction presented challenges associated with the uniform heating of the system. Uniform heating is important since cold spots could result in condensation if one works with high relative pressures of agents. Initially, a finite element analysis was performed using Pro-E on the stainless steel block itself. The critical boundary conditions included setting the temperature of the cartridge heaters to 100^{o}C, the convective heat transfer coefficient of the sidewalls at 30 W/m2, and the convective heat transfer coefficient of the bottom plate at 100W/m2. Assuming these values, the calculated temperature distribution is shown in Figure A.3. As can be seen, the chamber temperature uniformity is ~6^{o} C, with the coldest spot being the location of the sample. The cold spot's location is logical due to the symmetric placement of the cartridge heaters coupled with the substantial heat loss from the bottom of the plate. It should be noted that the application of a convective heat loss out of the bottom is not necessarily representative of the equipment's geometry. A conductive loss mechanism would have probably been more accurate, but this added complexity to the simulation.

Figure A.3: Temperature distribution simulation of the Stainless Steel sample chamber.

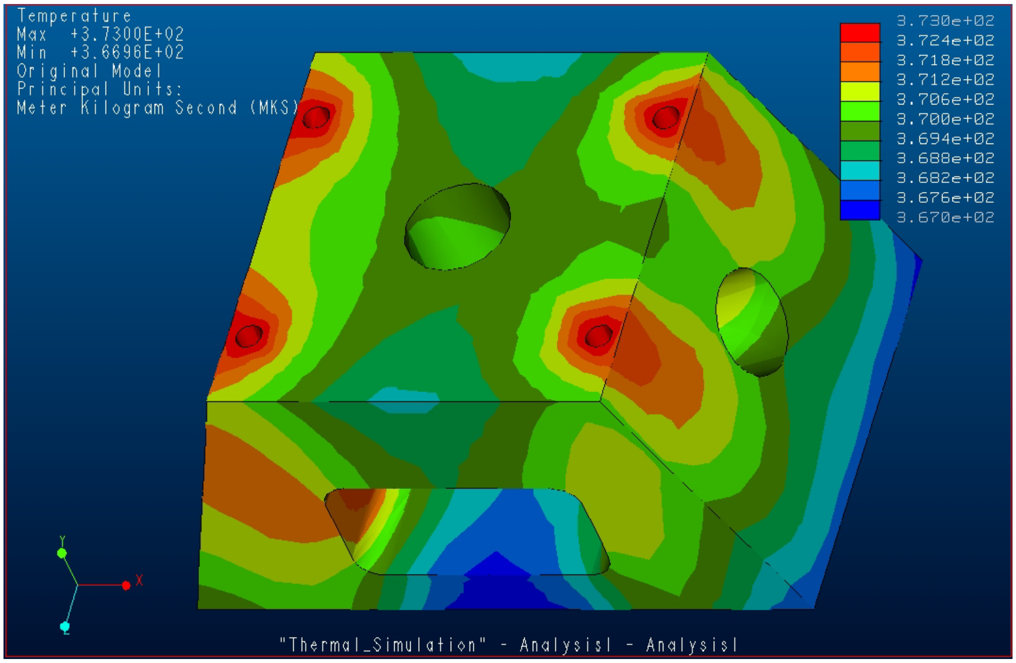

The FE simulation altered the design of the chamber in one critical way. Although the temperature distribution was acceptable in general, it was not uniform enough at the wafer plane for accurate kinetics measurement. The system would require a separately heated sample stage that was thermally isolated from the chamber, and constructed from a more conductive material such as aluminum. Additionally, after initial testing, it became clear that the windows would require separate heating due to their innate low conductivity and the large conduction pathway from the cartridge heaters.

Sample Stage Temperature Uniformity

During sample heating and ramping, the duration it takes for the sample stage to reach a uniform temperature is an important issue. This dictates the maximum ramping speed of the plate during Tg measuring processes, etc. Since the Aluminum plate sits in a non-conductive vacuum on 5 sides, and an insulating Teflon plate on the bottom, the system can be modeled as one-directional conduction from the areas that are heated by the Kapton heaters to the un-heated regions. A quick back-of-the-envelope calculation can be performed to investigate this issue. The 1/e thermal diffusion time can be approximated by $t = L^2 / 4 \alpha$ where t is the diffusion time, L is the path-length and α is the thermal diffusivity, which equals $k / \rho C_p$, where k is the thermal conductivity, ρ is the density, and Cp is the heat capacity. Assuming that L is 1cm, and α is 73e-6 m^2 / s, we find that the thermal diffusion time is 0.34 s. In this case, a heating rate of 5^o C / min is very reasonable, and overall temperature uniformity on the plate is very good.

Agent Thermal Expansion Issues

An issue that has received significant attention in many gas phase reaction chambers is the cooling associated with an adiabatic expansion of the silylation agent. As one would expect in any expanding gas, the temperature drops greatly during the expansion process. One can easily approximate the cooling by looking at the internal energy of a system.

$$dU = dQ - dW$$

Since the system is approximately adiabatic, $dQ = 0$, therefore

$$dU = - dW$$

Furthermore we see that,

$$Cv\ dT = -P\ dV$$

Plugging in the ideal gas law, $P = nRT / V$ and rearranging, we find

$-R\ dV / V = Cv\ dT / T$

Integrating from one state to another, and rearranging we find that

$$T_2 = T_1 (V_1 / V_2)^{2/5}$$

Plugging in a volume change of a factor of two, coupled with an initial temperature of 400K, we find that the final expanded gas temperature is 303K!!!. This represents a drastic temperature change, and previous researchers were appropriate in their fear of this issue. As such, some chambers were designed with large initial volumes in order to increase the relative volume. However, one must further analyze the duration it takes to heat the gas back up.

A good approximation method for looking at the transient heating of the gas is to look at the thermal diffusion time, as used in the previous section. So, $t = L^2 / 4 \alpha$. Plugging in the definition of α, we find:

$$t = L^2 \rho C_p / 4 k$$

In order to approximate k, we can look to Bird, Stewart and Lightfoot for k's for low pressure gases (First Edition p. 255)

$$k = \rho C_v u \lambda / 3$$

where u is the mean molecular speed, and λ is the mean free path of the molecule. Plugging in this relationship for k, along with the fact that $C_p / C_v = 7 / 5$ for ideal gases, we find:

$$t = L^2 / (u \lambda) * (21 / 20)$$

We can approximate u from BSL as well to be

$$u = (8RT / \pi M)^{1/2}$$

Where R is the ideal gas constant and M is the molecular mass. For a moderately sized molecule, with M = 100 g / mole, we find that u = 253 m / s. We can approximate λ according to McQuarrie as being

$$\lambda = R\, T / (2^{1/2} N_A \sigma P)$$

Where N_A is Avagadro's number, and σ is the collision cross section. If we assume our molecule has approximately the same collision cross-section of ethylene of 0.58 nm^2, and that the pressure is 100 torr, we find that λ = 3.7 e-7 m. Plugging this into the time relationship above, with L = 1cm, (the farthest point any gas is from a wall), we find that t = ~1 s. In other words, despite the fact that the gas cooled 100^{o}C, it subsequently rises substantially in the first second at the coldest spot in chamber. Overall, the effect appears to be negligible due to the fact that the heat capacity of the gas is incredibly small. Within a few seconds, the gas has heated back up again. This is confirmed by monitoring the pressure after expansion, where the pressure rarely rises. More importantly, the gas close to the sample reaches equilibrium with the sample much quicker. In fact, once the gas flow has stopped, the gas directly above the sample will heat instantly in comparison with the time frame of the experiment.

AUTOMATION

In order to control 5 temperature zones while simultaneously controlling 6 pneumatic valves, it quickly became apparent that automated operation with a computer was necessary. Fortunately, the Willson group has a significant amount of experience in this area, especially using LabView. Four areas needed to be developed in order for the automation to occur. First, a DAQ interface for communication and control between the computer and the real world needed to be researched and purchased. Second, hardware needed to be constructed that takes the low-voltage outputs of the DAQ card and translates it into useful signals (such as 120 VAC signals, etc). Third, programs in LabView needed to be written. Finally, separate, hardware based safety devices needed to be developed in case the software or hardware failed (this is especially important due to the high power present in the heating systems).

Inputs such as temperature and pressure are monitored using a National Instruments SCXI 1102 input board coupled with a 1303 Terminal Block. Outputs are generated with a National Instruments SCXI 1163 optically isolated digital output board coupled with a 1326 terminal block. The National Instruments boards are plugged into a SCXI 1000 Chassis connected to a National Instrument 6024 E DAQ board. The SCXI-1163 digital output board is essentially a bank of 32 independent switches for an external 5V signal to pass through. If the output board signals open, the externally connected 5V signal will be able to pass through the switch at very low currents. This 5V signal can be used to drive TTL based devices, such as relays for larger signals.

CONTROL BOX

Inside a rack mountable chassis, the relay and power supply connections were assembled. The 5V output signals of the SCXI 1163 board are connected to a 16 position relay mounting board. The mounting board contains a mixture of AC and DC relays used to control the representative output equipment. In the case of AC heaters, 120 VAC signals are connected in parallel through the relays to their respective heaters. For the sample stage heater, a 24 VDC power supply is attached to the heater's DC relay. The pneumatic valves are opened by use of a 24 VDC signal attached to the DC relays opening solenoid air valves. A 12 VDC power supply is present for driving the cooling fan, as well as future possible work using a peltier based cooling system (4 relays are connected to the 12 VDC power supply for this application, although they are not currently active). An additional 120 VAC connection is present in the chassis for external plate heaters. The mounting board connections SCXI 1163 output connections are listed in Table A.2. Table A.3 shows the thermocouple input positions on the SCXI 1102.

Table A.2: SCXI output connections

Output	**Line #**	**Output**	**Line #**
Heater Block	10	Valve Mixing	1
Peltier A1	6	Valve N2 to Chamber	0
Peltier A2	7	Valve SA (back) to Chamber	5
Peltier B1	8	Valve SA(front) to Chamber	2
Peltier B2	9	Valve Vac to Chamber	4

Heater Piping	11	Valve Vac to Charger	3
Heater Window Side	12		
Heater Window Top	13		
Heater Kapton	14		

Table A.3: SCXI input Connections

Input	**Line #**
Temp Block	15
Temp Stage bottom	20
Temp Stage top	19
Temp Piping	16
Temp window side	17
Temp window top	14

LABVIEW PROGRAM

A simple Labview program was generated that controls the five heating zones and the six pneumatic valves. The temperature control algorithm works with a time modulated output from a canned LabView PID algorithm. The PID parameters were experimentally determined, and are shown in table A.4. A screen-shot of the program interface is shown in Figure A.4.

Table A.4: PID parameters for the various heating regions.

Heating Zone	P	I	D
Block	0.02	0	0
Piping	0.01	0	0
Windows Top	0.02	0.1	0.05
Windows Side	0.02	0.1	0.05
Kapton Stage	0.02	0.1	0.1

Figure A.4: Screen shot of the control software user interface.

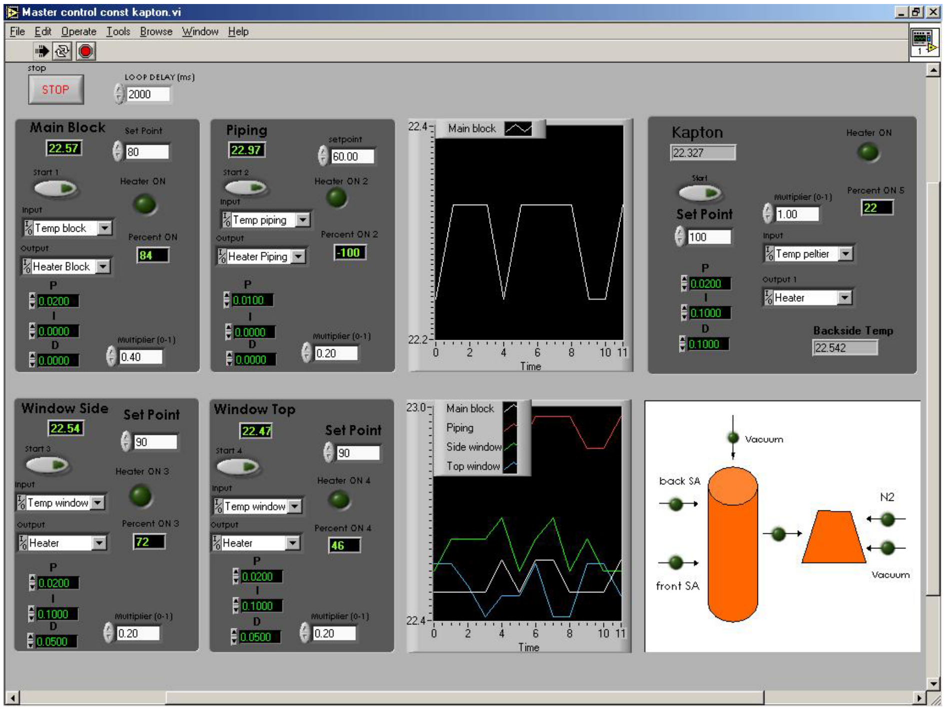

LOOP DELAY (ms) 2000

Main Block 22.57
Set Point 80
Start 1
Heater ON
Input Temp block
Output Heater Block
Percent ON 84
P 0.0200
I 0.0000
D 0.0000
Multiplier (0-1) 0.40

Piping 22.97
setpoint 60.00
Start 2
Heater ON 2
Input Temp piping
Output Heater Piping
Percent ON 2 -100
P 0.0100
I 0.0000
D 0.0000
Multiplier (0-1) 0.20

Kapton 22.327
Heater ON
Start
Set Point 100
Multiplier (0-1) 1.00
Percent ON 5 22
Input Temp peltier
Output 1 Heater
P 0.0200
I 0.1000
D 0.1000
Backside Temp 22.542

Window Side 22.54
Set Point 90
Start 3
Heater ON 3
Input Temp window
Output Heater
Percent ON 3 72
P 0.0200
I 0.1000
D 0.0500
Multiplier (0-1) 0.20

Window Top 22.47
Set Point 90
Start 4
Heater ON 4
Input Temp window
Output Heater
Percent ON 4 46
P 0.0200
I 0.1000
D 0.0500
Multiplier (0-1) 0.20

SAFETY

There are a number of significant safety issues associated with the equipment. The first issue is the toxic nature of many of the gaseous agents that are used in these experiments. For this reason all equipment was installed in fume hood. Additionally, the vent of the vacuum pump feeds back to the fume hood.

The second issue is the potential over-heating of various aspects of the equipment. It is simple to envision a software bug, or hardware problem leading to the opening of a relay that controls a heater. Many of the heaters have significant power relative to their heat loss mechanisms, and if run without active control could heat to dangerous conditions. In order to protect against this problem an Omega CN101K-500C temperature monitor was purchased that simultaneously measures the temperature of 6 thermocouples that are attached to the various heating regions. Each thermocouple has an individual maximum set-point. If any of the temperatures exceed that set-point, a relay opens that shuts off power to the entire Control box (ie all heating elements will be shut down). The safety is hardware based, and independent of the computer and National Instruments equipment. Thus, software errors or errors associated with the National Instruments equipment are protected against.

The third safety issue is associated with the electrical feed-through for the kapton heater within the vacuum chamber. The feed-through contains large gauge copper wires with a 24V power supply. The maximum current of the power supply is fairly low, but all attempts should still be made to avoid a shock. The block itself is grounded to earth in order to ensure that if the feed-through has a short, the block itself will not shock the user.

The fourth safety issue that is of significant value is keeping track exactly what two agents are present in the oven prior to heating. Since two agents can be attached in the oven at any given time, it is easy to forget to check the properties of the other agent. If one were to heat the chamber to an adequate temperature for one silyation agent, it is very possible that one could exceed the atmospheric boiling point of the second agent. This could possibly cause rupture or explosion of the glass container storing the agent. Many of these agents are flammable, and their release in the presence of heating elements could result in a fire. There is one method currently employed to avoid this potential problem, and that is a label on the front panel of the oven that is constantly updated every time an agent is changed out. Future plans include changing the agent storage containers to steel instead of glass; thereby increasing the pressure the containers are capable of withstanding.

There are a number of addition safety precautions that have been undertaken while constructing this equipment. However, this is not the appropriate document for such a discussion. These four issues are of paramount importance, justifying their inclusion here.

TYPICAL OPERATION

Agent Loading

The two-valve design for each silylation agent allows easy disconnection and replacement of various silylation agents. All that is required is the closing of the hand-turn valve on the agent container, followed by pumping down of the line between the two valves. The new container is attached with a new VCR gasket. The section between the two valves is pumped out, and the hand turn is opened. Often it is wise to pump a couple of volumes of the charging chamber out in order to remove any air that leaked into the agent container (this is particularly true upon first use of the agent, often requiring 4-6 pump downs in order to ensure purity). Silylation agent container replacement should occur only when the oven is cold.

Sample loading and measurement

Prior to sample loading, the sample heating stage must be turned off. The chamber is vented using the pneumatic valve controlling air delivery to the sample chamber. The old sample is extracted, and a new one is placed in the chamber. At this point, the sample must be properly aligned with the ellipsometry beam. A single ellipsometer spectroscopic scan is performed to ensure proper operation and alignment. The sample chamber is then pumped down to vacuum.

If not already at vacuum, the charging chamber is pumped to vacuum as well. The sealing of the sample chamber door is checked by opening the valve between the two chambers, and the vacuum valves are closed. At this point the sample stage heater is turned on and allowed to come to equilibrium. The system is allowed to sit for at least 15 minutes to reach thermal equilibrium throughout the system (including the door), and to ensure no leaks. The valve between the chambers is closed.

When you are ready to start your run, begin collecting data on the ellipsometer. Wait at least one minute to establish a thickness baseline. The silylation agent is then used to charge up the charging chamber. Upon reaching the appropriate adjusted pressure (approx 5/3 times the desired final pressure), the valve between the chambers is opened, and the reaction begins.

HOTBLOCK V.II CONSTRUCTION

BACKGROUND

Gas phase silylation reactions performed at International SEMATECH were undertaken on a Genesis MicroStar 250C. The Genesis tool was designed for top surface imaging processes, most of which used moderately volatile silylation agents such as dimethylaminodimethylsilane. The tool was built for a semiconductor fab environment and wafer throughput was of paramount importance. The tool's vapor dosing sub-system, called a "hotblock" works extremely well for the types of processes the tool was designed for. However, the hotblock's dosing process was not well suited for research work. First, silylation agent loading is not easy- the process was extremely time consuming and prone to contamination. Second, the large volume and poor temperature control was not good for working with small volumes of agents. Third, the dosing process and pressure transducers were not capable of accurate work with low-vapor pressure agents (<10torr). Finally, the construction of the hotblock relied heavily on o-ring seals. These seals were often permeable to various agents, resulting in agent loss, as well as sorbtion and desorbtion of agents, causing cross-contamination. Additionally, the o-rings often degraded and outright failed, allowing air to enter the hotblock. For these reason it became necessary that a new hotblock be designed and built.

Construction and Schematic

The design for this hotblock was based on the vapor delivery system described in the ellipsometry chamber section above. A schematic of the hotblock is shown in figure A.5. A simple metal agent container with a two valve connection point is attached to a charging chamber with a capacitance manometer. The charging chamber is attached to the sample chamber with a single sample dumping pneumatic valve. The entire assembly is placed within a home built oven assembly. Since the equipment was to be integrated with the existing Genesis tool, temperature and pneumatic valves were designed using the same equipment as the old hotblock. Additionally, the small oven had to fit into the limited volume of the Genesis tool.

Figure A.5: Schematic of the hotblock v.II.

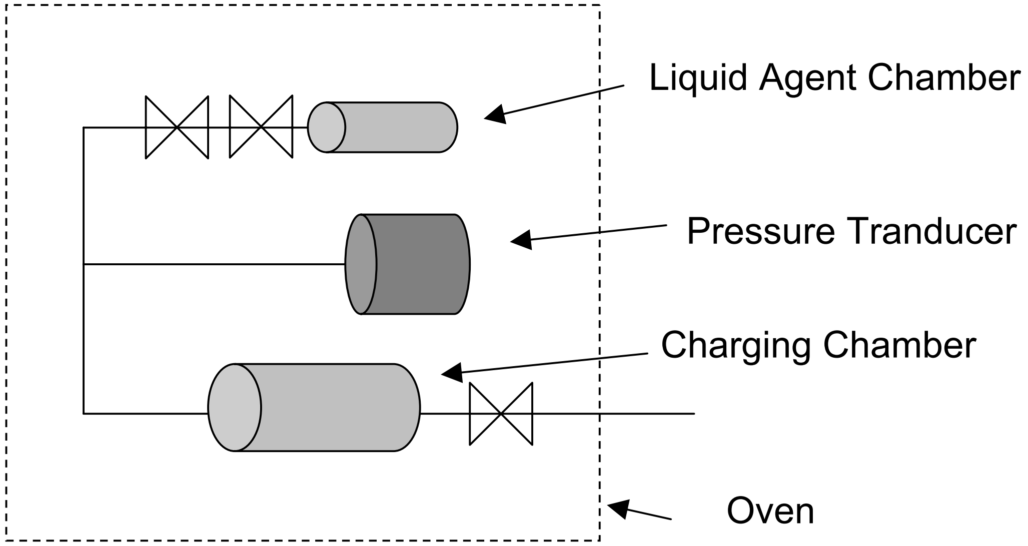

The agent container was made from a stainless steel 1 1/3” ConFlat full nipple blanked on one side and with a ¼” VCR adapter on the other. The ¼” VCR connects to a hand-turn valve connected to a normally closed pneumatic bellows valve. On the other side of the bellows valve is the charging chamber, made from a 2 ¾” ConFlat full nipple with ¼” VCR adapters on each side. A capacitance manometer measures pressure in the charging chamber. On the other side of the charging chamber is another pneumatically controlled valve that connects the charging chamber to the sample chamber. The pneumatic valves are controlled using the Genesis tool’s interface.

The oven housing was designed to fit snugly within the available space in the Genesis tool. The wall are a stacked composite of 1/16" Aluminum for structural support, spacers for an airgap, ¼" Teflon, and internal spacers. Typical external temperature remains below 40^{o}C, assuming moderate flow of air around the exterior, which is typical in the Genesis tool due to venting of that region for safety purposes.

Heating is performed with two 300 W 6" cartridge heaters controlled by the Genesis tool. Temperature is measured with a J-Type Thermocouple. The heaters are inserted into a ½" aluminum plate on the bottom of the oven. Three Aluminum cradles are bolted down to the Aluminum heating plate, on which rest the capacitance manometer and the two full nipples. The cradles assist in heat conduction into the gas handling system. Additionally, two fans mounted on the top lid of the oven blow are vertically down on the plate, assisting in heating through substantial increased heating. Typical heating times are on the order of 2 hours. Figure A.6 shows the temperature heating profiles at 5 locations as a function of time, and illustrates that the hotblock uniformity is less than 6^{o} C.

Figure A.6: Temperature heating profiles in the hotblock as a function of time for five locations.

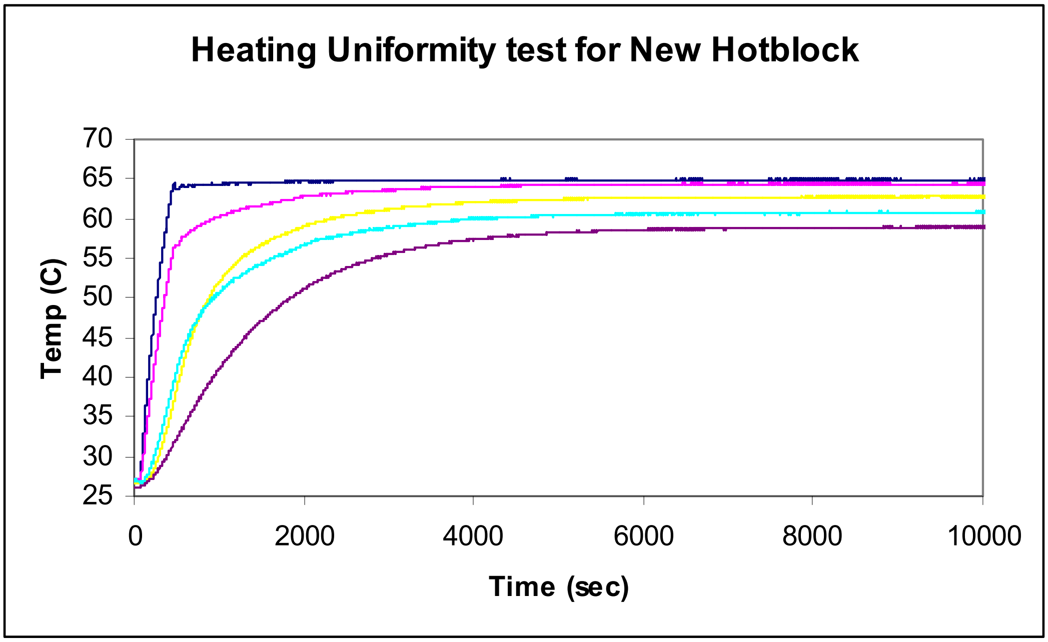

Bibliography

Belot, V.; Corriu, R.; Leclercq, D.; Mutin, P. H.; Vioux, A. *Chem. Mater.* **1991**, *3*, 127-131.

Boettcher, M.; Bauch, L.; Stolberg, I. *J. Vac. Sci. Technol., B* **1994**, *12*, 3473-3477.

Brodsky C., *et al*, *J. Vac. Sci. Technol*. B, **18 (6),** 3396-3401 Nov/Dec (2000)

Burns, S. D.; Medeiros, D. R.; Johnson, H. F.; Wallraff, G. M.; Hinsberg, W. D.; Willson, C. G. *Proceedings of SPIE-The International Society for Optical Engineering* **2002**, *4690*, 321-331.

Burns, S. D.; Schmid, G. M.; Trinque, B. C.; Willson, J.; Wunderlich, J.; Tsiartas, P. C.; Taylor, J. C.; Burns, R. L.; Willson, C. G. *Proceedings of SPIE-The International Society for Optical Engineering* **2003**, *5039*, 1063-1075.

Chan, V. Z. H.; Thomas, E. L.; Frommer, J.; Sampson, D.; Campbell, R.; Miller, D.; Hawker, C.; Lee, V.; Miller, R. D. *Chemistry of Materials* **1998**, *10*, 3895-3901.

Chang, T. H. P.; Kern, D. P.; Muray, L. P. *J. Vac. Sci. Technol., B* **1992**, *10*, 2743-2748.

Chiang, W. Y.; Lu, J. Y. *Journal of Polymer Science, Part A: Polymer Chemistry* **1991**, *29*, 399-410.

Cobb J., Conley W., Huang F., Lii T., Usmani S., Hector S., Wu W., *Proc. SPIE* **4345**, (2001).

Cobb, J. L.; Rauf, S.; Thean, A.; Dakshina-Murthy, S.; Stephens, T.; Parker, C.; Peters, R. D.; Rao, V. *Proceedings of SPIE-The International Society for Optical Engineering* **2003**, *5039*, 376-383.

Condo, P. D.; Paul, D. R.; Johnston, K. P. *Macromolecules* **1994**, *27*, 365-371.

Dammel, R. R. *Spie Press* **1993**, *TT 11*.

Dao, T. T.; Spence, C. A.; Hess, D. W. *Proceedings of SPIE-The International Society for Optical Engineering* **1991**, *1466*, 257-268.

Domke W. D., Graffenberg V. L., Patel S., Rich G. K., Cao H. B., Nealey P. F., *Proc. SPIE* **3999**, 313 (2000)

Ellington, J. C., Jr.; Arnett, E. M. *Journal of the American Chemical Society* **1988**, *110*, 7778-7785.

Fel, L. G.; Zimmels, Y. *Los Alamos National Laboratory, Preprint Archive, Condensed Matter* **2002**, 1-25, arXiv:cond-mat/0211045.

Goethals, A. M.; Lombaerts, R.; Roland, B.; Van den Hove, L. *Microelectronic Engineering* **1991**, *13*, 37-40.

Gratzke, U.; Kapadia, P. D.; Dowden, J.; Kroos, J.; Simon, G. *Journal of Physics D: Applied Physics* **1992**, *25*, 1640-1647.

Grinfeld, M. *Mechanics Research Communications* **1994**, *21*, 613-616.

Harkness, B. R.; Takeuchi, K.; Tachikawa, M. *Macromolecules* **1998**, *31*, 4798-4805.

Hinsberg, W.; Hoffnagle, J.; Houle, F. *Microlithography World* **2000**, *9*, 16, 18, 20-22.

Houle, F. A.; Hinsberg, W. D. *Book of Abstracts, 219th ACS National Meeting, San Francisco, CA, March 26-30, 2000* **2000**, CHED-998.

Houle, F. A.; Hinsberg, W. D.; Morrison, M.; Sanchez, M. I.; Wallraff, G.; Larson, C.; Hoffnagle, J. *Journal of Vacuum Science & Technology, B: Microelectronics and Nanometer Structures* **2000**, *18*, 1874-1885.

Hung R. J., *et al*, *Proc. SPIE* **4345** (2001)

Ito, H.; Willson, C. G. *Polymers in Electronics* **1984**, *ACS Symposium Series 242*, 11-23.

Ito, H.; MacDonald, S. A.; Miller, D. A.; Willson, C. G. *US Patent* **1985**, *4,552,83*.

Ito H., Seehof N., Sato R., Nakayama T., Ueda M., *Micro- and Nanopatterning Polymers*, ACS Symposium Series **706**, 210-212

Ito, H. S., N.; Sato, R.;Nakayama, T.;Ueda, M *Micro- and Nanopatterning Polymers*; ACS, 1998.

Jamieson, A. T.; Somervell, M. H.; Tran, H. V.; Hung, R. J.-P.; MacDonald, S. A.; Willson, C. G. *Proceedings of SPIE-The International Society for Optical Engineering* **2001**, *4345*, 406-416.

Kong, Y.-P.; Tay, F. E. H.; Xu, Y. *Proceedings of SPIE-The International Society for Optical Engineering* **2000**, *4230*, 89-99.

Kratschmer, E.; Kim, H. S.; Thomson, M. G. R.; Lee, K. Y.; Rishton, S. A.; Yu, M. L.; Chang, T. H. P. *Journal of Vacuum Science & Technology B* **1994**, *12*, 3503-3507.

Kratschmer, E.; Kim, E. S.; Thomson, M. G. R.; Lee, K. Y.; Rishton, S. A.; Yu, M. L.; Chang, T. H. P. *J. Vac. Sci. Technol., B* **1995**, *13*, 2498-2503.

Kudryashov, V. A.; Krasnov, V. V.; Prewett, P. D.; Hall, T. J. *Microelectron. Eng.* **1997**, *35*, 165-168.

Kunz R.R., Bloomstein T. M., Hardy D. E., Goodman R. B., Downs D. K., Curin J.E., *Proc. SPIE* **3678**, 13 (1999)

Lee, K. Y.; Hsu, Y.; Le, P.; Tan, Z. C. H.; Chang, T. H. P.; Elian, K. *Journal of Vacuum Science & Technology, B: Microelectronics and Nanometer Structures* **2000**, *18*, 3408-3413.

Lee, Y. H.; Browning, R.; Maluf, N.; Owen, G.; Pease, R. F. W. *J. Vac. Sci. Technol., B* **1992**, *10*, 3094-3098.

Lee, Y.; Lee, W.; Chun, K.; Kim, H. *Journal of Vacuum Science & Technology B* **1999**, *17*, 2903-2906.

Liu, W.; Ingino, J.; Pease, R. F. *J. Vac. Sci. Technol., B* **1995**, *13*, 1979-1983.

Lo, C. W.; Rooks, M. J.; Lo, W. K.; Isaacson, M.; Craighead, H. G. *J. Vac. Sci. Technol., B* **1995**, *13*, 812-820.

MacDonald S. A., Schlosser H., Ito H., Clecak N. J., Willson C. G., *Chem. Mater*. **3**, 435-442 (1991)

MacDonald, S. A.; Schlosser, H.; Ito, H.; Clecak, N. J.; Willson, C. G. *Journal of Photopolymer Science and Technology* **1991**, *4*, 487-495.

MacDonald S. A., Schlosser H., Clecak N. J., Willson C. G., Fréchet J. M. J., *Chem. Mater*. **4**, 1364 (1992).

Mack, C. A. *Opt. Eng. (Bellingham, Wash.)* **1993**, *32*, 3350-3362.

Mack, C. A. *Inside ProLith*, 1997.

Mahorowala A. P., *et al. SPIE* **4343** (2001)

Maile, B. E.; Henschel, W.; Kurz, H.; Rienks, B.; Polman, R.; Kaars, P. *Japanese Journal of Applied Physics, Part 1: Regular Papers, Short Notes & Review Papers* **2000**, *39*, 6836-6842.

Matsuzawa, N. N.; Mori, S.; Endo, M.; Morisawa, T.; Kaimoto, Y.; Kuhara, K.; Sasato, M. *Journal of Photopolymer Science and Technology* **1998**, *11*, 625-632.

McCord, M. A.; Newman, T. H. *Journal of Vacuum Science & Technology B* **1992**, *10*, 3083-3087.

Moore, G. E. *Electronics* **1965**, *36*.

Mori, S.; Matsuzawa, N.; Morisawa, T.; Kaimoto, Y.; Endo, M.; Matsuo, T.; Kuhara, K.; Sasago, M. *Journal of Photopolymer Science and Technology* **1997**, *10*, 603-608.

Namatsu, H.; Takahashi, Y.; Yamazaki, K.; Yamaguchi, T.; Nagase, M.; Kurihara, K. *J. Vac. Sci. Technol., B* **1998**, *16*, 69-76.

Namatsu, H.; Yamaguchi, T.; Nagase, M.; Yamazaki, K.; Kurihara, K. *Microelectron. Eng.* **1998**, *41/42*, 331-334.

Ngai, P. In *Physical Properties of Polymers Handbook*; American Institute of Physics, 1996, pp 139.

Nicolau, D. V.; Jinescu, G.; Fulga, F. *Proceedings of SPIE-The International Society for Optical Engineering* **1992**, *1672*, 461-471.

Pawloski, A. R.; Christian; Nealey, P. F. *Chemistry of Materials* **2002**, *14*, 4192-4201.

Pease, R. F. W. *The IEEE 9th Annual Symposium on Electron, Ion, and Laser Beam Technology, Edited by RFW Pease (San Francisco, CA)* **1967**, 176.

Peters, R. D.; Amblard, G. R.; Lee, J.-J.; Guenther, T. *Proceedings of SPIE-The International Society for Optical Engineering* **2003**, *5039*, 393-403.

Peterson, P. A.; Radzimski, Z. J.; Schwalm, S. A.; Russell, P. E. *J. Vac. Sci. Technol., B* **1992**, *10*, 3088-3093.

Pierrat, C.; Paniez, P.; Martin, P. *Proceedings of SPIE-The International Society for Optical Engineering* **1991**, *1466*, 248-256.

Polasko, K. J.; Yau, Y. W.; Pease, R. F. W. *Proc. SPIE-Int. Soc. Opt. Eng.* **1982**, *333*, 76-82.

Postnikov S. V., Somervell M. H., Henderson C. L., Willson C. G., Katz S., Byers J., Qin A., Lin Q., *Proc. SPIE* **3333**, 997 (1998).

Satyalakshmi, K. M.; Olkhovets, A.; Metzler, M. G.; Harnett, C. K.; Tanenbaum, D. M.; Craighead, H. G. *Journal of Vacuum Science & Technology, B: Microelectronics and Nanometer Structures* **2000**, *18*, 3122-3125.

Schock, K. D.; Prins, F. E.; Strahle, S.; Kern, D. P. *J. Vac. Sci. Technol., B* **1997**, *15*, 2323-2326.

Siew, Y. K.; Sarkar, G.; Hu, X.; Hui, J.; See, A.; Chua, C. T. *J. Electrochem. Soc.* **2000**, *147*, 335-339.

Simakov, N. N. *Mikroelektronika* **1995**, *24*, 108-112.

Sirard, S. M.; Green, P. F.; Johnston, K. P. *Journal of Physical Chemistry B* **2001**, *105*, 766-772.

Sirard, S. M.; Ziegler, K. J.; Sanchez, I. C.; Green, P. F.; Johnston, K. P. *Macromolecules* **2002**, *35*, 1928-1935.

Somervell, M. H.; Byers, J.; Willson, C. G. *Abstracts of Papers of the American Chemical Society* **1999**, *218*, 29-PMSE

Somervell, M. H.; Fryer, D. S.; Osborn, B.; Patterson, K.; Byers, J.; Willson, C. G. *Journal of Vacuum Science & Technology, B: Microelectronics and Nanometer Structures* **2000**, *18*, 2551-2559.

Somervell, M. Doctoral, University of Texas, Austin, 2000.

Sooriyakumanaran R., Fenzel-Alexander D., Fender N., Wallraff G.M., Allen R.D., *Proc. SPIE* **4345**, (2001).

Stark, T. J.; Edenfeld, K. M.; Griffis, D. P.; Radzimski, Z. J.; Russell, P. E. *J. Vac. Sci. Technol., B* **1993**, *11*, 2367-2372.

Stewart, M. D.; Schmid, G. M.; Goldfarb, D. L.; Angelopoulos, M.; Willson, C. G. *Proceedings of SPIE-The International Society for Optical Engineering* **2003**, *5039*, 415-422.

Tanaka, S.; Umbach, C. C.; Blakely, J. *Surface Science* **1997**, *372*, L298-L300.

Tanenbaum, D. M.; Lo, C. W.; Isaacson, M.; Craighead, H. G.; Rooks, M. J.; Lee, K. Y.; Huang, W. S.; Chang, T. H. P. *J. Vac. Sci. Technol., B* **1996**, *14*, 3829-3833.

Thompson, L. F., Willson, C. Grant, Bowden, M. J. *Introduction to Microlithography*; ACS, 1983.

Turner, S. R.; Arcus, R. A.; Houle, C. G.; Schleigh, W. R. *Polymer Engineering and Science* **1986**, *26*, 1096-1100.

van Delft, F. C. M. J. M.; Weterings, J. P.; van Langen-Suurling, A. K.; Romijn, H. *Journal of Vacuum Science & Technology, B: Microelectronics and Nanometer Structures* **2000**, *18*, 3419-3423.

Visser, R. J.; Schellekens, J. P. W.; Reuhman-Huisken, M. E.; Van Ijzendoorn, L. J. *Proceedings of SPIE-The International Society for Optical Engineering* **1987**, *811*, 62-68.

Whelan, C. S.; Tanenbaum, D. M.; La Tulipe, D. C.; Isaacson, M.; Craighead, H. G. *J. Vac. Sci. Technol., B* **1997**, *15*, 2555-2560.

Wong, H. C.; Campbell, S. W.; Bhethanabotla, V. R. *Fluid Phase Equilibria* **1997**, *139*, 371-389.

Woollam, J. A.; Johs, B.; Herzinger, C. M.; Hilfiker, J.; Synowicki, R.; Bungay, C. L. *Critical Reviews of Optical Science and Technology* **1999**, *CR72*, 3-28.

Woollam, J. A.; Green, S. E.; Hilfiker, J. N.; Tiwald, T. E.; Bungay, C. L.; Synowicki, R. A.; Meyer, D. E.; Herzinger, C. M.; Pfeiffer, G. L.; Cooney, G. T. *Proceedings of SPIE-The International Society for Optical Engineering* **2000**, *4099*, 197-205.

Woollam, J. A.; Hilfiker, J. N.; Bungay, C. L.; Synowicki, R. A.; Tiwald, T. E.; Thompson, D. W. *AIP Conference Proceedings* **2001**, *550*, 511-518.

Woollam, J. A.; Bungay, C.; Hilfiker, J.; Tiwald, T. *Nuclear Instruments & Methods in Physics Research, Section B: Beam Interactions with Materials and Atoms* **2003**, *208*, 35-39.

Yau, Y. W.; Pease, R. F. W.; Iranmanesh, A. A.; Polasko, K. J. *Journal of Vacuum Science & Technology* **1981**, *19*, 1048-1052.

Zimm, B. H.; Lundberg, J. L. *Journal of Physical Chemistry* **1956**, *60*, 425-428.

Vita

Andrew Thomas Jamieson is the son of James and Marie Jamieson, and was born in Boston, MA on July 22, 1977. He grew up in the Seattle area where he graduated from Woodinville High School in 1995. He attended the Massachusetts Institute of Technology, and received Bachelors of Science degrees in Chemistry and Chemical Engineering in 1999. He began studies at the University of Texas at Austin shortly thereafter, and received a Masters of Science degree in Chemical Engineering in the Fall of 2002. He has worked in research positions at Bristol-Meyer Squibb, the University of Washington, MIT, the University of Texas and ETEC Systems. He begins work at Intel in Santa Clara starting in the Spring of 2004.

Permanent address: PO Box 1670, Woodinville, WA, 98072